MICROFABRICATED HIGH-PERFORMANCE LIQUID CHROMATOGRAPHY (HPLC) SYSTEM WITH CLOSED-LOOP FLOW CONTROL

Thesis by

Jason Shih

In Partial Fulfillment of the Requirements

For the Degree of

Doctor of Philosophy

California Institute of Technology

Pasadena, CA

2008

(Defended 5/5/2008)

© 2008

Jason Shih

All Rights Reserved

Acknowledgements

I would first like to thank my graduate advisor, Dr. Yu-Chong Tai. From giving me the opportunity to join his lab as a bored undergrad to mentoring me throughout my graduate years, his guidance has been invaluable. I would also like to thank Dr. Terry Lee from the City of Hope, who in many ways was a co-advisor throughout my graduate studies. Without him, much of this work would have been impossible. Finally, I would like to acknowledge Dr. Markus Kalkum, another PI at City of Hope, who I've been lucky to work with in more recent years.

I have also had the opportunity to work with many talented students over the years. In particular, I would like to acknowledge Jun Xie for mentoring me my first few years in the Caltech Micromachining Lab and starting me down the microfluidics path. I would also like to thank fellow Caltech Micromachining Lab members Trevor Roper, Tanya Owen, Christine Garske, Agnes Tong, Ellis Meng, Justin Boland, Matthieu Liger, Qing He, Victor Shih, Scott Miserendino, Angela Tooker, Damien Rodger, Changlin Pang, PJ Chen, Quoc Quach, Wen Li, Nick Lo, Mike Liu, Luca Giacchino, Ray Huang, Jefferey Lin, Monty Nandra, Justin Kim, Bo Lu, Yok Satsanarukkit, Wendian Shi, and Ying-Ying Wang for their helpful suggestions and discussions during my time here.

My research has also taken me to City of Hope where I also got the chance to work with many wonderful people. In particular, Yunan Miao, who taught me pretty much everything I know about liquid chromatography and mass spectrometry, and spent years helping me troubleshoot these devices. Also I would like to thank Roger Moore, Karine Bagramyan, Diana Diaz-Arevalo, and Teresa Hong for help with my experiments.

Finally, I would like to thank my family for their support over the years. Even though I still don’t think they know exactly what I do as a graduate student (“I think he makes small things”), their encouragement has kept me going over the years.

Abstract

This thesis presents the development of a microfabricated high-performance liquid chromatography (HPLC) system. The design, fabrication, and characterization of individual HPLC components such as high-pressure pumps, mixers, flow sensors, composition sensors, separation columns, filters, and detectors is presented. These individual components were then integrated to create robust, feedback-driven separation systems capable of performing gradient, reverse-phase, nanoscale HPLC. Two separate separation systems were created. The first integrated system was a microfluidic device for HPLC tandem mass spectrometry (HPLC-MS/MS) designed for proteomic applications. The second system was a portable HPLC conductivity detection (HPLC-CD) system designed for point-of-care applications such as biodetection. Both systems demonstrated good performance and repeatability. The performance of these systems is largely attributable to the development of HPLC-compatible sensors that could provide precise control over the elution profiles. These microfluidic closed-loop flow control systems represent an important advancement in the microfluidics field, where open-loop flow control is universally used, and risks becoming inadequate with the increasing complexity of microfluidic systems.

Table of Contents

Chapter 1: Introduction to Microfluidics ... 1
1.1. Introduction ... 1
1.2. Microfluidic Phenomena ... 2
1.2.1. Laminar Flow ... 2
1.2.2. Multiphase Interfaces ... 4
1.2.3. Electrokinetics ... 6
1.3. Fabrication Technologies ... 8
1.3.1. Bulk Micromachining ... 9
1.3.2. Surface Micromachining ... 11
1.3.3. Soft Lithography ... 13
1.3.4. Other ... 15
1.4. Microfluidic Components ... 15
1.4.1. Fluid Handling ... 16
1.4.2. Fluid Sensing ... 17
1.4.3. Fluid Interfacing ... 18
1.4.4. Fluid Processing ... 19
1.5. HPLC / Conclusion ... 21
Chapter 2: Parylene Surface Micromachining Technology ... 27
2.1. Introduction ... 27
2.1.1. Parylene Background ... 27
2.1.2. Parylene Surface Micromachining with Photoresist as a Sacrificial Material 29
2.2. Experimental ... 31

2.2.1. Materials 31

2.2.2. Parylene Processing 33

2.2.2.1. Deposition 33

2.2.2.2. Patterning 34

2.2.2.3. Surface Treatment and Adhesion 35

2.2.3. Detailed Processing Examples 37

2.2.3.1. Example 1—Single Microchannel Fabrication 37

2.2.3.2. Example 2—Valve Fabrication 39

2.2.3.3. Example 3—High-Pressure Microfluidics 45

2.2.3.4. Example 4—SU-8 Fluidic Ports 49

2.2.4. Common Problems 52

2.2.4.1. Adhesion Issues 52

2.2.4.2. Heating Issues 52

2.2.4.3. Photoresist Dissolution 53

2.2.4.4. Conformality 54

2.3. Device Examples 54

2.3.1. Sensors 54

2.3.2. Pumps 56

2.3.3. Valves 57

2.3.4. External Detector Interfacing 57

2.3.5. Passive Fluidic Structures 58

2.4. Conclusions 58

Chapter 3: Microfluidic Chip for Flow Control Applications 60

3.1. Introduction ... 60

3.2. Experimental ... 62

3.2.1. Chip Design ... 62

3.2.2. Chip Fabrication ... 65

3.2.3. Composition Sensor ... 68

3.2.4. Flow Sensor ... 69

3.2.5. Sensor Calibration ... 70

3.2.6. Chip Packaging ... 71

3.3. Results and Discussion ... 72

3.3.1. Mixer ... 72

3.3.2. Composition Sensor ... 72

3.3.3. Flow Sensor ... 76

3.4. Conclusion ... 81

Chapter 4: High-Pressure Electrolysis Pumping ... 82

4.1. Introduction ... 82

4.1.1. Electrolysis of Water ... 84

4.2. Experimental ... 85

4.2.1. Device Design ... 85

4.2.2. Chip Fabrication ... 86

4.2.3. Pump Packaging ... 86

4.2.4. Pump Calibration ... 88

4.3. Results and Discussion ... 89

4.4. Conclusion ... 100

Chapter 5: Multi-Function Microfluidic Platform for Liquid Chromatography Tandem Mass Spectrometry (LC-MS/MS) ... 102
5.1. Introduction ... 102
5.2. Experimental ... 104
5.2.1. Chip Design ... 104
5.2.2. Chip Fabrication ... 108
5.2.3. Chip Packaging / Preparation ... 112
5.2.4. Sensor Operation ... 112
5.2.5. Pneumatic Pump ... 112
5.2.6. Mass Spectrometry ... 113
5.2.7. Data Acquisition ... 114
5.2.8. Chip Separation Configurations ... 115
5.2.8.1. Standard Column with Active Sensors ... 115
5.2.8.2. Vented Column with Non-Active Sensors ... 116
5.2.8.3. Standard Column with On-Chip Feedback-Controlled Flow Control ... 118
5.3. Results and Discussion ... 119
5.3.1. Microfluidic Chip/Components ... 119
5.3.1.1. Analytical/Trap Column ... 120
5.3.1.2. Bead Filter ... 120
5.3.1.3. Electrospray ... 121
5.3.2. Standard Column with Active Sensors ... 122
5.3.3. Vented Column with Non-Active Sensors ... 124
5.3.4. Feedback-Controlled Operation ... 125

5.3.5. Standard Column with On-Chip Feedback-Controlled Flow Control 128

5.4. Conclusion 131

Chapter 6: Portable High-Performance Liquid Chromatography Conductivity Detection (HPLC-CD) System 133

6.1. Introduction 133

6.2. Experimental 135

6.2.1. Modular System / Individual Chip Design 135

6.2.2. Chip Fabrication 137

6.2.3. Chip Packaging / Preparation 138

6.2.4. Electrolysis Pump Operation 138

6.2.5. Flow Control Chip Operation 138

6.2.6. Detector Operation 139

6.2.7. Chip Separation Configurations 139

6.2.7.1. Separation with Conventional HPLC Pump 140

6.2.7.2. Separation with Electrolysis Pumps 141

6.2.8. Data Acquisition and Computer Control 143

6.3. Results and Discussion 144

6.3.1. Microfluidic Chips/Components 144

6.3.1.1. Conductivity Detector 144

6.3.2. Separation with Agilent HPLC Pump 146

6.3.3. Separation with Electrolysis Pumps 148

6.4. Conclusion 154

Chapter 7: Conclusion 155

Chapter 8: References 156

Figures / Tables

Figure 1-1: The different interfacial forces acting on a fluid in a microchannel 5

Figure 1-2: Diagram showing the principle of EOF 7

Figure 1-3: Fabrication of a microchannel using bulk micromachining and anodic bonding 11

Figure 1-4: Fabrication of a microchannel using a surface micromachining process 13

Figure 1-5: Fabrication of a microchannel using soft lithography 14

Table 1-1: Typical column sizes for HPLC 23

Figure 1-6: Diagram of a basic binary HPLC system. Shown on the bottom is an actual Eksigent NanoLC system with diagram of its internal components. 24

Figure 1-7: Comparison between isocratic and gradient elutions 25

Figure 2-1: Chemical structure of common Parylene monomers 28

Table 2-1: Key properties of Parylene C 29

Figure 2-2: Diagram showing the Parylene deposition process 33

Figure 2-3: Process flow for single microchannel fabrication 37

Figure 2-4: Process flow for valve fabrication 40

Figure 2-5: Process flow for high-pressure-capable microchannel 46

Figure 2-6: Process flow showing the creating of SU-8-based ports at the inlet/outlet of a microchannel 49

Figure 2-7: A diagram showing the fluidic packaging concept 51

Figure 2-8: Picture and cross section of a flow control system consisting of an electrostatic valve (left) and thermal flow sensor (right) 55

Figure 2-9: Picture and cross section of an electrostatically actuated peristaltic pump. Individual chambers also can serve as pressure sensors. 56

Figure 2-10: Picture and cross section of a normally closed passive check valve 57

Figure 2-11: Picture and cross section of an electrospray nozzle 58

Figure 3-1: A picture and diagram of both the described chips. The various components are highlighted blue (mixer), green (composition sensor), and red (flow sensor). Both chips were 9.8 x 9.8 (L x W) mm^2. A. Integrated chip. B. Standalone chip.......... 63

Figure 3-2: A close-up picture of all the sensor designs presented in this chapter. All devices are shown at the same scale. 64

Figure 3-3: Process flow showing the fabrication of the standalone device. The left-hand column shows a cross-sectional view where the liquid flow is from left to right. The right-hand column shows a cross-sectional view where the flow is into the page. 65

Figure 3-4: Packaged standalone device and close-up view of the electrode block........ 71

Figure 3-5: Equivalent circuits for the composition sensor. C_{dl} is the double layer capacitance, R_l is the fluid resistance, C_p is the parasitic capacitance, and L is an external inductor only used in the resonant-enhanced measurement circuit 73

Figure 3-6: Example calibration plots for the composition sensors on the integrated device (500 kHz, 200 mV with resonant circuit) and standalone device (100 kHz, 200 mV with non-resonant circuit). 74

Figure 3-7: Sample waveforms collected using the integrated device. The different waveforms correspond to different fluid compositions ranging from 0–50% acetonitrile (10% intervals). A flow rate of ~ 140 nL/min was used to generate all the waveforms. The pulse was generated at t = 0 ms. 76

Figure 3-8: Sample waveforms comparing the response of the integrated device and standalone device. Both waveforms were collected at a flow rate of 140 nL/min and using a 10% acetonitrile solution. The pulse was generated at t = 0 ms. 77

Figure 3-9: Flow sensor calibration plots for both the integrated and standalone devices. The TOFs correspond to the peak position. The points are fitted (solid line) assuming an ideal inverse relationship between TOF and flow rate. The dotted line represents the expected TOFs based only on the physical sensor dimensions and flow rate. 79

Figure 3-10: Sample waveforms collected using the flow sensor on the standalone device. The flow rate was 140 nL/min for all waveforms and a 10% acetonitrile solution was used. The pulse was generated at t = 0 ms. 80

Figure 4-1: Different classes of microfluidic pumps and their corresponding maximum backpressures and flow rates 82

Figure 4-2: A picture of the electrode array.. 86

Figure 4-3: A picture of the packaged electrolysis pump along with a cross-sectional view. The electrolysis chamber is faintly visible in the center of the Ultem piece. 87

Figure 4-4: A plot showing the increase in pressure inside the closed electrolysis system at applied currents of 1, 2, and 3 mA. These three curves were collected using a 100% water solution (0.1% formic acid). 89

Figure 4-5: Comparison between mathematical model and actual data (Figure 4-4). The model results are shown in the solid black lines.. 93

Figure 4-6: A plot showing the flow rate, pressure, and current relationship for the electrolysis pump. Also on the plot are single point calibrations to check the accuracy of

the mathematical model. The discrete points are colored corresponding to the applied current. 95

Figure 4-7: Plot of molecular efficiency as a function of pressure and current. Each of the curves corresponds to a different applied electrolysis current. 97

Figure 4-8: I-V curve for the electrolysis device 98

Figure 4-9: Plot showing the power efficiency of the electrolysis pump at various pressures and currents 99

Figure 5-1: A picture and diagram of the presented chip. The various components are highlighted in blue (mixer), green (composition sensor), red (flow sensor), orange (trap column), purple (analytical column), brown (electrodes for applying electrospray potential), yellow (electrospray nozzle), and gray (bead filters). The black dots represent the location of fluidic ports. Overall chip size was 9.8 x 9.8 mm^2. 105

Figure 5-2: Close-up pictures of all the individual components on the presented chip. All devices are shown at the same scale. 106

Figure 5-3: Process flow for the presented chip. The left-hand column shows a cross-sectional view where the liquid flow is from left to right. The right-hand column shows a cross-sectional view where the liquid flow is into the page. 108

Figure 5-4: A picture of the custom-built two-channel pneumatic pump 113

Figure 5-5: A picture of the chip/mass spectrometer interfacing 114

Figure 5-6: Fluidic configuration and separation method for the "Standard Column with Active Sensors" configuration 115

Figure 5-7: Fluidic configuration and separation method for the “Vented Column with Non-Active Sensors” configuration. V1 is internal to the autosampler but is shown separately for clarity. 117

Figure 5-8: Fluidic configuration and separation method for the “Standard Column with On-Chip Feedback-Controlled Flow Control” configuration........ 118

Figure 5-9: Separation results using the “Standard Column with Active Sensors” configuration. The MS data (top), flow sensor (bottom right), and composition sensor (bottom left) data are plotted........ 122

Figure 5-10: Separation results using the “Vented Column with Non-Active Sensors” configuration. The MS data for three different sample concentrations are plotted. 125

Figure 5-11: Equivalent electrical circuit for the fluidic system 126

Figure 5-12: Comparison between the pressures obtained during feedback drive operation of a 0 to 30% acetonitrile gradient (solid lines) versus the pressure calculated using a mathematical model (dotted lines). 127

Figure 5-13: Separation results using the “Standard Column with On-Chip Feedback-Controlled Flow Control” configuration. The MS data (top), flow sensor (middle left), composition sensor (middle right), and pump pressure (bottom) data are plotted. 129

Figure 6-1: A picture and diagram of the presented separation/detection chip. The various components are highlighted in purple (analytical column), gray (bead filter), and red (conductivity detector). The black circles represent the location of the inlet and outlet ports........ 135

Figure 6-2: Close-up pictures of all the individual components on the column/detection chip. The larger (70 x 1000 (W x L) μm^2) detector is shown here. All devices are shown at the same scale.. 136

Figure 6-3: Process flow for the separation/detection chip. The left-hand column shows a cross-sectional view where the liquid flow is from left to right. The right-hand column shows a cross-sectional view where the liquid flow is into the page............................. 137

Figure 6-4: Diagram of the commercial HPLC pump-driven setup along with the separation method. An inset showing the operation principle of the injection valve is also included.. 140

Figure 6-5: Diagram of the electrolysis pump-driven setup along with the separation method. An inset showing the operation principle of the injection valve is also included. 142

Figure 6-6: A photograph of the entire separation system... 143

Figure 6-7: Detector response at different aqueous concentrations of $[H^+]/[COOH^-]$. 0.1% formic acid in water corresponds to 2.1 mM... 145

Figure 6-8: Separation of a five-peptide sample. The raw detector and baseline signals (top left) are shown along with the compensated detector signal (top right). Also shown are the composition (bottom left) and flow rate (bottom right) as indicated by the integrated sensors... 146

Table 6-1: Digital control algorithm for electrolysis pumps 151

Figure 6-9: Separation of a five-peptide sample. The raw detector and baseline signals (top left) are shown along with the compensated detector signal (top right). Also shown are the composition (middle left), flow rate (middle right), pump-driving currents (bottom

left), and pump pressures (bottom right). To better show the trend, pump currents were fitted with a 5 min moving average. 152

Figure 6-10: Comparison between the actual electrolysis pump pressures and the calculated ones 153

Chapter 1: Introduction to Microfluidics

1.1. Introduction

Microfluidics is the study of fluid behavior/manipulation at sub-mm length scales. Initially, the study of small-scale fluid transport was driven by the need to understand natural phenomenon such as blood flow in human capillaries, water/mineral transport in plants, and colloids. In the 1980s, the development of microfabrication technologies allowed man-made microfluidic devices and systems to be created. These new technologies enabled the further study of microfluidic phenomenon and also spurred the development of miniature fluidic components such as pumps, valves, and mixers. More recently, the focus has shifted to applying the numerous developed technologies and devices towards biotechnology-related tasks. The development of microfluidic chips that can replicate the analyses being done in a conventional laboratory, so-called lab-on-a-chip devices or micro total analysis systems, is currently the driving force behind most microfluidic research[1].

The miniaturization of analytical systems has many potential advantages. Some analytical tasks are theoretically expected to demonstrate improvements in performance on smaller scales. Reducing the scale of the analysis also has the benefits of reduced sample and reagent consumption. The small overall size also allows systems to be portable, allowing on-the-spot analysis. Finally, the ability to integrate an entire analytical procedure onto a single device has the potential to drastically reduce the overall analysis cost.

This chapter will begin with a discussion of some key microfluidic principles. Next, some of the most widely used fabrication technologies used to create microfluidic devices and systems will be introduced. This will be followed by a discussion of common microfluidic devices. Finally, special attention will be paid to high-performance liquid chromatography (HPLC), which holds a central theme in this thesis, and its relation to microfluidics.

1.2. Microfluidic Phenomena

Forces that are commonly seen in macroscale fluids can be inconsequential on the microscale. For example, turbulence, which is commonly found in everyday life, rarely exists in microfluidic systems. Likewise, the opposite can be true, and forces that usually play a small role in macroscale fluids can become significant and in some cases dominate in microfluidics. For example, surface tension and electrokinetic forces become more apparent in the microscale and in many cases can be exploited.

1.2.1. Laminar Flow

Microfluidic devices by nature have a very low Reynolds number, the value of which gives an indication of the flow regime (e.g., laminar, turbulent). The Reynolds number is defined as

$$\mathrm{Re} = \frac{\rho v D_h}{\mu}, \text{ (equation 1)}$$

where Re is the Reynolds number, ρ is the fluid density, v is the velocity of the fluid, D_h is the hydraulic diameter, and μ is the fluid viscosity. Microfluidic flows generally have a Reynolds number of < 1 and are almost always laminar. The biggest consequence of

laminar flow is that when two or more fluid streams combine, there is no turbulent mixing. Mass transport between the two streams will be by diffusion alone.

Low-Reynolds-number, pressure-driven, incompressible flows can be described by the Stokes equations,

$$\begin{aligned} \nabla p &= \mu \nabla^2 \vec{v} + \vec{f} \\ \nabla \cdot \vec{v} &= 0 \end{aligned} \text{, (equation 2)}$$

where p is the fluid stress, μ is the fluid viscosity, v is the velocity, and f is the applied body force. Analytical solutions of the Stokes equations, assuming no-slip boundary conditions, have been obtained for channel geometries commonly encountered in microfluidic devices. In all cases, the flow has a parabolic velocity profile. The bulk flow through these channel geometries can be described using the concept of fluidic resistance, where the flow through a given channel geometry is proportional to the pressure drop over the channel and inversely proportional to the fluidic resistance, or

$$Q = \frac{\Delta P}{R} \text{, (equation 3)}$$

where Q is the flow rate, ΔP is the pressure drop, and R is the fluidic resistance. For circular channel geometries the fluidic resistance is found to be

$$R_{circ} = \frac{8\mu L}{\pi r^4} \text{, (equation 4)}$$

where R_{circ} is the fluidic resistance of a circular channel geometry, μ is the fluid viscosity, L is the channel length, and r is the radius of the microchannel. The resistance of a low-aspect-ratio rectangular microchannel (w>>h), another geometry often encountered in microfluidic devices, is found to be

$$R_{rec} = \frac{12\mu L}{wh^3} \text{, (equation 5)}$$

where R_{rec} is the fluidic resistance of a rectangular microchannel, μ is the fluid viscosity, L is the channel length, w is the channel width, and h is the channel height[2]. With channel dimensions on the μm scale, the fluidic resistance can be very significant. For example, a 1-cm-long rectangular microchannel with a cross section of 100 x 5 (W x H) μm^2 would need a pressure of 167 kPa to produce a 1 μL/min flow of water.

The concept of fluidic resistance is useful for describing the splitting and combining of flows in pressure-driven microfluidic systems. Networks of channels can be analyzed using the same principles used to solve electrical circuits because of the similarities between equation 3 and Ohm's law. Basic rules used to solve electrical circuits, such as Kirchhoff's first and second rules can be applied to microfluidic "circuits" as well. Kirchhoff's first rule applied to microfluidics would simply demand that the sum of flows going into any junction is equal the sum of flows going out, while Kirchhoff's second rule would imply that the sum of the pressure drops over any closed microfluidic circuit must be zero. In some cases, electrical components such as capacitors, inductors, and diodes can also be used to model microfluidic behavior.

1.2.2. Multiphase Interfaces

At a liquid/gas interface, the surface tension will give rise to a distortion of the liquid/gas boundary. The relationship between the equilibrium pressure difference across the interface and curvature is described by the Young-Laplace equation,

$$\Delta P = \gamma\left(\frac{1}{r_1} + \frac{1}{r_2}\right), \text{ (equation 6)}$$

where ΔP is the differential pressure, γ surface tension, and $r_{1,2}$ are the principal radii of curvature of the liquid/gas interface[2].

In microfluidics, we often encounter liquid/solid/gas interfaces, such as a droplet of water on a solid surface, or a column of liquid in a partially filled microchannel. The balance of surface tension forces results in a characteristic contact angle at the liquid/solid/gas interface. If the adhesive forces between the liquid and solid are greater than that of the cohesive forces in the liquid, the contact angle will be < 90°. If the opposite is true, the contact angle will be > 90°. For the specific case of water as the working fluid, the solid is described a hydrophilic if the contact angle is < 90° and hydrophobic if it is > 90°.

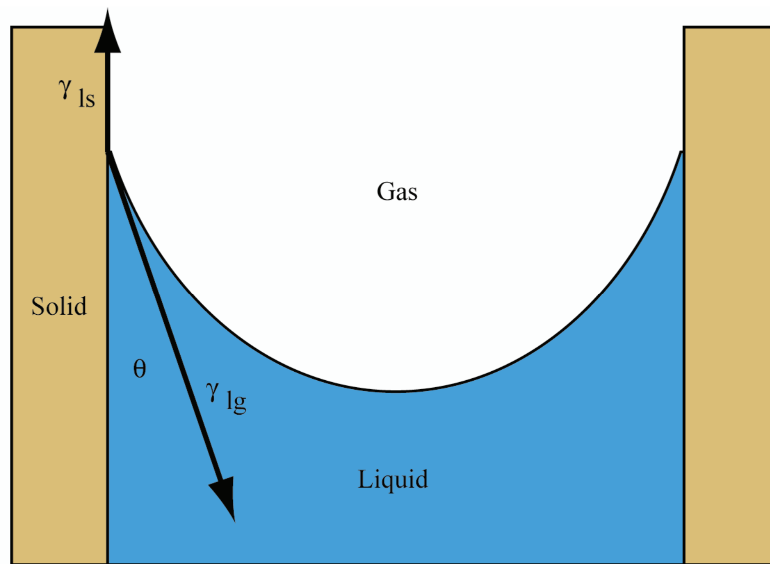

Figure 1-1: The different interfacial forces acting on a fluid in a microchannel

The balance of forces at the liquid/solid/gas interface can be described mathematically. For the case of a liquid column in a partially filled microchannel as seen in Figure 1-1, this balance of forces can be written as

$$\gamma_{ls} = \gamma_{\mathrm{lg}} \cos\theta \text{, (equation 7)}$$

where γ_{ls} is the liquid/solid interface surface tension, γ_{lg} is the liquid/gas interface surface tension, and θ is the contact angle. The exerted pressure can be calculated using equation 6. For a circular microchannel, the pressure can be expressed as

$$\Delta P = \frac{2\gamma_{ls}}{r}, \text{ (equation 8)}$$

where ΔP is the pressure, γ_{ls} is the liquid/solid interface surface tension, and r is the radius of the circular microchannel. One thing that becomes clear is that at smaller channel dimensions, the pressure becomes larger and larger. For example, a 100 µm ID glass capillary in contact with water will generate a pressure of nearly 3 kPa, which is enough to support a column of water 30.6 cm in height.

1.2.3. Electrokinetics

Electrokinetics refers to the coupling between electric currents and fluid flows in an electrolyte. The most common electrokinetic phenomenon is electro-osmosis, which refers to the generation of fluid flow via the application of an electric field. Electro-osmotic flow (EOF) is one of the primary methods of transporting fluids in microchannels.

EOF is dependant on the formation of a double layer at the liquid/solid interface. For example, glass in the presence of water at low pH will exhibit a negatively charged surface consisting of SiO^- groups. The free positive ions in the water are attracted to the negatively charged surface and will form a layer of equal and opposite charge. These layers of charge form what is called a double layer. The thickness of the double layer is defined as the Debye length, which is inversely proportional to the square root of the ion concentration and is generally < 100 nm for aqueous solutions. Applying an electric

field along the direction of the channel causes the positive ions in the double layer to move towards the cathode. This movement of ions carries the bulk fluid along with it generating net flow. This process is illustrated in Figure 1-2.

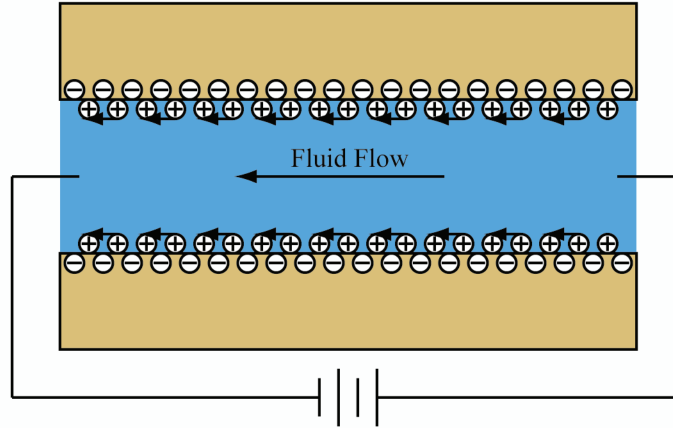

Figure 1-2: Diagram showing the principle of EOF

The fluid velocity is assumed to be zero at the liquid/solid surface. Towards the edge of the double layer (e.g., one Debye length away from the liquid/solid interface), the fluid velocity can be written as

$$\vec{v} = -m\vec{E}\text{, (equation 9)}$$

where v is the velocity, m is the mobility of the ions, and E is the electric field. This is effectively the same velocity that the bulk fluid moves at as well, provided that the dimensions of the channel are not too large. The ion mobility can be expressed as

$$m = \frac{\sigma_s \lambda_D}{\mu} = \frac{\zeta k \varepsilon_o}{\mu}\text{, (equation 10)}$$

where m the mobility of the ions, σ_s is the surface charge density, λ_D is the Debye length, μ is the fluid viscosity, ζ is the zeta potential, k is the relative dielectric constant of the liquid, and ε_o is the permittivity of free space. For most aqueous systems the zeta

potential is on the order of 10 mV, yielding a mobility on the order of 10^{-4} $cm^2/(s\text{-}V)$. A 1 kV/cm electric field would therefore yield a fluid velocity of 1 mm/s.

EOF is common in microfluidics because of its simplicity. Changes in flow are made by simply changing the magnitude of the applied voltage. Another advantage of EOFs is that the velocity profile is constant across the entire microchannel cross section. This allows plugs of material to be transported from one place to another with minimal distortion[1].

1.3. Fabrication Technologies

Many different methods have been developed to fabricate microfluidic devices and systems. The earliest attempts in the 1980s used microfabrication techniques borrowed from the MEMS (MicroElectroMechanical Systems) field, which itself used techniques borrowed heavily from the semiconductor industry[3]. Bulk micromachining[4], which usually involves the etching of silicon or glass and the subsequent bonding of two or more different elements, was the method of choice for early microfluidic studies. Surface micromachining techniques[5] were also used for microfluidic applications. It involves the repeated deposition and patterning of thin-film materials on a substrate to build up 3-D structures. In the last several years, the micro-molding and bonding of elastomers, dubbed soft lithography[6], has also been studied and utilized heavily in the creation of microfluidic devices. Finally, conventional polymer processing methods such as hot embossing, injection molding, and casting have been applied to microfluidics as well.

One common aspect of these different fabrication methods, with the exception of the conventional polymer processing techniques, is that they all generally rely on photolithography to produce the microscopic patterns required. Photolithography involves the use of a photosensitive polymer called photoresist, which is spin-coated on a substrate. Exposure of the polymer through a mask can make the corresponding exposed regions soluble or insoluble in a developer solution. The patterned photoresist can be used as a structural or sacrificial material itself, or used to pattern other materials through various etch processes.

1.3.1. Bulk Micromachining

Bulk micromachining refers to the etching of a substrate to create a trench, hole, or other structure. The most popular substrate is silicon because of the wide variety of isotropic and anisotropic etches available. Wet and plasma etching methods are the most common.

Wet etching of silicon can be done using many different solutions, the most common include: HNA (HF, HNO_3, and CH_3COOH), KOH, EDP (Ethylene-diamine pyrochatechol), and TMAH ($(CH_3)_4NOH$). HNA is isotropic, meaning that it etches all crystal orientations of silicon equally. KOH, EDP, and TMAH are all anisotropic, etching the {111} planes of silicon ~ 30–100x slower than the {100} planes. This anisotropy can be exploited to create structures such as grooves with sidewalls corresponding exactly to the {111} planes. Depending on the etchant, silicon oxide, silicon nitride, photoresist, or a number of other materials may be used as a mask.

Plasma etching of silicon is also widely utilized. The main etch chemistry used is based on SF_6. In the highly energetic plasma state, SF_6 reacts with silicon to form the gaseous product SiF_4. Different plasma configurations can allow for etches with varying degrees of isotropy, ranging anywhere from isotropic to completely directional. This anisotropy can be achieved, for example, by using reactive ion etching (RIE), which involves the acceleration of the SF_6 towards the substrate, leading to more vertical sidewalls. Deep reactive ion etching (DRIE), a variation on RIE, alternates SF_6 with C_4F_8 plasmas. This switched plasma etching chemistry allows for almost perfectly vertical trenches.

Bonding of multiple layers is usually required in bulk micromachined microfluidic devices. Anodic bonding is the most popular bonding technique and is a method for joining a silicon substrate with a Na^+-based glass such as Pyrex. The bonding process begins with the careful cleaning of both surfaces, with particular attention to removing the native oxide from the silicon substrate. The glass and silicon are then placed in contact with each other and heated to 200–500 ºC. A high potential, generally between 500–1500 V, is then applied across the bonding interface, with the more positive potential on the silicon. This causes the mobile Na^+ ions in the glass to migrate towards the cathode and away from the silicon/glass interface. This migration of ions leaves a fixed negative charge in the glass at the bonding surface. The electrostatic attraction between the negatively charged glass surface and the positively charged silicon keeps the two substrates bonded. Some chemical bonding at the silicon/glass interface occurs due to the close proximity of the two substrates.

The combination of bulk etching with wafer bonding can be used to produce many basic microfluidic components. One of the earliest examples of a microfabricated analytical system was a spiral column for use in gas chromatography[7]. HNA, with silicon oxide as a mask, was used to etch trenches into a silicon substrate. A Pyrex substrate was then used to cap off the channels using anodic bonding. This process is shown in Figure 1-3.

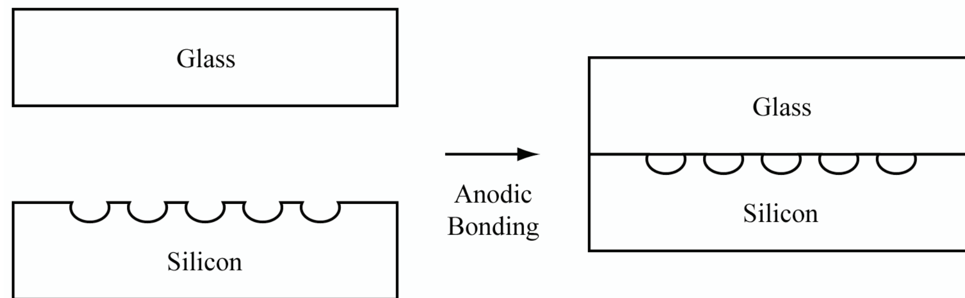

Figure 1-3: Fabrication of a microchannel using bulk micromachining and anodic bonding

1.3.2. Surface Micromachining

Surface micromachining generally consists of the deposition and patterning of alternating layers of a sacrificial and structural material. At the end of the process, the sacrificial material is removed using a selective etch/dissolution process, leaving only the structural material intact. Two main surface micromachining technologies have been used for microfluidic applications. The first involves using polysilicon as the structural material and silicon oxide as the sacrificial material. The second is completely polymer-based and uses Parylene/photoresist as the structural/sacrificial materials.

Surface micromachining using polysilicon and silicon oxide has been one of the most commercially successful methods of making MEMS devices. Both polysilicon and

silicon oxide can be deposited using chemical vapor deposition (CVD), which involves the deposition of thin films on a substrate from the gaseous phase. CVD of polysilicon is accomplished by using SiH_4, which is pyrolized at 550–700 ºC to form polysilicon layers up to several μm thick. The exact temperature determines the crystalline structure. Patterning can be accomplished using SF_6 plasma. Deposition of silicon oxide is accomplished using a mixture of SiH_4 and O_2, generally at temperatures < 500 ºC. Patterning is accomplished using HF. For both the CVD deposition of polysilicon and silicon oxide, dopants can be added by introducing gases such as PH_3 or B_2H_6 during the deposition process. The resulting polysilicon will either be p-type or n-type, respectively. When used during silicon oxide deposition, phosphosilicate glass (PSG) or borophophososilicate glass (BPSG) can result[8]. These dopants can be used to change the conductivity or etch characteristics of the material. Removal of the oxide sacrificial layers at the end can be accomplished using HF.

Parylene/photoresist surface micromachining is a second method that has been widely used to make microfluidic devices. Parylene is deposited using a room-temperature CVD process. Gas-phase Parylene monomers are produced via the pyrolysis of a stable Parylene dimer. The monomers then deposit as a polymer film on any substrate. Thicknesses ranging from < 100 nm to > 100 μm can be deposited, with patterning usually accomplished using O_2 plasma. Photoresist, the sacrificial layer, is spin coated and patterned using photolithography. Removal of the sacrificial photoresist can be achieved using acetone or other solvent. This fabrication technology is used for making all the devices in the subsequent chapters and will be discussed in great detail in Chapter 2.

As an example, the fabrication of a microchannel using surface-micromachining is depicted in Figure 1-4. Starting with a silicon substrate, a sacrificial material is deposited and patterned. A layer of the structural material is then deposited, completely encapsulating the sacrificial layer. After patterning the structural material to open the ends of the channel, the sacrificial material can then be dissolved or etched away. This simple process can be abstracted to include many more layers and used to make 3-D microfluidic structures.

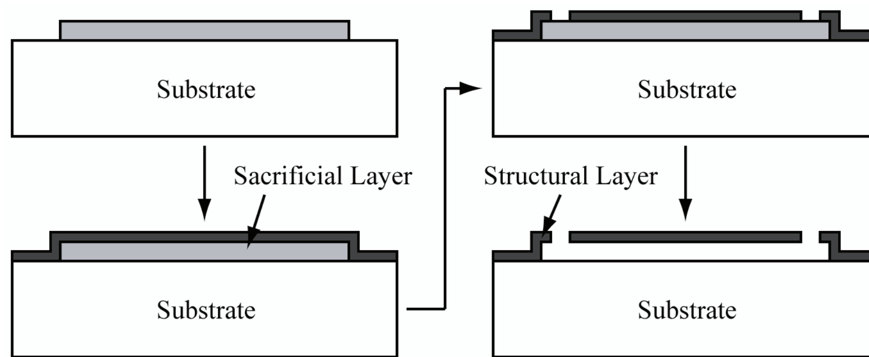

Figure 1-4: Fabrication of a microchannel using a surface micromachining process

1.3.3. Soft Lithography

The replica molding of Poly(dimethylsiloxane) (PDMS) has gained a lot of attention in the last several years as a method to create microfluidic systems, mainly because of its simplicity and fast production time. The process generally begins with the creation of a master mold using standard photolithography-based processes. Molds can range from patterned photoresist on a silicon substrate to bulk micromachined silicon. This mold is then used to cast a PDMS piece. Common PDMS formulations such as Sylgard 184 are generally cast using a two-part mixture consisting of a polymer base and hardener mixed in a 10:1 ratio. Complete curing can be achieved in 1 hr at 100 ºC. After

removal from the mold, the PDMS piece can be bonded with other PDMS pieces or to a solid substrate.

Glass is commonly used as the substrate to bond PDMS pieces to. Several bonding methods exist. The most simple is simply wetting both the glass and PDMS and joining the two pieces. As the liquid dries, the stiction forces will keep the two components bonded together. If a more robust bond is needed, oxygen plasma or chemical treatments can be used to make both the PDMS and glass pieces hydrophilic. The two pieces are then placed in contact with each other and are held together through hydrophilic interactions. For more complex devices, PDMS/PDMS bonding is sometimes needed. One method of joining two PDMS pieces is by casting the two pieces using a non-standard base:hardener ratio, one with a slightly higher than needed base component and the other with a higher than normal hardener ratio. When these two pieces are joined together and further cured, the residual PDMS components will cure at the boundary creating a monolithic structure.

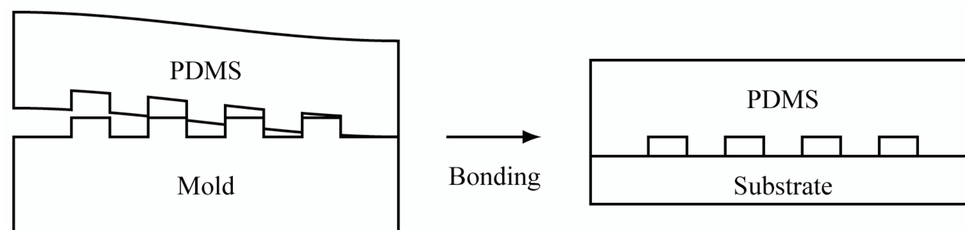

Figure 1-5: Fabrication of a microchannel using soft lithography

The process to create a network of microfluidic channels using soft lithography is shown in Figure 1-5. After a mold has been made and a PDMS part has been cast, the PDMS piece is bonded to a glass substrate. The resulting channels can be accessed by punching holes through the entire PDMS piece. Components such as valves can be

realized by adding a second PDMS piece above the first one to create a top control channel, which crosses perpendicular to the bottom fluid channel. Pneumatic actuation of the top control channel can be used to collapse the bottom fluid channel, effectively closing off the fluidic pathway[6, 9].

1.3.4. Other

In addition to the previously discussed methods, numerous other technologies have been used for microfluidic applications. Techniques such as hot embossing, injection molding, and casting (soft lithography being an example) are often used. Also, more direct micromachining methods such as laser ablation and micro-milling have also found use. These techniques are mostly targeted towards polymer-based microfluidic devices. Polymers that can be used include polyamide, polycarbonate, cycloolefin copolymer, polymethylmethacrylate, and many others. Because many of these technologies are based on well-developed conventional polymer-processing methods, this has made them the choice for most commercially available microfluidic assays and micro analytical systems on the market today[10]. One drawback of these methods is that they are not able to achieve the same levels of complexity a photolithography-based technology is capable of.

1.4. Microfluidic Components

Microfluidic devices can be broken down into four main categories: handling, sensing, interfacing, and processing. The full extent of devices demonstrated to date is too great to be covered here. Not only are there many approaches for each particular task,

but each approach can be realized using several different fabrication technologies as well. An effort will be made here to briefly summarize some of the more common devices as well as their operating principles.

1.4.1. Fluid Handling

Fluid handling refers to devices that are used to physically control the movement of fluid. This includes components such as microchannels, valves, and pumps. Microchannels are the most basic component of any microfluidic system and are analogous to the pipes used in household plumbing systems. They are used to physically transport fluid from one place to another in a microfluidic network.

Valves can be classified into one of two categories: active and passive. Active valves are those which can be actuated, selectively closing off or opening the flow path. The general design principle of microfluidic valves uses the action of a movable mechanical structure that can be used to shut off flow. Usually this involves the creation of structures such as flaps, membranes, and plugs that can be actuated to cover or open an orifice. These structures can be actuated using many mechanisms, including magnetic, electrostatic, pneumatic, piezoelectric, thermal, electrochemical, and phase change. Passive valves on the other hand generally refer to check valves, which rectify the flow without any outside actuation force. Like an active valve, check valves generally consist of a moving flap, membrane, plug, or even ball that can move to cover or reveal an opening. Instead of being actuated, passive valves open and close depending on the flow direction, relying on hydrodynamic forces and built in stresses to change position[11].

Microfluidic pumps can be broken down into two categories, mechanical and non-mechanical. Most mechanical pumps are based on the same principles used in everyday pumps. Check-valved pumps consist of an actuate-able fluid chamber with check valves at the inlet and outlet. The check valves are oriented in the same direction so that flow is rectified during the compression and expansion steps of the actuator. Peristaltic pumps function through the wave-like actuation of a series of actuators. Rotary pumps use the spinning action of a gear or impeller to move fluid. The actuation of mechanical pumps, like active valves, can be implemented using a variety of different forces. On the non-mechanical side, electro-osmotic pumping is the most common. It uses an electric field to move surface charges on the channel sidewalls, which "carries" the surrounding fluid with it via solvent drag. Electrohydrodynamic (EHD) pumps rely on the electrostatic force exerted on a fluid when exposed to a changing electric field. Pumps based on the creation of gas to displace fluid have also been demonstrated. Gas can be formed through chemical, electrochemical, or thermal means[12, 13].

1.4.2. Fluid Sensing

Sensors can be divided up into two different categories, ones that measure physical properties of the fluid and others that measure chemical properties. Important physical properties include pressure, flow rate, temperature, viscosity, and density. Pressure sensors in microfluidics generally rely on measuring the deflection of a membrane when subjected to a differential pressure. Common methods of measuring the deflection include optical, piezoresistive, capacitive, and strain gauges. Flow sensors based on many different operating principles have also been demonstrated. These

include ones that operate based on calorimetric principles, time-of-flight sensors which measure the velocity of a tracer pulse, and sensors that measure the differential pressure across a fixed fluidic resistance. Temperature measurements can be conducted using miniaturized thermistors and thermocouples. Viscosity can be measured by using oscillating structures to measure the damping forces. Density and/or mass can be measured by using a hollow resonator structure that fluid passes through.

Chemical sensors are used to measure the contents of a particular fluid. This includes universal detection and the specific detection of a particular molecule or class of molecules. Electrochemical detectors are used to measure molecules that can be oxidized or reduced. Conductivity sensors and sensors based on field effect transistors have been used for measuring the ion content or pH of a fluid. Sensors with exposed electrodes are often coated with a semi-permeable and/or functionalized membrane to increase specificity. Acoustic wave sensors are also widely used and quantify the amount of adsorbed molecules on a surface by measuring the propagation characteristics of an acoustic wave. Optical detectors, which use light-sensitive elements, light sources, and concentration/collection optics, have also been developed for common optical-based measurements of fluids, such as absorbance, transmission, and fluorescence. Also, cantilever-based sensors, which use the resonance characteristics of a functionalized cantilever, have been used for the detection of specific molecules[14].

1.4.3. Fluid Interfacing

Reliable interfacing between a microfluidic chip and the outside world is one of the most critical aspects of developing microfluidic systems. Fluidic connections are

used to introduce liquid from outside sources onto the chip or send the processed fluid to another instrument. The earliest methods used bulk micromachined ports in which tubes could be inserted and bonded using adhesives. Microfabricated interlocking structures were also developed and used instead of adhesives to keep the tubing in place. Microfluidic manifolds, which can be clamped or glued to a microfluidic chip to access the inlets/outlets, are also used.

It is also important to be able to interface microfluidic chips with specialized detectors, particularly those which are difficult to integrate onto a chip. While many external instruments can simply be connected to a microfluidic chip using a tube, some instruments require unique interface devices. Electrospray emitters, which interface chip-based analyses with a mass spectrometer, have been developed. Devices to analyze on-chip fluid using a conventional NMR machine have also been demonstrated. Optical detection methods such as UV absorbance and laser-induced fluorescence (LIF) have also been successfully used to measure fluids through the use of chip-based optical flow cells[15].

1.4.4. Fluid Processing

Fluid processing is a very broad term and refers to the steps needed to process a sample, often biological in origin. Some key steps include extraction, concentration, mixing/reacting, and separation.

The need to concentrate and purify raw samples is a very important task in the life sciences. Molecules of interest are often only present in very low abundance and can be masked by the molecules of high abundance. One popular method is to use a

functionalized solid phase to capture molecules from the fluid. The solid phase can range from the channel sidewalls themselves, to porous polymers that are polymerized on-chip, to specially coated beads immobilized in a device. The capture of molecules from solution can be based on any number of interactions including hydrophobic/hydrophilic interaction or antibody/antigen binding. Miniaturized dialysis systems, which use a semi-permeable membrane, have also been used to clean up raw samples. Electrically driven concentration techniques have also been studied. For example, the use of nanochannels with dimensions comparable to the Debye length have been used to concentrate molecules based on electrokinetic principles[16].

Mixers, like many of the other discussed components can be broken into passive and active categories. Because microfluidic systems almost always function in the laminar flow regime, passive mixers rely on diffusion. Designs are optimized to maximize the contact area between the two incoming flows to increase diffusion and, as a result, the mixing efficiency. Methods of doing this include laminating the flows and the injection of one flow into the other using an array of nozzle-like structures. Active mixers use external forces to disturb the flow to enhance the mixing speed. Pressure-induced disturbances are often achieved by incorporating a mechanical actuator, much like those found in active valves and mechanical pumps. Electric and/or magnetic fields can also be used to improve mixing, and active mixers based on EHD, dielectrophoretic (DEP), electrokinetic, and magneto hydrodynamic (MHD) forces have been demonstrated. Finally, acoustic and thermal methods can be used to cause fluid disturbances as well[17]. Many mixers also function as miniature reactors, speeding up on-

chip chemical reactions. These reactors often have integrated temperature sensing and heaters to accurately control the reactor conditions[18].

Many separation techniques are also available to process a sample prior to detection. Separation is important in that it helps to reduce dependence on the sensor to be able to distinguish between different analytes in the fluid. Many separation technologies also have the net effect of concentration, as a particular molecule is more highly concentrated in the separated band than it was in the original sample. Electrically driven separations are extremely well studied. Electrophoretic separation devices are based on the different migration speeds of charged molecules in a medium (such as a gel or fluid) under the influence of an electric field. Specific techniques include capillary electrophoresis (CE) and capillary zone electrophoresis (CZE). Liquid chromatography (LC), which uses pressure driven flow, separates molecules based on their interaction with a solid phase support and a liquid mobile phase. Hybrid devices, which combine LC and electrophoresis, have also been demonstrated and include specific techniques such as micellar electrokinetic chromatography (MEKC) and capillary electrochromatography (CEC)[16].

1.5. HPLC / Conclusion

All the devices previously mentioned can be integrated to form lab-on-a-chip system for applications ranging from genomics and proteomics, to biodetection. This thesis will focus on the development and integration of components for HPLC, which is one of the most widely used and powerful separation techniques available to scientists today. HPLC is based on the interaction between the analytes, a solid stationary phase,

and liquid mobile phase. By choosing the proper mobile phase and stationary phase chemistries, analytes can be separated based on hydrophobicity, size, charge, and many other properties.

A typical separation system includes three main components: 1) pumps to drive the mobile phase, 2) a column, which contains the stationary phase (usually in the form of beads with a specially treated surface), and 3) a detector. To begin a separation, sample is first injected onto the column using an injection valve. After the sample has been loaded, the pump is used to drive the mobile phase through the column. The various molecules in the sample are then separated based on their varying retention properties. As the components of the sample elute off the column, the detector measures their concentration. A plot of the detector signal versus time is called a chromatogram. The peak heights, widths, and retention times from the chromatogram can be used to quantify and identify particular analytes in a complicated mixture.

The separation column itself can come in a variety of different diameters and chemistries. Table 1-1 shows a few of the most common types of column sizes and the flow rates that are used with them. Preparatory scale columns are the largest and are usually only used for purification while the other columns are designed for quantitative separations. The trend in HPLC has been towards smaller diameter columns, lower flow rates, and smaller beads sizes. This decrease in scale has brought with it several advantages, including an improvement in resolution and sensitivity. Higher resolution is due the reduction in bead size. Higher sensitivity is attained because a particular analyte is eluted in a smaller overall volume when smaller diameter columns/flow rates are used. As most detectors are concentration sensitive, this improves the overall system sensitivity.

The choice of column chemistry depends mainly on the type of sample being separated. Reverse-phase is the most common type of separation and uses a non-polar stationary phase generally consisting of silica beads bound with hydrophobic alkyl chains (e.g., C_4, C_8, or C_{18}). These stationary phases are used with a moderately polar mobile phase (such as water/acetonitrile mixtures) to separate molecules based on their hydrophobicity.

Column Type	Diameter	Flow Rate
Preparatory	> 5 mm	> 5 mL/min
Analytical	4–5 mm	1–10 mL/min
Narrowbore	2–4 mm	0.3–3 mL/min
Microbore	1–2 mm	50–1000 µL/min
Capillary	0.1–1 mm	0.4–200 µL/min
Nanobore	25–100 µm	25–4000 nL/min

Table 1-1: Typical column sizes for HPLC

Because the column is packed with small diameter beads, the pressure needed to drive the mobile phase is usually large, in most cases > 40 bar. While some HPLC analyses only require the use of a single mobile phase (e.g., isocratic elution), more advanced separation techniques require a mobile phase with a time-varying composition (e.g., gradient elution). In these more advanced separations, the mobile phase is normally composed of two different components, with the ratio of the two components varied over time. In effect, this requires two pumps, one for each component of the binary solvent system. As mentioned earlier, in the case of reverse-phase separations, a typical binary solvent system might consist of water/acetonitrile. Figure 1-6 shows a diagram of a typical binary HPLC system as well as a picture and diagram of an actual HPLC pump.

The advantage of a gradient elution becomes apparent when the sample contains analytes with widely varying retention properties. For an isocratic elution, the eluent composition must be chosen such that it is capable of eluting the most highly retained

analytes. Unfortunately, doing so can result in poor separation of the less strongly retained analytes. A gradient elution solves this problem by slowly increasing the elution strength of the mobile phase over time. One additional factor that must be taken into account when working with gradient elutions is column equilibration. After the gradient is complete, the column must be equilibrated with a low elution strength mobile phase before starting the next separation. Figure 1-7 shows the effect of a gradient elution on a separation.

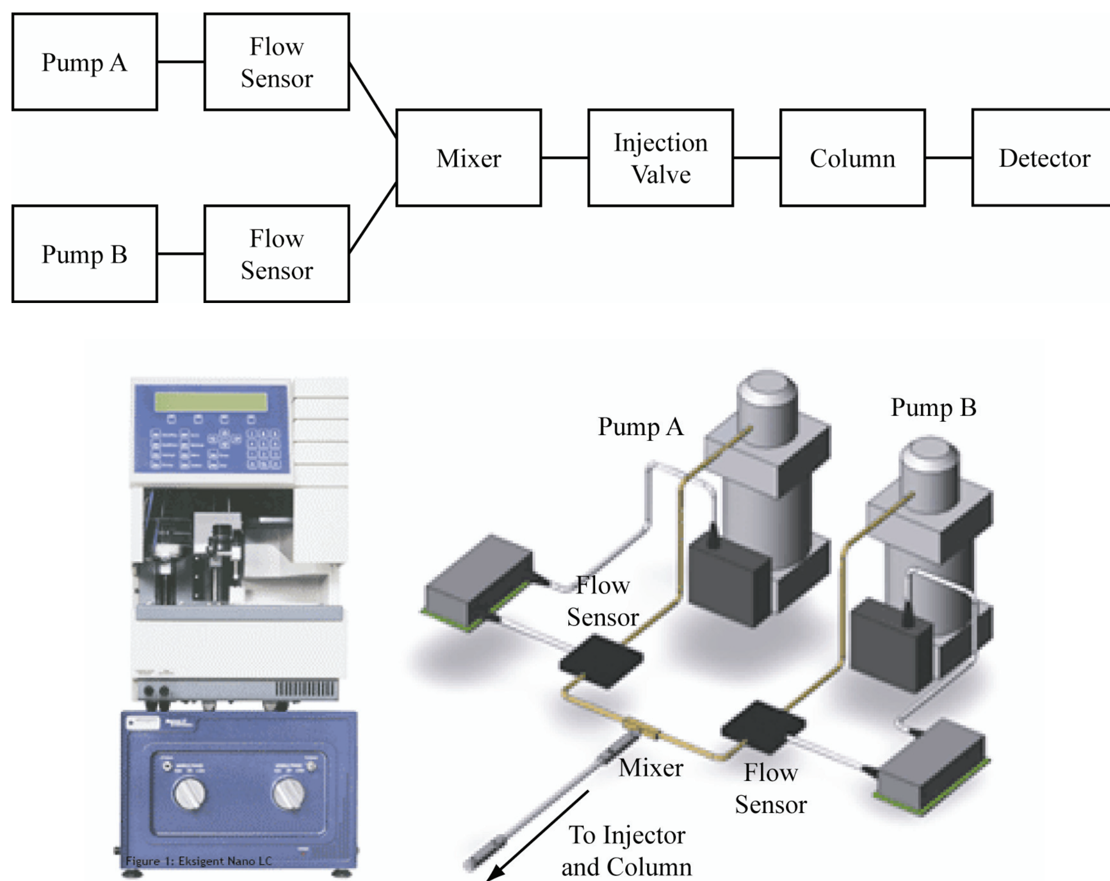

Figure 1-6: Diagram of a basic binary HPLC system. Shown on the bottom is an actual Eksigent NanoLC system with diagram of its internal components.

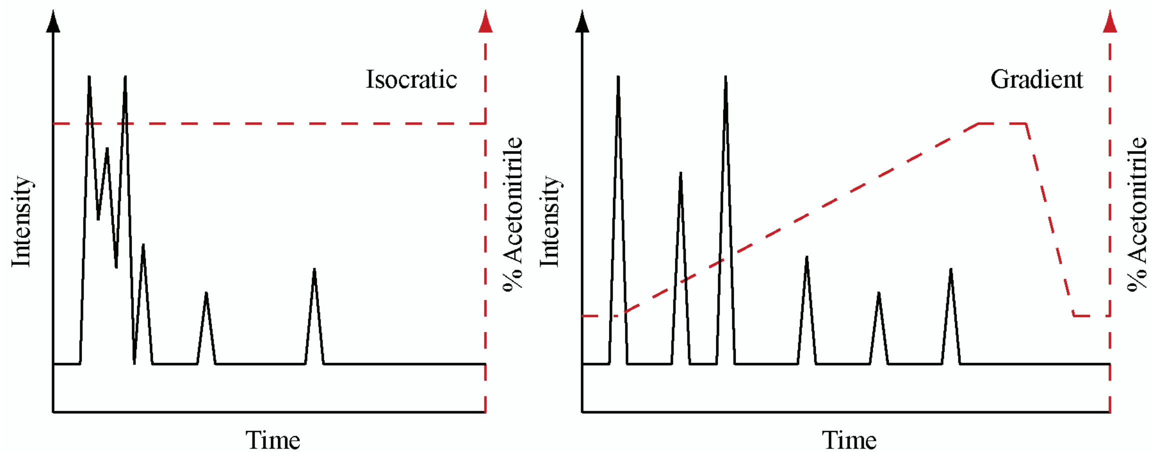

Figure 1-7: Comparison between isocratic and gradient elutions

Several detection methods exist. UV detectors are the most widely used because of their high sensitivity and near-universal detection capability. The detectors work by measuring the UV absorbance of the liquid/analytes in a flow cell connected to the end of the column. At the smaller chromatography scales, such nanoscale HPLC, UV absorbance is not used as frequently. This is mainly because UV detection needs a relatively long optical path length to achieve sensitive detection. The ability to do this, and still maintain good temporal resolution is diminished when the flow rates are very low. Instead of UV absorbance, mass spectrometry (MS) is often the preferred choice for nanoscale separations. Mass spectrometers are particularly desired because they essentially add another degree of separation (e.g., by mass). This not only decreases the dependence on the HPLC system, but also allows the analysis of more complex samples. MS also allows for methods of actually identifying the separated analytes based on their M/Z ratio rather than by their retention time. Coupling between the column and the mass spectrometer can be accomplished through on-line methods such as electrospray

ionization (ESI) or through spotting on a plate for analysis later using matrix-assisted laser desorption/ionization (MALDI).

As mentioned before, the progression of HPLC over the years has been towards smaller diameter columns and flow rates. In fact, it is not uncommon to see columns with an ID of < 50 µm and flow rates < 200 nL/min being used. These reductions in scale have lead to higher-resolution and higher-sensitivity separations, which has helped drive proteomics and other applications where complex mixtures of molecules need to be analyzed. Nanoscale HPLC has decreased to the point where microfluidic technologies can readily achieve the requisite dimensions and flow rates. There are several advantages of using microfluidics to implement a miniature HPLC system. First of all, a microfluidic system could provide a low-cost alternative to highly expensive conventional HPLC systems. A highly integrated microfluidic system could also be potentially easier to use, eliminating the need for highly trained personnel to conduct the separations. Finally, the small physical size of microfluidic systems allows for the creation of portable HPLC systems for point-of-care applications. The rest of this thesis will describe in detail the development of HPLC-compatible components (e.g., pumps, sensors, columns, filters), and the integration of these components to form a totally miniaturized separation system.

Chapter 2: Parylene Surface Micromachining Technology

2.1. Introduction

The fabrication technology used to create the microfluidic devices and systems in the following chapters is based around Parylene, a thin-film, chemically inert, and biocompatible polymer deposited using a room temperature chemical vapor deposition (CVD) process. Surface micromachining, a common technique in microfabrication, is used to build up the fluidic structures one Parylene layer at a time.

This chapter will begin by discussing Parylene, its material properties, and its application to microfluidics. The processing methods are best explained through the use of examples, and several illustrative processes will be described in detail. Common problems and solutions will also be discussed. Finally, the advantages of this technology will be examined. Overall, this chapter will give a detailed look at the Parylene surface micromachining process. The subsequent chapters will only describe fabrication in brief terms and this chapter should be referred to for detailed methodologies and underlying fabrication principles.

2.1.1. Parylene Background

Parylene is a transparent, inert, biocompatible, low permeability, and high-strength thin-film polymer that is conformally deposited using a room temperature CVD

process. The deposition thickness can range anywhere from < 0.1 µm to > 1000 µm. Parylene's unique room temperature conformal deposition process and material properties have made it widely used as an protective coating for products ranging from electronic components to medical devices such as catheters and pacemakers. Not surprisingly, Parylene has found applications in microfluidics. The same properties that make Parylene an ideal material for encapsulation make it promising for microfluidics use.

Parylene was first produced in 1947 by Professor Michael Mojzesz Szwarc at the University of Manchester in England. He discovered that the pyrolysis of para-xlene lead to the deposition of a unique film downstream in cooler temperature zones. He noted the unique chemical and mechanical properties of the film and named the material Szwarcite, which we now know as poly-p-xylylene or Parylene N. His discovery prompted further research at Union Carbide. It was here that William Franklin Gorham pioneered the process of using a stable dimer, di-p-xylylene, to produce poly-p-xylylene. But it wasn't until Donald Cram developed a way to synthesize di-p-xylylene at UCLA in 1951 that commercialization become possible. In all, Union Carbide developed over 20 types of Parylene, though today only Parylene C, N, and D are commonly used. More recently the commercialization of Parylene HT has added another dimer to that list.

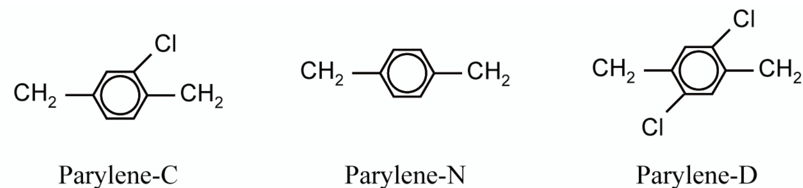

Figure 2-1: Chemical structure of common Parylene monomers

The three commonly used Parylenes (C, D, and N) each have their own unique properties. Their chemical structures are shown in Figure 2-1. Parylene C is generally considered the best choice for microfluidic applications. It exhibits the lowest gas and moisture permeability and also the highest mechanical strength of all the common Parylenes. In addition it has the highest deposition rate, generally around 2–3 µm/hr. Parylene C is also United States Pharmacopeia (USP) Class VI and ISO 10993 certified, meeting the most stringent tests of biocompatibility. Optically, Parylene C is transparent above 300 nm and throughout the visible range. Finally, Parylene C is also an excellent dielectric. Some important properties of Parylene C are listed in Table 2-1[19].

Property	Value
Density	1.289 g/cm^3
Young's Modulus	400000 psi
Tensile Strength	100000 psi
Melting Point	290 ºC
Thermal Conductivity	0.084 W/m-K
Dielectric Constant	3.1 (1 kHz)
Breakdown Voltage	220 V/µm
Water Vapor Permeability	0.08 g-mm/m^2-day

Table 2-1: Key properties of Parylene C

Note: Because Parylene C is used exclusively in the devices presented in this thesis, every Parylene reference, unless specified, should be assumed to refer to Parylene C.

2.1.2. Parylene Surface Micromachining with Photoresist as a Sacrificial Material

The Parylene-based microfluidic technology is based on surface micromachining, which uses alternating layers of a structural material and sacrificial material to build up structures one layer at a time[5]. Removal of the sacrificial material at the end of the process leaves only the desired 3-D freestanding structures. More specifically, this

technology is based around photoresist as the sacrificial material and Parylene as the structural material.

One simple example that illustrates the basic fabrication principles is a microchannel. The process begins with the deposition of a Parylene film on any substrate, such as a silicon wafer. A sacrificial photoresist layer is then deposited using a spin-on process, and patterned using photolithography. A second Parylene film is then coated to encapsulate the sacrificial photoresist. The ends of the channels are then etched open using an oxygen plasma with photoresist or metal as a mask. Finally the sacrificial photoresist is removed using a suitable solvent such as acetone or methanol. This example is described in more detail in example 1 of the experimental section and diagrammed in Figure 2-3.

While a single microchannel only uses two Parylene layers and one sacrificial photoresist layer, the basic concept can be generalized to use many more layers. Selective patterning of these Parylene layers prior to additional sacrificial photoresist layers can provide pathways for out-of-plane flow, opening the doors to devices such as valves. The addition of new layers is not necessarily limited to Parylene and photoresist. Polymers, such as epoxies and silicones, and metal layers can be used to add even more functionality. In addition to the central surface micromachining technology, techniques have also been developed to address the actual implementation and testing of the Parylene microfluidics. This includes the development of fluidic input/output (I/O) ports, which in combination with fluidic manifolds can be used to introduce and collect fluid from our devices. Also, modifications to the core technology have been developed to address special applications, such as high-performance liquid chromatography (HPLC).

These supporting technologies along with the core surface micromachining technology are described in the experimental section.

2.2. Experimental

This section will begin by giving an introduction to basic Parylene processing techniques such as deposition, patterning, and surface property control. Next, several detailed protocols will be presented.

1. **Example 1—Single Microchannel Fabrication**: This will cover the fabrication of the most basic structure in Parylene microfluidics.
2. **Example 2—Valve Fabrication**: This process details the fabrication of an electrostatically actuated valve. This example highlights the importance of proper surface treatments between different surfaces.
3. **Example 3—High-Pressure Microfluidics**: This example describes the fabrication of a Parylene channel capable of sustaining much higher pressures than the channel in Example 1.
4. **Example 4—SU-8 Fluidic I/O Ports**: The final section describes the making of "fluidic ports" along with the fluidic manifold needed to input/collect liquid to/from the microfluidic devices.

2.2.1. Materials

The list of materials is comprised of raw materials and equipment normally used in the fabrication of Parylene surface micromachined devices at the Caltech

Micromachining Laboratory, where all the devices in this thesis were fabricated. Specific model numbers are provided where applicable and available.

Processing Materials

- Silicon Wafers—Silicon Quest International
- Acetone, Isopropyl Alcohol, Concentrated H_2O_2, Concentrated H_2SO_4—VWR Scientific
- Concentrated HF—Transene, Inc.
- Cr-7 Chrome Etchant, Au Etchant—Cyantek
- Cr, Au, Ti, Pt Pellets—Williams Advanced Materials
- A-174 Adhesion Promoter, Parylene C Dimer—Specialty Coating Systems
- AZ4620, AZ1518 Photoresists—AZ Electronic Materials
- SU-8, LOR3B Photoresists—Microchem

Processing Equipment

- Oxidation Furnace (Thermco)—Tetreon
- Plasma Chamber (PEII-A)—Technics Plasma
- DRIE (SLR Series)—Plasma-Therm
- Parylene Deposition Chamber (PDS 2010)—Specialty Coating Systems
- Spin Dryer (Model 914)—Applied Process Technology
- Photoresist Spinner (Model PWM32)—Headway Research, Inc.
- Photoresist Baking Oven (LAC Series)—Despatch
- Photoresist Baking Digital Hot Plate—Cole-Parmer

- Stepper (4800 DSW)—GCA Mann
- Contact Aligner—Kasper Instruments
- E-Beam Evaporator—CHA Industries

Fluidic Manifold Manufacturing

- Computer Numerical Controlled (CNC) Mill—Sherline Products, Inc.
- Plastics (PEEK, PEI, Teflon), Tooling (Machining Tools, Hardware)—McMaster Carr
- O-Rings—Apple Rubber Products, Inc.
- Fittings/Tubing—Upchurch Scientific

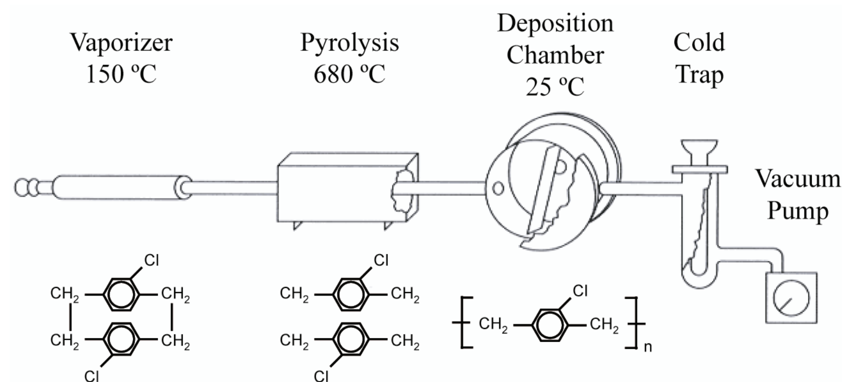

Figure 2-2: Diagram showing the Parylene deposition process

2.2.2. Parylene Processing

2.2.2.1. Deposition

Parylene is deposited using a room temperature CVD process. The deposition process begins with the vaporization of the Parylene dimer (~ 150 °C). Each individual dimer is then pyrolized (~ 680 °C) and broken down into two individual monomers. The gas-phase monomers then deposit as a polymer film downstream in a deposition chamber

at ambient temperature. The entire process is conducted in a medium vacuum (5–10 mTorr). The overall deposition process is illustrated in Figure 2-2. The deposition rate is controlled by regulating the partial pressure of the Parylene monomer in the deposition chamber. The reading from a pressure sensor in the deposition chamber is used as feedback to control the vaporizer temperature in order to maintain a constant pressure. In general, the partial pressure of the monomer is set to be approximately 15 mTorr, which roughly translates to a deposition rate of 2–3 μm/hr. The total deposition thickness is determined by the initial amount of Parylene dimer placed in the vaporizer. The exact relationship between Parylene thickness and dimer amount will depend on the exact machine and load[19].

2.2.2.2. Patterning

Because Parylene is chemically inert to nearly all liquids, it cannot be effectively etched using a wet process. Only a few solvents, such as chloro-napthalene are known to dissolve Parylene, and this is only at a temperature of 175 °C. The preferred method of Parylene patterning is oxygen plasma etching. The etching rate depends on many factors, the most important being the type of plasma etcher, the power, and the oxygen pressure. In general the etch rate will vary from 0–0.5 μm/min depending on the plasma conditions. The most convenient material to use as a mask for Parylene etching is photoresist, as it can be patterned to the correct thickness and has excellent adhesion to the Parylene. Photoresist etches at nearly the same rate as Parylene in an oxygen plasma[20]. In general, the photoresist mask needs to be at least twice the thickness of the Parylene to be etched. For thick Parylene layers (> 10 μm), metal etch masks are normally used. Metals such as

Al and Au as thin as 2000 Å are sufficient to etch more than 30 μm of Parylene. These metals, as long as they aren't sputtered, have a nearly infinite etch ratio when compared to Parylene. One advantage of using a metal etch mask is that it can be removed (via wet etching) without disturbing any sacrificial photoresist that might have been revealed during the Parylene etching. Stripping a photoresist etch mask, on the other hand, will inevitably remove some of the exposed sacrificial photoresist as well.

All the Parylene etching processes described in the experimental section are based on the use of a PEII-A parallel plate plasma etcher. Etch rates of ~ 0.15–0.2 μm/min are generally observed. Etching is load dependant, which can cause some variation in the etch rate.

2.2.2.3. Surface Treatment and Adhesion

As deposited, Parylene exhibits a water contact angle of approximately 75°. An oxygen plasma treatment can make the surface extremely hydrophilic, reducing the water contact angle to < 5°. An SF_6 plasma treatment, on the other hand, can increase the contact angle to > 105°. The Parylene surface can be partially restored to its natural, as-deposited state by treating the surface with a dilute HF solution. These different surface treatments play a large role in the adhesion between different layers.

Because Parylene is generally the first layer deposited on the substrate and needs to withstand all subsequent processing steps, good adhesion between Parylene and the substrate is critical. Parylene exhibits poor adhesion to a hydrophilic surface such as silicon oxide. On the other hand, Parylene naturally adheres well to clean hydrophobic surfaces. To attain good adhesion between Parylene and hydrophilic surfaces, an

adhesion promoter such as A-174 (gamma-methacryloxy propyltrimethoxysilane) is generally used. In some cases, neglecting to use A-174 and directly depositing Parylene on a hydrophilic surface will cause the Parylene layer to delaminate even in the presence of a neutral solvent such as water. One limitation of the A-174 adhesion promoter is that the organic solvent used to dissolve the A-174 will also dissolve any exposed photoresist on the wafer. Because of this, it is often desirable to deposit a thin Parylene layer (after application of A-174) prior to using any sacrificial photoresist layers. This eliminates the need for adhesion promoter later in the process.

The most common interface encountered in device fabrication is that between Parylene layers. The optimal surface treatment consists of an oxygen plasma cleaning/roughening process followed by a rinse in a dilute HF solution. The plasma roughening is believed to provide a pitted surface for the second Parylene layer to cling onto and the dilute HF is thought to clean the Parylene surface and restore its natural hydrophobicity.

Adhesion between photoresist and Parylene is generally good and no surface treatment is necessary. The hydrophobic nature of both photoresist and Parylene provides for naturally good adhesion. A short bake in the oven to remove any water on the Parylene surface is usually performed.

Metal/Parylene interfaces are often encountered. The use of adhesion layers such as Cr and Ti is often helpful to improve adhesion, particularly with Au, which demonstrates very poor adhesion to Parylene. Other commonly used metals such as Al and Pt do not need any adhesion layer. An oxygen plasma surface cleaning prior to metal deposition can be performed to remove unwanted organic contaminants.

2.2.3. Detailed Processing Examples

2.2.3.1. Example 1—Single Microchannel Fabrication

For the purposes of this example, the fabrication of a single microchannel (1 cm x 100 µm x 10 µm—LxWxH) on a 500-µm-thick silicon wafer will be described. The walls of the microchannel will be 5-µm-thick Parylene. A diagram of the process is shown in Figure 2-3.

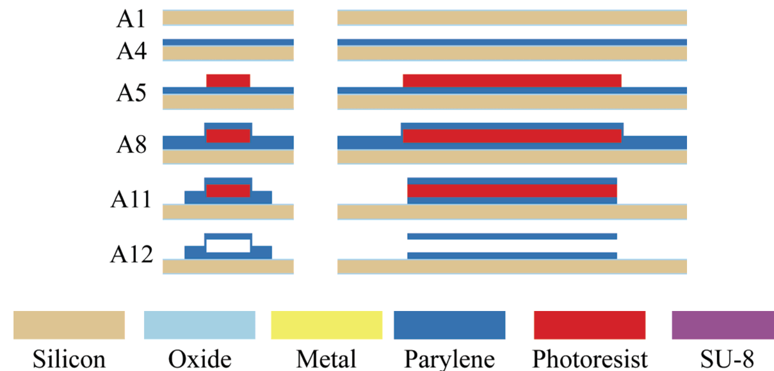

Figure 2-3: Process flow for single microchannel fabrication

A1. Grow 5000 Å silicon oxide on wafer using wet thermal oxidation. Example: Temperature: 1050 °C, Duration: 1 hr

A2. Surface cleaning/treatment using oxygen plasma. Example: Power: 200 W, Pressure: 200 mTorr O_2, Duration: 2 min

A3. Apply A-174 adhesion promoter. Example: Prepare 100:100:1 (by volume) solution of IPA:DI water:A-174. Stir and let stand for at least 2 hr. Submerge wafer in A-174 solution for 15 min. Air dry for 15 min. Rinse with IPA for 15 s. Air dry for 30 s.

A4. Deposit 5 µm Parylene. Example: Parylene Dimer Amount: 7.5 g, Vaporizer SP: 180 ºC, Pyrolysis SP: 690 ºC, Pressure SP: 23 mTorr

A5. Spin and pattern 10 µm photoresist layer. Example: Surface Dehydration: 15 min at 100 °C (oven), Photoresist: AZ4620, Spin Speed: 1400 RPM, Soft Bake: 30 min at 100 °C (oven), Exposure: 700 mJ/cm^2 g-Line, Development: 1.5 min in AZ351:DI Water (1:3), Post Bake: 2 hr at 120 °C (oven)

A6. Surface cleaning/roughening using oxygen plasma. Example: Power: 400 W, Pressure: 200 mTorr O_2, Duration: 1 min

A7. Surface cleaning/treatment using 5% HF dip followed by DI water rinse. Example: HF Dip Duration: 5 sec

A8. Deposit 5 µm Parylene. Example: Parylene Dimer Amount: 7.5 g, Vaporizer SP: 180 ºC, Pyrolysis SP: 690 ºC, Pressure SP: 23 mTorr

A9. Spin and pattern ~ 45–50 µm photoresist. Example: Surface Dehydration: 15 min at 100 °C (oven), Photoresist: AZ4620, Spin Speed: 500 RPM, Soft Bake: 5 min at 100 °C, cool to room temperature at 2 °C/min (hot plate), Exposure: 1500 mJ/cm^2 g-Line, Development: 5 min in AZ351:DI Water (1:3), Post Bake: 15 min at 100 °C (oven)

A10. Parylene etching using oxygen plasma. Example: Power: 400 W, Pressure: 200 mTorr O_2, Duration: 80 min

A11. Strip photoresist etch mask using acetone/IPA followed by DI water rinse.

A12. Dissolve sacrificial photoresist in acetone. Example: Temperature: 25 ºC, Duration: 2 days

A long post bake is necessary after patterning the sacrificial photoresist layer (step A5). The reasoning behind this is that all liquids (e.g., solvent) need to be baked out of the photoresist prior to encapsulation with Parylene. Not doing so can cause outgassing during later high-temperature processes, such as during the Parylene plasma etch, and cause the fully encapsulated channel to rupture.

Even though in this example only 20 μm of Parylene/photoresist needs to be etched (e.g., 5 μm Parylene + 10 μm photoresist + 5 μm Parylene), a photoresist mask greater than 40 μm is used (A9). This is to ensure there is enough photoresist to account for non-uniformity in the photoresist mask thickness, particularly near the channel structures where the photoresist is not conformally coated.

This example encounters Parylene/substrate and Parylene/Parylene interfaces. As outlined earlier, Parylene/substrate adhesion, when the substrate is hydrophilic, is best when using an adhesion promoter (A2–A3), and Parylene/Parylene adhesion is optimized by using a combination of oxygen plasma cleaning/roughening and HF surface cleaning/treatment (A6–A7). Also, the initial Parylene layer, while not necessary to create the channel structure, is used to ensure that no more Parylene/substrate interfaces are encountered later in the process. This is done to prevent the need to apply A-174 adhesion promoter mid-process, which would dissolve the sacrificial photoresist layer.

2.2.3.2. Example 2—Valve Fabrication

The method of making a microchannel can be expanded to create more complicated microfluidic devices. For example, after step A11, instead of dissolving the photoresist, another sacrificial photoresist layer can be added, followed by another

Parylene layer, and so on. To illustrate this, the fabrication of an in-channel electrostatic valve[21] will be described. The valve uses a circular composite (Parylene/metal/Parylene) diaphragm with an etched hole in the center. Applying a high voltage to the diaphragm electrode while grounding an electrode underneath the membrane will cause the diaphragm to collapse, sealing the hole, and shutting off flow. In all, there are two metal layers, two sacrificial photoresist layers, and four Parylene layers. The process is diagramed in Figure 2-4.

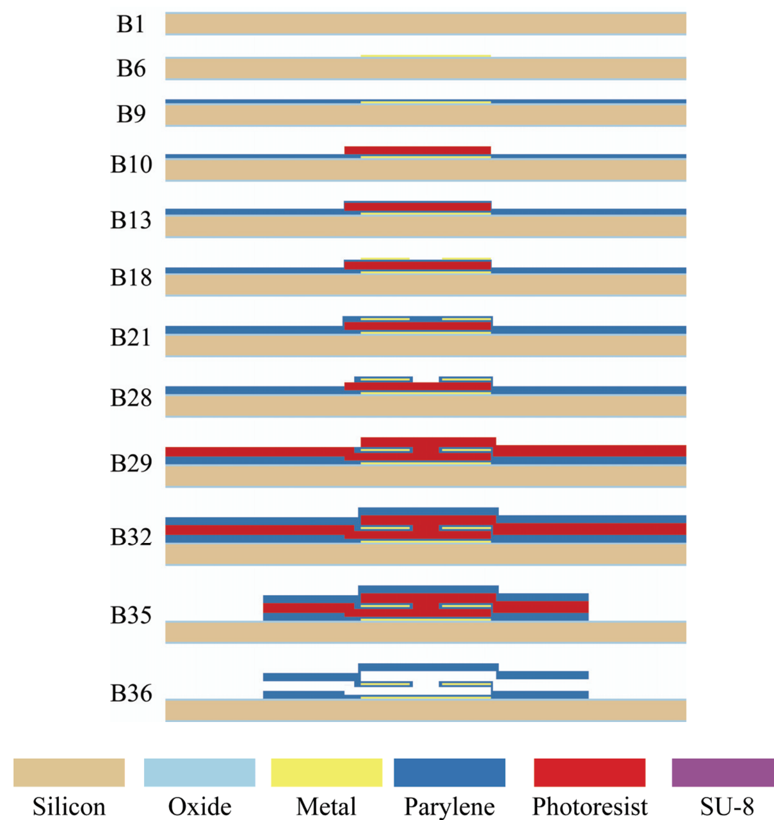

Figure 2-4: Process flow for valve fabrication

B1. Grow 5000 Å silicon oxide on wafer using wet thermal oxidation. Example: Temperature: 1050 °C, Duration: 1 hr

B2. Surface cleaning/treatment using oxygen plasma. Example: Power: 200 W, Pressure: 200 mTorr O_2, Duration: 2 min

B3. Deposit Cr/Au metal layer using evaporator. Example: Cr Thickness: 200 Å, Au Thickness: 2000 Å

B4. Spin and pattern 10 µm photoresist layer. Example: Surface Dehydration: 15 min at 100 °C (oven), HMDS Vapor Prime: 2 min, Photoresist: AZ4620, Spin Speed: 1400 RPM, Soft Bake: 30 min at 100 °C (oven), Exposure: 700 mJ/cm^2 g-Line, Development: 1.5 min in AZ351:DI Water (1:3), Post Bake: 15 min at 100 °C (oven)

B5. Etch Cr/Au metal layer using Au (Type TFA) etchant and Cr (CR-7) etchant. Example: Au Etching Duration: 50 sec, Cr Etching Duration: 10 sec

B6. Strip photoresist etch mask using acetone/IPA followed by DI water rinse.

B7. Surface cleaning/treatment using oxygen plasma. Example: Power: 200 W, Pressure: 200 mTorr O_2, Duration: 2 min

B8. Apply A-174 adhesion promoter. Example: Prepare 100:100:1 (by volume) solution of IPA:DI water:A-174. Stir and let stand for at least 2 hr. Submerge wafer in A-174 solution for 15 min. Air dry for 15 min. Rinse with IPA for 15 s. Air dry for 30 s.

B9. Deposit 1 µm Parylene. Example: Parylene Dimer Amount: 1.5 g, Vaporizer SP: 180 ºC, Pyrolysis SP: 690 ºC, Pressure SP: 23 mTorr

B10. Spin and pattern 5 µm photoresist layer. Example: Surface Dehydration: 15 min at 100 °C (oven), Photoresist: AZ4620, Spin Speed: 2500 RPM, Soft

Bake: 30 min at 100 °C (oven), Exposure: 250 mJ/cm^2 g-Line, Development: 1.5 min in AZ351:DI Water (1:3), Post Bake: 2 hr at 120 °C (oven)

B11. Surface cleaning/roughening using oxygen plasma. Example: Power: 400 W, Pressure: 200 mTorr O_2, Duration: 1 min

B12. Surface cleaning/treatment using 5% HF dip followed by DI water rinse. Example: HF Dip Duration: 5 sec

B13. Deposit 1 µm Parylene. Example: Parylene Dimer Amount: 1.5 g, Vaporizer SP: 180 ºC, Pyrolysis SP: 690 ºC, Pressure SP: 23 mTorr

B14. Surface cleaning/treatment using oxygen plasma. Example: Power: 200 W, Pressure: 200 mTorr O_2, Duration: 2 min

B15. Deposit Cr/Au metal layer using evaporator. Example: Cr Thickness: 200 Å, Au Thickness: 2000 Å

B16. Spin and pattern 10 µm photoresist layer. Example: Surface Dehydration: 15 min at 100 °C (oven), HMDS Vapor Prime: 1 min, Photoresist: AZ4620, Spin Speed: 1400 RPM, Soft Bake: 30 min at 100 °C (oven), Exposure: 700 mJ/cm^2 g-Line, Development: 1.5 min in AZ351:DI Water (1:3), Post Bake: 15 min at 100 °C (oven)

B17. Etch Cr/Au metal layer using Au (Type TFA) etchant and Cr (CR-7) etchant. Example: Au Etching Duration: 50 sec, Cr Etching Duration: 10 sec

B18. Strip photoresist etch mask using acetone/IPA followed by DI water rinse.

B19. Surface cleaning/roughening using oxygen plasma. Example: Power: 400 W, Pressure: 200 mTorr O_2, Duration: 1 min

B20. Surface cleaning/treatment using 5% HF dip followed by DI water rinse. Example: HF Dip Duration: 5 sec

B21. Deposit 1 µm Parylene. Example: Parylene Dimer Amount: 1.5 g, Vaporizer SP: 180 ºC, Pyrolysis SP: 690 ºC, Pressure SP: 23 mTorr

B22. Surface cleaning/treatment using oxygen plasma. Example: Power: 200 W, Pressure: 200 mTorr O_2, Duration: 2 min

B23. Deposit Cr/Au metal layer using evaporator. Example: Cr Thickness: 200 Å, Au Thickness: 2000 Å

B24. Spin and pattern 10 µm photoresist layer. Example: Surface Dehydration: 15 min at 100 °C (oven), HMDS Vapor Prime: 1 min, Photoresist: AZ4620, Spin Speed: 1400 RPM, Soft Bake: 30 min at 100 °C (oven), Exposure: 700 mJ/cm^2 g-Line, Development: 1.5 min in AZ351:DI Water (1:3), Post Bake: 15 min at 100 °C (oven)

B25. Etch Cr/Au metal layer using Au (Type TFA) etchant and Cr (CR-7) etchant. Example: Au Etching Duration: 50 sec, Cr Etching Duration: 10 sec

B26. Strip photoresist etch mask using acetone/IPA followed by DI water rinse.

B27. Parylene etching using oxygen plasma. Example: Power: 400 W, Pressure: 200 mTorr O_2, Duration: 8 min

B28. Strip Cr/Au etch mask using Au (Type TFA) etchant and Cr (CR-7) etchant followed by DI water rinse.

B29. Spin and pattern 5 µm photoresist layer. Example: Photoresist: Surface Dehydration: 15 min at 100 °C (oven), AZ4620, Spin Speed: 1400 RPM, Soft

Bake: 30 min at 100 °C (oven), Exposure: 700 mJ/cm^2 g-Line, Development: 1.5 min in AZ351:DI Water (1:3), Post Bake: 2 hr at 120 °C (oven)

B30. Surface cleaning/roughening using oxygen plasma. Example: Power: 400 W, Pressure: 200 mTorr O_2, Duration: 1 min

B31. Surface cleaning/treatment using 5% HF dip followed by DI water rinse. Example: HF Dip Duration: 5 sec

B32. Deposit 5 μm Parylene. Example: Parylene Dimer Amount: 7.5 g, Vaporizer SP: 180 ºC, Pyrolysis SP: 690 ºC, Pressure SP: 23 mTorr

B33. Spin and pattern ~ 45–50 μm photoresist. Example: Surface Dehydration: 15 min at 100 °C (oven), Photoresist: AZ4620, Spin Speed: 500 RPM, Soft Bake: 5 min at 100 °C, cool to room temperature at 2 °C/min (hot plate), Exposure: 1500 mJ/cm^2 g-Line, Development: 5 min in AZ351:DI Water (1:3), Post Bake: 15 min at 100 °C (oven)

B34. Parylene etching using oxygen plasma. Example: Power: 400 W, Pressure: 200 mTorr O_2, Duration: 75 min

B35. Strip photoresist etch mask using acetone/IPA followed by DI water rinse.

B36. Dissolve sacrificial photoresist in acetone. Example: Temperature: 25 ºC, Duration: 2 days

As for the microchannel process (example 1), a long post bake is used for any photoresist layer that will be encapsulated by Parylene (B10, B29). Also, a very thick photoresist etch mask (B33) is used to make sure there is sufficient photoresist coverage over the entire topology of the device.

A Cr/Au metal layer instead of photoresist is used as an etch mask for the patterning of the central hole in the valve membrane (B22–B28). This is because the first sacrificial photoresist layer is revealed during the Parylene etching. If a photoresist etch mask had been used, the removal of the etch mask with acetone/IPA would have removed some of the revealed sacrificial photoresist layer. Using Cr/Au as an etch mask solves this problem because the etchants used to remove the metals do not have any effect on the revealed photoresist.

There is a clear repetition of steps as each surface is treated before adding a new layer. Once again, an adhesion promoter (B7–B8) is applied before depositing the first Parylene layer on the substrate. Also, the combination of oxygen plasma and HF treatment (B11–B12, B19–B20, B30–B31) is used on every Parylene/Parylene interface. This structure also has metal/Parylene interfaces, which were not present in the microchannel example. To ensure there is good adhesion, a combination of oxygen plasma treatment and Cr adhesion layer is used (B14–B15, B22–B23).

2.2.3.3. Example 3—High-Pressure Microfluidics

One of the limitations of the surface micromachined channels described to this point is the complete reliance on Parylene to Parylene adhesion. While suitable for low pressure applications (< 2 bar) the channels will rupture at higher pressures. To address this, an anchoring technology, which allows the fabrication of fluidic structures capable of withstanding > 100 bar, has been developed. This technology utilizes mushroom-shaped trenches etched into the wafer surface along the sides of the microchannel pathway. The trenches are etched using a two-step deep reactive ion etching (DRIE)

process. The first step consists of a standard Bosch process and produces vertical trenches. The second step is an isotropic SF_6 etch to produce a mushroom shaped bulb at the bottom of the trench. Because of the highly conformal nature of Parylene deposition, this trench will be completely filled with Parylene providing a mechanical mechanism for securing the Parylene layer to the substrate[22].

The processing steps for the fabrication of a single microchannel (1 cm x 100 µm x 10 µm—LxWxH) on a 500-µm-thick silicon wafer are listed below. The top and side walls of the channel will be 10 µm Parylene while the bottom of the channel will be a silicon oxide surface. The process is diagrammed in Figure 2-5.

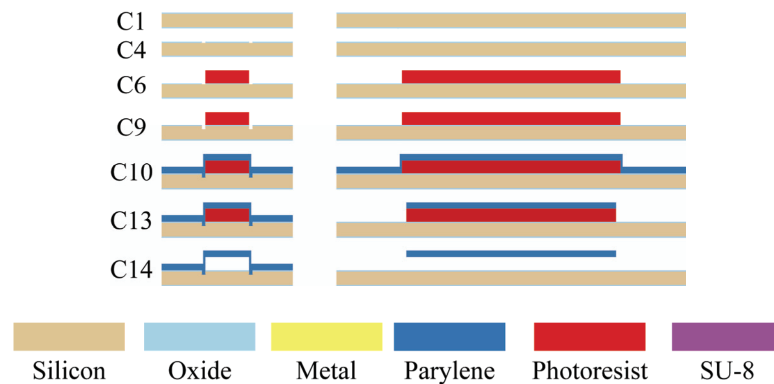

Figure 2-5: Process flow for high-pressure-capable microchannel

C1. Grow 5000 Å silicon oxide on wafer using wet thermal oxidation. Example: Temperature: 1050 °C, Duration: 1 hr

C2. Spin and pattern 2 µm photoresist layer. Example: Surface Dehydration: 15 min at 100 °C (oven), HMDS Vapor Prime: 2 min, Photoresist: AZ1518, Spin Speed: 4000 RPM, Soft Bake: 30 min at 100 °C (oven), Exposure: 200 mJ/cm^2 g-Line, Development: 1.5 min in AZ351:DI Water (1:4), Post Bake: 15 min at 100 °C (oven)

C3. Etch silicon oxide using buffered HF. Example: Duration: 6 min

C4. Strip photoresist etch mask using acetone/IPA followed by DI water rinse.

C5. Surface cleaning/treatment using oxygen plasma. Example: Power: 200 W, Pressure: 200 mTorr O_2, Duration: 2 min

C6. Spin and pattern 10 μm photoresist layer. Example: Surface Dehydration: 15 min at 100 °C (oven), HMDS Vapor Prime: 2 min, Photoresist: AZ4620, Spin Speed: 1400 RPM, Soft Bake: 30 min at 100 °C (oven), Exposure: 700 mJ/cm^2 g-Line, Development: 1.5 min in AZ351:DI Water (1:3), Post Bake: 2 hr at 120 °C (oven)

C7. Surface cleaning using oxygen plasma. Example: Power: 200 W, Pressure: 200 mTorr O_2, Duration: 2 min

C8. Surface cleaning using 5% HF dip followed by DI water rinse. Example: HF Dip Duration: 5 sec

C9. Etch anchors using DRIE. Example: Etch 1 Recipe: Bosch process, Etch 1 Depth: 50 μm, Etch 2 Recipe: SF_6, Etch 2 Depth: 10 μm

C10. Deposit 10 μm Parylene. Example: Parylene Dimer Amount: 15 g, Vaporizer SP: 180 ºC, Pyrolysis SP: 690 ºC, Pressure SP: 23 mTorr

C11. Spin and pattern ~ 45–50 μm photoresist. Example: Surface Dehydration: 15 min at 100 °C (oven), Photoresist: AZ4620, Spin Speed: 500 RPM, Soft Bake: 5 min at 100 °C, cool to room temperature at 2 °C/min (hot plate), Exposure: 1500 mJ/cm^2 g-Line, Development: 5 min in AZ351:DI Water (1:3), Post Bake: 15 min at 100 °C (oven)

C12. Parylene etching using oxygen plasma. Example: Power: 400 W, Pressure: 200 mTorr O_2, Duration: 80 min

C13. Strip photoresist etch mask using acetone/IPA followed by DI water rinse.

C14. Dissolve sacrificial photoresist in acetone. Example: Temperature: 25 ºC, Duration: 2 days

The overall process is very similar to that of making a non-anchored microchannel (example 1). The long post bake of the sacrificial photoresist (C6) and a thick photoresist etch mask (C11) still apply.

Several design rules need to be considered when making the anchors. The width of the anchors needs to be less than twice the thickness of the Parylene layer it is anchoring. For example, to anchor a 10 µm Parylene layer to the substrate an anchor width of 10–15 µm is typical. In this process, the mask for etching the anchors is defined using oxide on one edge and the sacrificial photoresist on the other edge. The DRIE process will etch the sacrificial photoresist slightly (e.g., ~ 1:100 to 1:50 photoresist:silicon). This needs to be taken into account if accurate channel heights are desired.

No surface treatments are necessary prior to the Parylene deposition because the reliance is on mechanical anchoring of the Parylene to the substrate instead of chemical adhesion.

2.2.3.4. Example 4—SU-8 Fluidic Ports

The purely surface micromachined fluidic structures described so far provide no easy way to connect the channel to external pumps or sensors. One way to overcome this is to use SU-8, a photopatternable epoxy, to completely encapsulate the fluidic structures and create ports at the inlets and outlets. This is done by adding a single SU-8 layer just prior to photoresist dissolution. The SU-8 has the added advantage of strengthening the channels, allowing them to withstand higher pressures. The processing steps for adding SU-8-based ports to the microchannel described in example 1 are described below and diagrammed in Figure 2-6.

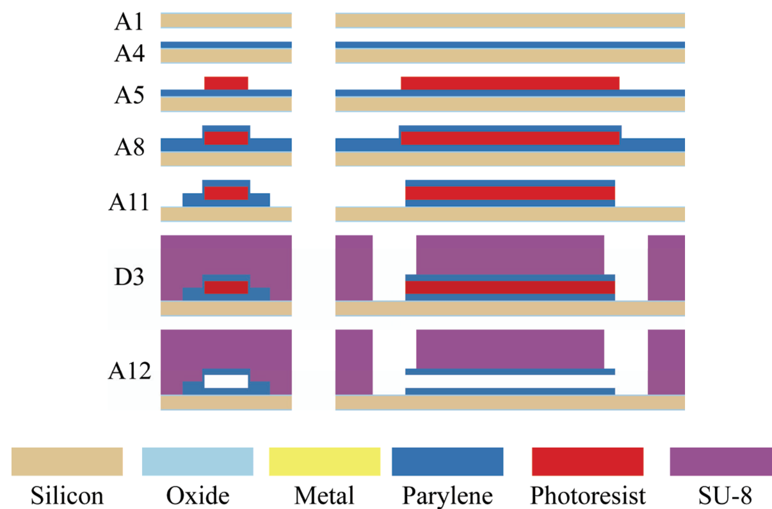

Figure 2-6: Process flow showing the creating of SU-8-based ports at the inlet/outlet of a microchannel

Start by performing steps A1–A11, then continuing as follows:

D1. Surface cleaning/treatment using oxygen plasma. Example: Power: 200 W, Pressure: 200 mTorr O_2, Duration: 2 min

D2. Surface cleaning using 5% HF dip followed by DI water rinse. Example: HF Dip Duration: 5 sec

D3. Spin and pattern 50 µm SU-8 layer. Example: Surface Dehydration: 15 min at 100 °C (oven), Photoresist: SU-8 50, Spin Speed: 2400 RPM, Soft Bake: 30 min at 80 °C, heat/cool from/to room temperature at 2 °C/min (hot plate), Exposure: 2000 mJ/cm^2 g-line, Post Exposure Bake: 10 min at 80 °C, heat/cool from/to room temperature at 2 °C/min (hot plate), Development: 4 min in SU-8 developer (PGMEA), Post Bake: 1 hr at 100 °C, heat/cool from/to room temperature at 2 °C/min (hot plate)

The process is finished by performing step A12.

Steps D1–D2 are cleaning steps to prepare the wafer surface for the SU-8 layer. Not cleaning the wafer surface will likely lead to delamination of the SU-8 from the wafer during photoresist dissolution. Delamination is caused by swelling of the SU-8 after long soaks in organic solvents such as acetone or IPA. To reduce swelling it is recommended to use higher exposure dosages and longer post bakes of the SU-8 layer than recommended in the manufacturer data sheets to ensure full cross linking and best possible chemical inertness. For example, the recipe above has an exposure dose 4x that of the one recommended by the manufacturer. With full cross linking, SU-8 can withstand even heated acetone solutions (40 ºC) for weeks without any cracking or delamination from the wafer surface. In some cases, using a DRIE process to etch anchors in the substrate prior to SU-8 coating can help improve the adhesion. In much the same way the anchors improved Parylene adhesion in example 3, they can also help prevent SU-8 delamination.

Instead of using photoresist as an etch mask (A9–A10), a metal mask can also be used. The advantage of using a metal etch mask is that it can be removed without dissolving any of the sacrificial photoresist in the channel that was revealed during the Parylene etch. If too much sacrificial photoresist is removed, the SU-8 can seep into the channels and potentially lead to blockages.

Once the fluidic ports are created on the chips, fluid connections can be made using a fluidic manifold. The manifold will have ports, which on one end will seal against the port on the chip and on the other end connects to the desired tubing. These manifolds are generally made out of high-performance, chemically inert plastics such as PEEK, PEI, and Teflon, using conventional machining methods.

The sealing between the manifold and the chip can be done using either gaskets or o-rings. With the proper high-pressure fitting and commercially available o-rings, the packaging scheme can withstand pressures > 100 bar. O-rings 0.5 x 0.5 mm (ID x cross-section diameter) or smaller are typically used.

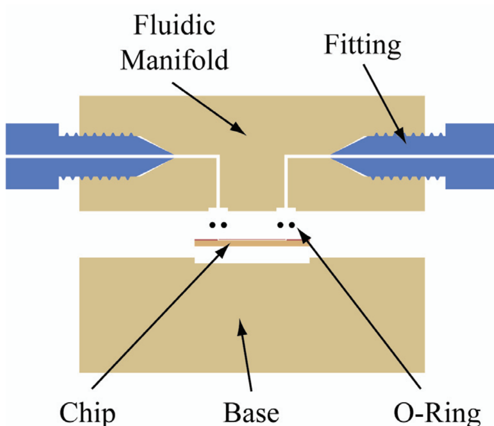

Figure 2-7: A diagram showing the fluidic packaging concept

Tubing to manifold connections can be made using a variety of different fittings. The most useful ones tend to be those designed for HPLC, which are made to a tight-

tolerance and with low volume and high pressure in mind. One example of a fluidic manifold can be seen in Figure 2-7. The diagrammed packaging scheme also has alignment grooves to hold the chip and o-rings. These grooves facilitate alignment of the manifold, o-rings, and chip.

2.2.4. Common Problems

2.2.4.1. Adhesion Issues

In nearly all cases, unsuccessful fabrication of Parylene-based microfluidic devices is caused by failure in adhesion between layers. Good adhesion can be consistently achieved with the use of proper surface treatment before the addition of each layer, whether it be metal, photoresist, or Parylene.

2.2.4.2. Heating Issues

Another common problem is the formation of bubbles in Parylene-encapsulated sacrificial photoresist. The formation of these bubbles will cause the channel to expand, eventually rupturing. This is most often seen during plasma etching steps where the substrate temperature is not completely regulated.

This problem can be avoided in two ways. First, do a lengthy post bake of any sacrificial photoresist layer after development to remove any residual solvents in the photoresist. And second, use low power plasma settings and/or divide the entire etch into shorter, and therefore cooler, etching cycles. As a general rule, any process done on the device should not exceed the photoresist baking temperatures.

2.2.4.3. Photoresist Dissolution

Another problematic step is the dissolution of the photoresist sacrificial layer. The photoresist dissolution process is limited by not only the solubility of the photoresist in the organic solvent used, but also how fast photoresist can diffuse out of the channels[23]. For devices where there is a very long channel length, photoresist dissolution can take a significant amount of time. It is important to wait until all the photoresist has dissolved and diffused out of the channel before drying the devices, otherwise the residual photoresist will remain in the channels and need to be dissolved again. Solvents such as IPA or methanol dissolve the photoresist at a similar rate, and for a 1-cm-long channel, require approximately one week until the photoresist is completely removed. Stronger solvents such as acetone are much faster, needing only a few days for the same-sized channels. Heating the solvent can also greatly increase the dissolution rate. While acetone is much faster, there can be a tendency for the acetone to attack interfaces, causing delamination. Acetone also has the tendency to swell some photoresist, such as SU-8. This swelling can cause cracks to form in the SU-8 and underlying Parylene. Because of this, the SU-8 processing parameters must be highly controlled. An optimized SU-8 process like the one described in example 4 is able to withstand Acetone for months without any noticeable effect.

One method that has been particularly effective in speeding up the photoresist dissolution process is to flush the channel with Acetone as soon as the photoresist has been dissolved all the way through. This eliminates the need to wait for the photoresist to diffuse out. Using this technique, microchannels as long as 5 cm have been fully released in less than 1 week.

2.2.4.4. Conformality

As with any surface-micromachining process, the conformality of the different layers plays a key role in attaining the desired device. Parylene naturally produces a conformal coating, but spun-on photoresist does not. This is particularly evident when the photoresist layer that is being added is thinner than the structures already on the wafer. It is important to check each photoresist layer after lithography to make sure it achieves the desired height.

2.3. Device Examples

Numerous devices have been demonstrated with this technology. A brief summary of them will be given here.

2.3.1. Sensors

A thermal flow sensor[21] was demonstrated and operated using a calorimetric principle. The temperature of a heater integrated into the channel was dependent on the channel flow rate, the higher the flow rate, the lower the temperature of the heater. With water, the flow sensor demonstrated good performance between 0–100 nL/min with a sensitivity of 0.8 nL/min. For air, the range was from 0–10 µL/min with a sensitivity of 0.2 µL/min. A picture and diagram of this device can be found in Figure 2-8.

A time-of-flight (TOF) flow sensor[24] (also see Chapter 3) was also fabricated and characterized. Flow rate measurements were based on detecting the traveling time of an electrochemically generated ion pulse over a fixed distance, giving a measure of the

linear flow velocity. The flow sensor was optimized for flow rates < 200 nL/min and demonstrated a sensitivity of 1.6 nL/min.

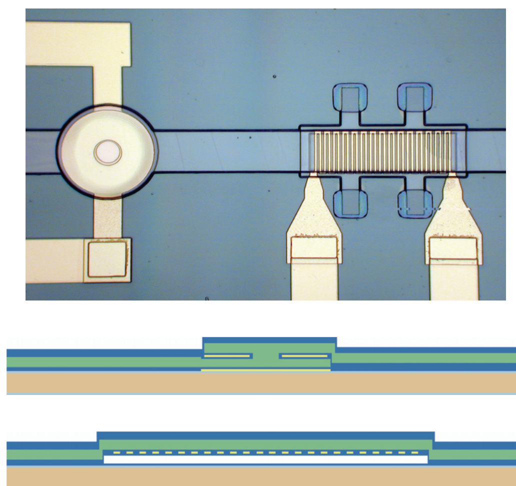

Figure 2-8: Picture and cross section of a flow control system consisting of an electrostatic valve (left) and thermal flow sensor (right)

In-channel pressure sensors, as seen in Figure 2-9, have also been reported[25]. This sensor used the deflection of a circular membrane integrated into the bottom of the channel to determine the relative pressure inside. The deflection of the membrane was measured using capacitive techniques. The sensor was characterized from 0–35 kPa and demonstrated a resolution of 0.03 kPa.

Sensors have also been developed to measure the electrical properties of the fluid inside Parylene channels. By measuring the electrical properties of the liquid, the composition of miscible organic/aqueous solutions were determined[24, 25] (also see Chapter 3). Also, integrated electrochemical/coductivity detectors were used for analyte detection in miniaturized separation systems[26, 27] (also see Chapter 6).

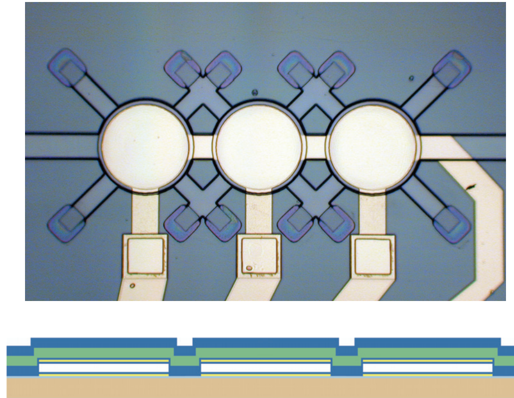

Figure 2-9: Picture and cross section of an electrostatically actuated peristaltic pump. Individual chambers also can serve as pressure sensors.

2.3.2. Pumps

A low flow rate (< 2 nL/min) mechanical peristaltic pump based on the sequential electrostatic actuation of three separate chambers was demonstrated and can be found in Figure 2-9[28].

Pumps based on the electrolysis of water have been demonstrated and integrated with Parylene channels[29-31] (also see Chapters 4 and 6). These electrolysis pumps functioned by harnessing the pneumatic pressure generated by the breakdown of water into hydrogen and oxygen. These pumps have demonstrated flow rates as high 1 mL/min when there is little or no backpressure. Pumping at low flow rates (< 200 nL/min) at backpressures as high as 50 bar have been shown as well.

Finally, electrically driven pumping techniques such as electro-osmotic flow[32] and electrohydrodynamic[33] pumping have been demonstrated in Parylene channels.

2.3.3. Valves

Several designs of check valves have been demonstrated[34-38]. These check valves operate by utilizing the vertical motion of a Parylene flap or diaphragm to alternately seal or reveal an opening depending on the flow direction. An example can be found in Figure 2-10.

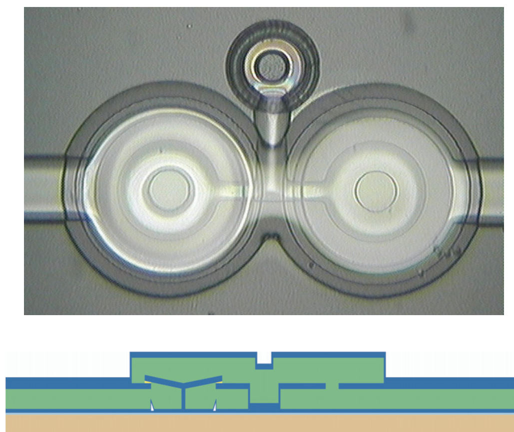

Figure 2-10: Picture and cross section of a normally closed passive check valve

Active valves have also been demonstrated. Like the check valves, these valves operated based on the vertical movement of a flap or diaphragm to open or close an opening. Actuation methods include electrostatic[21], thermal[39], and hybrid techniques[40]. An example of an electrostatically actuated valve is shown in Figure 2-8.

2.3.4. External Detector Interfacing

An electrospray nozzle, which could be interfaced to a mass spectrometer[41], was demonstrated. An example is shown in Figure 2-11. These nozzles have been used to couple the output of chip-based analyses to a mass spectrometer[30, 31, 42] (also see Chapter 5) with performance comparable to pulled fused silica nozzles.

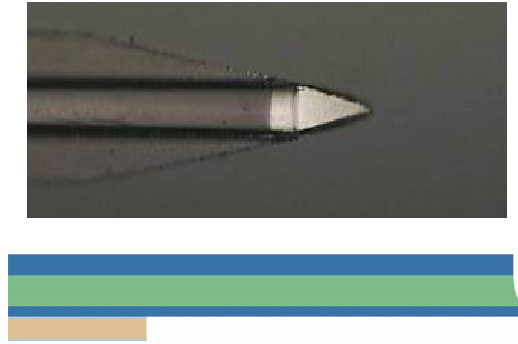

Figure 2-11: Picture and cross section of an electrospray nozzle

2.3.5. Passive Fluidic Structures

Common passive fluidic structures have also been demonstrated. Passive, diffusion-based mixers[24, 31, 43] (also see Chapters 3, 5, and 6), which rely on reducing the diffusion lengths, have been used for a variety of liquids and flow rates.

Filters for the collection of particles have been demonstrated. These include in-channel weir-type filters, which rely on a decrease in channel height to filter particles[31] (also see Chapters 5 and 6), as well as filters that utilize many small holes etched in a Parylene membrane.

2.4. Conclusions

The presented Parylene-based surface micromachining technology has several advantages that stem from its reliance on widely used and developed microelectronics manufacturing techniques. Because the process is lithography-based, it is easy to fabricate devices on a large scale. Lithographic techniques also enable the processes to utilize a large number of layers without having to worry about layer-to-layer alignment. It is this ability to use many different layers that allows us to make a large variety of devices of varying complexity. Another advantage of using the same techniques from the

microelectronics industry is that we could potentially create microfluidic devices on top of pre-fabricated integrated circuits. The integration of electronics with fluidics could lead to highly miniaturized microfluidic systems.

A second advantage of the technology is that it can be used to create a large number of demonstrated devices. Also, because these devices share a common technology, the ability to integrate different components is made much easier. In general, fabricating a system with many different components is no more difficult than fabricating the single most complicated component in the system. The ability to integrate many components together will be demonstrated in the following chapters.

A final but important advantage comes from the unique properties of Parylene. Its low permeability, optical transparency, high mechanical strength, excellent dielectric properties, and biocompatibility all make it an ideal material from both a mechanical and chemical standpoint.

Probably the most serious disadvantage of this technology is that it is more complicated than some of the other available microfluidic technologies both in terms of the number of processing steps and specialized fabrication equipment it requires. Some alternative approaches are designed to go from conception to fabrication in just a few hours. However, this comes at the cost of limited capacity for mass production and limited functionality, reducing the scope of possible applications.

Chapter 3: Microfluidic Chip for Flow Control Applications

3.1. Introduction

Flow control is a very fundamental and challenging problem in the microfluidics field. It is especially critical with regards to the development of lab-on-a-chip systems. Currently, most demonstrated lab-on-a-chip devices have no closed-loop flow control and rely exclusively on open-loop control. This open-loop control often takes the form of physically defined fluid reservoirs or pre-calibrated pumping mechanisms. As the tasks that need to be accomplished on chip become more complicated, these simple methods become inadequate. For example, a pump that is part of a lab-on-a-chip device might be affected by changes in the working fluid's properties. Small changes in these properties could prevent the pump from delivering the desired flow rate and cause inaccuracies in the final analysis. For example, in a previously demonstrated fully-integrated high-performance liquid chromatography (HPLC) system on a chip[31], the lack of any closed-loop flow control led to non-reproducible separations. By integrating sensing systems into this and other microfluidic systems, these inaccuracies can be eliminated.

One of the most demanding flow control applications is nanoscale HPLC. HPLC is a powerful liquid phase separation technique, which separates a mixture of analytes based on their interaction with a solid stationary phase and a liquid mobile phase. HPLC is largely a fluid control problem where accurate and repeatable fluid flow is needed in

order to produce repeatable separations. There are a large variety of stationary phases and mobile phase chemistries, which can be used to separate analytes based on size, charge, hydrophobicity, and many other properties. One of the most widely used techniques is reverse-phase HPLC. Reverse-phase separations use a hydrophobic stationary phase in conjunction with a mobile phase generally consisting of water/acetonitrile. Some separations require only the use of an isocratic elution, where the water/acetonitrile ratio is constant throughout the separation. For more complicated samples, gradient elutions, where the water/acetonitrile ratio is varied during the separation, are needed. As a result, any flow control system designed for HPLC must have accurate control over both the fluid composition and flow rate. This is complicated by the fact that nanoscale HPLC occurs at flow rates < 200 nL/min and can require water/acetonitrile compositions ranging from 0–50%. HPLC is also performed at high pressures, putting further strain on the flow control system.

Sensors form the core of any flow control system. Because flow rate is one of the most important physical parameters, several types of flow sensors have been demonstrated, the most common being thermal[44, 45], electrochemical[46, 47], and those based on hydrodynamics[48, 49]. However, these sensor types share one drawback; their response is dependent on the properties of the fluid. This is not ideal in situations where the fluid composition is constantly changing. In order to obtain a more reliable measurement of flow rate, a time-of-flight (TOF) approach is used here, where the flow sensor measures the time it takes a tracer pulse to travel a certain distance. This gives a direct measurement of linear flow velocity, which is directly related to the volumetric flow rate. The main advantage of a TOF flow sensor is that its response should be independent of

the working fluid. Different types of TOF flow sensors have been researched in the past, with thermal pulse[50, 51] and electrochemical pulse[52, 53] sensors being the most common. An electrochemical pulse was used in this work. The advantage of an electrochemical pulse over a thermal pulse is that the pulse is isolated inside the microchannel, resulting in less pulse broadening. A thermal pulse, on the other hand, would broaden as it loses heat to the microchannel walls. Another important class of microfluidic sensors is those used to sense changes in the fluid composition. In this work, to measure the water/acetonitrile ratio, a measurement of the electrical properties of the fluid was conducted. This is a proven concept which has been used to measure the composition of all different states of matter.

This chapter will cover the development of flow and composition sensors that are compatible with nanoscale reverse-phase HPLC. Because these sensors were designed with specifically reverse-phase separations in mind, water/acetonitrile (0.1% formic acid) solutions ranging from 0 to 50% acetonitrile were used in all experiments. The sensors were also designed for flow rates < 200 nL/min and pressures > 40 bar.

3.2. Experimental

3.2.1. Chip Design

Two different chip designs will be discussed in this chapter. Both chips were designed to be interfaced with a two-channel pumping system (e.g., one channel being water and the other being acetonitrile). Both devices accepted the two input fluids, mixed them, and measured the total flow rate and composition, where composition was based on

volume and described as a percentage ($V_{component}/V_{total}\%$). The implementation of these chips into closed-loop flow control systems is discussed in Chapters 5 and 6.

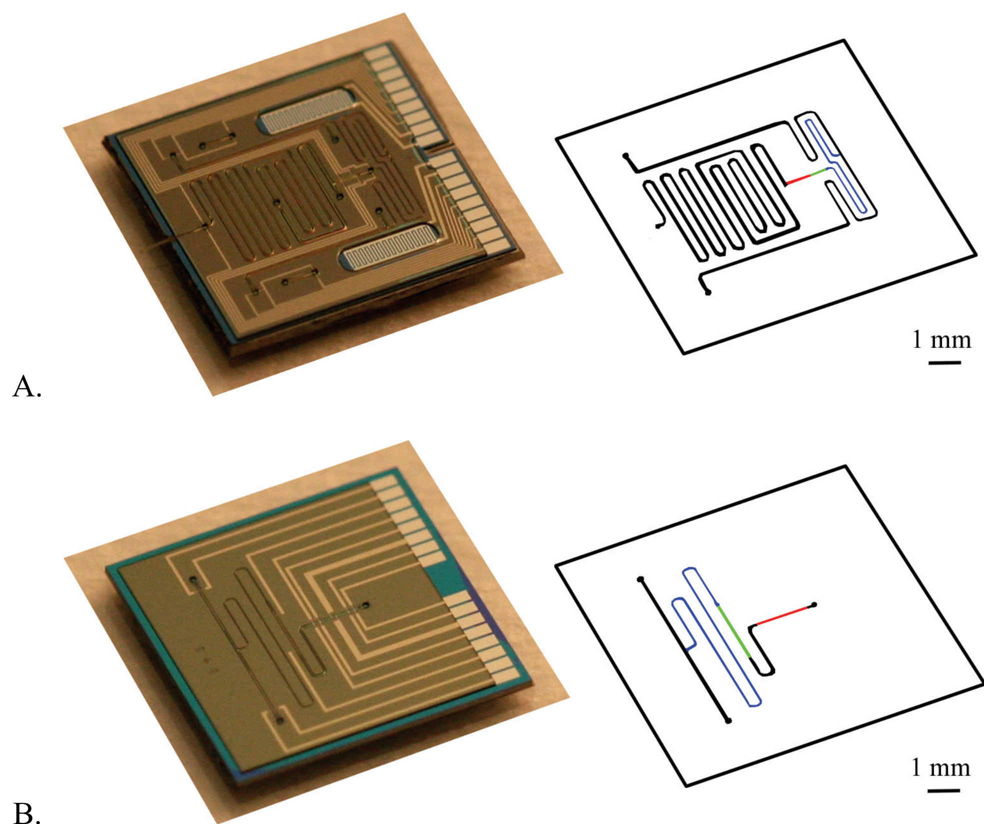

Figure 3-1: A picture and diagram of both the described chips. The various components are highlighted blue (mixer), green (composition sensor), and red (flow sensor). Both chips were 9.8 x 9.8 (L x W) mm^2. A. Integrated chip. B. Standalone chip

The two designs differed in their fluidic configuration and also sensor dimensions. In one approach, referred to as the integrated design and shown in Figure 3-1A, the output of the mixer was directed through the sensors and into a serpentine on-chip separation column. The second design, shown in Figure 3-1B and designated the standalone design, directed the flow out through a third fluidic port. Besides having a

different fluidic configuration, the standalone version also implemented changes in sensor design that improved sensitivity and accuracy.

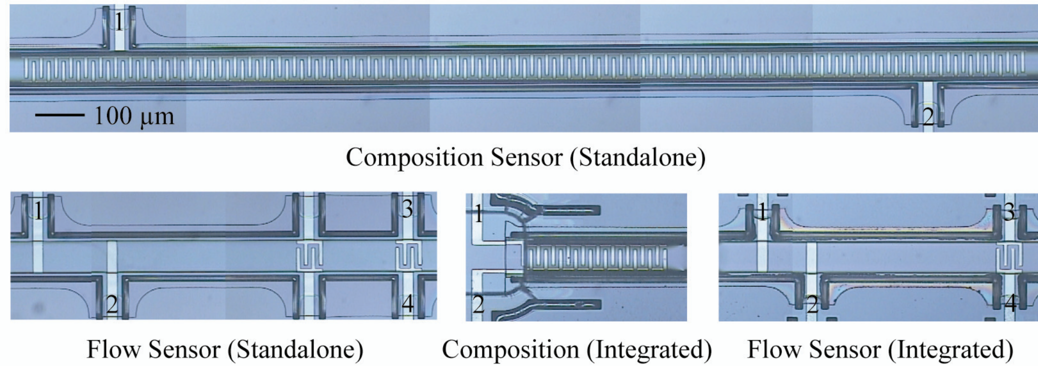

Figure 3-2: A close-up picture of all the sensor designs presented in this chapter. All devices are shown at the same scale.

Pictures of the sensors on integrated devices can be found in Figure 3-2. The composition sensor consisted of an interdigitated set of electrodes with an electrode width/spacing of 7.5/7.5 μm. The total area of the sensor was 70 x 300 (W x L) μm^2 and the microchannel dimensions were 80 x 25 (W x H) μm^2. For the flow sensor, the spacing between the pulse-generating electrodes (1 and 2) was 100 μm and the distance between the pulse electrodes' midpoint and detector electrodes (3 and 4) was 450 μm. The channel dimensions were 80 x 3.5 (W x H) μm^2. The integrated mixer (not shown in Figure 3-2) was 30 x 25 (WxH) μm^2 in cross section and 8.8 mm long.

Close ups of the sensors on the standalone device can be found in Figure 3-2 also. The composition sensor also consisted of a set of interdigitated electrodes with a width/spacing of 7.5/7.5 μm. The total area of this sensor was increased to 70 x 2000 (W x L) μm^2 and the microchannel dimensions were 80 x 20 (W x H) μm^2. For the flow sensor, the spacing between the pulse electrodes (1 and 2) was increased to 150 μm and

the spacing between the pulsing electrodes and the detector electrodes (3 and 4) was also increased to 675 µm. The channel dimension remained unchanged at 80 x 3.5 (W x H) μm^2. A second pair of detection electrodes was also fabricated and located only 475 µm from pulsing electrodes' midpoint. These detector electrodes were designed for lower flow rates but were not used in any experiments. The integrated mixer (not shown in Figure 3-2) was 30 x 20 (WxH) μm^2 in cross section and 15.7 mm long.

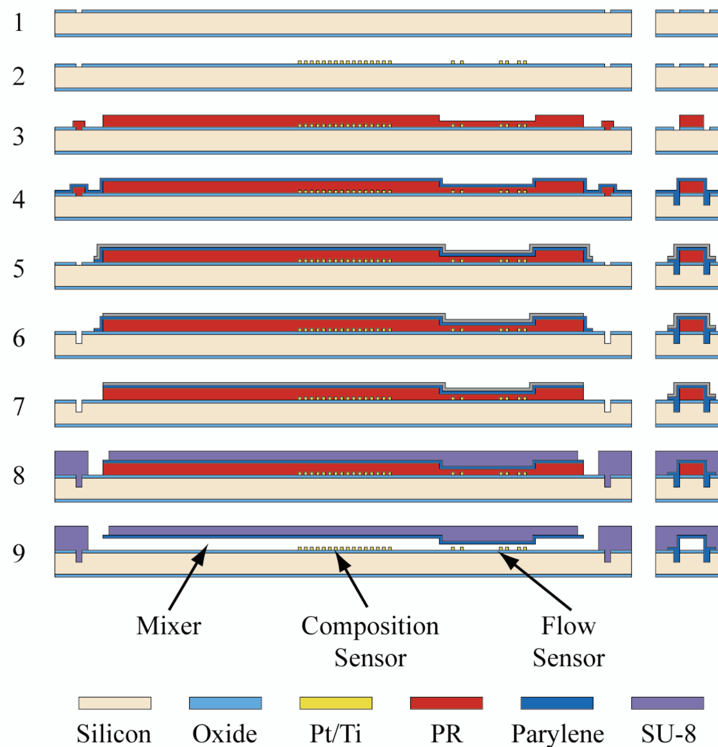

Figure 3-3: Process flow showing the fabrication of the standalone device. The left-hand column shows a cross-sectional view where the liquid flow is from left to right. The right-hand column shows a cross-sectional view where the flow is into the page.

3.2.2. Chip Fabrication

The technology used to fabricate these devices was described in detail in Chapter 2. These chips utilized the high-pressure anchoring technology and SU-8-based fluidic

ports outlined there. The process to make both these chips was identical and is diagrammed in Figure 3-3. The process could be broken down into nine basic steps as follows:

1. Silicon Oxide Deposition and Patterning: A 4000 Å silicon oxide (SiO_x) layer was grown on a silicon wafer. Next, a 5 µm AZ1518 photoresist layer was spun on the wafer and patterned using photolithography. The exposed silicon oxide was then etched using a buffered HF solution. Afterwards, the photoresist was stripped using acetone and isopropyl alcohol. The oxide layer served two functions. First, as an insulation layer between the electrodes and the silicon wafer, and second, as a mask for DRIE etching (see step 4).

2. Metal Deposition and Patterning: A 3 µm composite lift-off photoresist layer made up of LOR3B and AZ1518 was deposited and photo-patterned. The use of LOR3B as the base layer created a re-entrant profile ideal for lift-off. Then a 200/2000 Å Ti/Pt layer was deposited via e-beam deposition. The Ti was used to improve adhesion between the Pt and the oxide surface. After metal deposition, liftoff was accomplished by dissolving the photoresists using ST-22 photoresist stripper. The resulting metal layer was used to define all the active electrodes, as well as the metal lines and pads needed for electrical connections.

3. Sacrificial Photoresist: A 25 µm AZ4620 photoresist layer was spun on the wafer. By using two exposures, one full, and one partial, a bi-level (25 µm/3.5 µm), monolithic photoresist structure was produced. A bi-level sacrificial layer was necessary to reduce the channel height where the flow sensor was located. This sacrificial photoresist layer

was temporarily used to define the channel and would eventually be dissolved away (step 9).

4. Parylene Anchors and Deposition: Using a deep reactive ion etching (DRIE) instrument, 40-µm-deep trenches were created on the sides of the channels. The oxide, patterned in step 1, was used as a mask for DRIE etching. Afterwards, a 10 µm Parylene layer was deposited. The DRIE trenches took advantage of the conformal nature of the Parylene deposition and served to anchor the Parylene layer to the substrate. By mechanically anchoring the encapsulating layer, much higher pressures could be sustained by the channels.

5. First Parylene Patterning: A 200/2000-Å-thick Cr/Au layer was e-beam deposited and patterned by using a 40 µm AZ4620 photoresist mask. The metal was etched using Au etchant type TFA (KI) and CR-7 Cr etchant (perchloric acid). After metal etching, the photoresist was stripped using acetone and isopropyl alcohol. The Cr/Au metal layer was then used as an etch mask for Parylene patterning, which was accomplished using an oxygen plasma. This patterning was used to remove Parylene over the areas where the SU-8 anchors would be etched (step 6).

6. SU-8 Anchors: Before the formation of the SU-8 anchors, the Cr/Au layer was patterned again using the same process outlined in step 5. Then, a thick 40 µm AZ4620 photoresist layer was spun and patterned. This formed a mask to DRIE etch shallow 30 µm trenches near the SU-8 edges. The photoresist was stripped using acetone and isopropyl alcohol.

7. Second Parylene Patterning: The Parylene was etched in oxygen plasma using the Cr/Au mask patterned in step 6. After Parylene etching, the metal mask was stripped using Au etchant and Cr etchant.

8. SU-8 Encapsulation: A 50-μm-thick SU-8 layer was spun on the wafer and patterned. This SU-8 layer filled the trenches (step 6), which helped improve SU-8 adhesion to the substrate. This was especially critical, as the entire chip would be soaked in harsh organic solvents later in the process (step 9). The SU-8 also helped to strengthen the channels further so they could withstand the high operating pressures. Finally, the SU-8 sealed the regions where the electrodes crossed into the channel, preventing these areas from leaking during high-pressure operation.

9. Photoresist Dissolution: To finish the chip, the sacrificial photoresist was dissolved away using acetone and the wafer was diced to yield the individual devices

3.2.3. Composition Sensor

The composition sensor relied on a measurement of the fluid electrical admittance to deduce the water/acetonitrile percentage. The sensor on the integrated device was operated by applying a 500 kHz, 200 mV AC (HP8111A, Agilent Technologies) signal across electrodes the two electrodes (1 and 2, see Figure 3-2 for electrode numbering). The resulting current was measured using an I→V converter with a gain (V_{pp}/I_{pp}) of 3.18×10^4 Ω (OP37, Analog Devices). The AC voltage output was converted to a DC signal using an AC→RMS converter (AD636, Analog Devices). The total gain (V_{out}/I_{pp}) was 1.12×10^5 Ω. The operation of the sensor on the standalone device was identical

except for the use of a 100 kHz, 200 mV excitation signal and a reduced total gain (V_{out}/I_{pp}) of 1.07×10^5 Ω.

Prior to sensor use, the electrodes were electrochemically cleaned by cycling the electrode voltage between -2.0 and +2.0 V repeatedly until consistent current profiles were achieved (e.g., cyclic voltamograms). This conditioning of the electrodes improved the stability and repeatability of the sensor measurements.

3.2.4. Flow Sensor

The flow sensor was a TOF sensor that measured the velocity of an electrochemically generated ion pulse. On the integrated device the electrochemical pulse was generated by applying a +25 V, 7 ms square pulse to upstream pulse electrode (1) while the downstream pulse electrode (2) was grounded (see Figure 3-2 for electrode numbering). This electrical pulse was created by using a HP33120A arbitrary function generator (Agilent Technologies) that switched a high-voltage LCC110 solid-state relay (Clare, Inc.). The voltage was supplied using an HP6209B variable DC voltage supply (Agilent Technologies). Downstream ion pulse detection was achieved by measuring the fluid admittance. This was accomplished by applying a 20 kHz, 100 mV AC signal (HP8904A, Agilent Technologies) across the detector electrodes (3 and 4). The resulting current was measured using an I→V converter with a gain (V_{pp}/I_{pp}) of 5×10^5 (OP27, Analog Devices). The amplitude of signal was measured using an EG&G 5206 2-phase lock-in amplifier (Princeton Applied Research) using an integration time of 3 ms and a gain of 200. Overall gain (V_{out}/I_{pp}) was 1×10^8 Ω. The operation of the sensor on the

standalone device was identical except for the use of a 30 kHz, 200 mV AC excitation signal and a reduced overall gain (V_{out}/I_{pp}) of 1.67×10^7 Ω.

As with the composition sensor, cyclic voltamograms were repeatedly conducted on the detector electrodes (3 and 4) until stable results were given. This improved the sensitivity of the electrodes to the passing ion pulses.

3.2.5. Sensor Calibration

To calibrate the sensors, the chips were connected to a commercial HPLC pump (Agilent 1100 Series Nano Pump or Agilent 1100 Series Quaternary Pump) equipped with a water/acetonitrile (0.1% formic acid) solvent system. All sensors were controlled and monitored using a DAQPad-6020E data acquisition unit (National Instruments) in conjunction with LabVIEW (National Instruments). Flow rate measurements were conducted at a frequency of 0.1 Hz and composition measurements at 1 Hz.

To provide a realistic environment for calibration, the sensors were operated at pressures consistent with nanoscale HPLC. For the case of the integrated chip, this was done by directing the output flow from the sensors into the on-chip serpentine channel. The channel was packed with 5 µm C_{18} beads (Grace Vydac) to produce a high backpressure. For the standalone chip, an appropriate length of 15 µm ID fused silica tubing (Polymicro Technologies) connected to the chip outlet was used to provide the backpressure. Calibration backpressures ranged from 10 to 50 bar.

3.2.6. Chip Packaging

Fluidic connections to the chips were made using a CNC-machined Ultem (polyetherimide) fluidic manifold. The manifold was clamped onto the top chip surface and micro o-rings (Apple Rubber) were used to create a seal between the chip and manifold. Grooves were used to hold the o-rings and chip in place to facilitate alignment. Ports were machined into the manifold and used with commercially available fittings (Upchurch Scientific). The fittings allowed direct connection of standard 360 μm OD fused silica tubing (Polymicro Technologies) to the chip. The ports were machined as specified by Upchurch and provided a minimal dead volume and high-pressure-capable connection. Total connector volume was estimated to be < 8 nL. Electrical connections between the external circuitry and the chip were accomplished by using spring-loaded electrical probes (Everett Charles Technologies). An electrode block that housed up to 20 of these probes was made. The electrode block was positioned and then clamped down on the electrical pads to make contact with the chip. The other end of the electrical probes was clamped against a printed circuit board (PCB) that was connected to the measurement circuit. One example of a packaged device is shown in Figure 3-4.

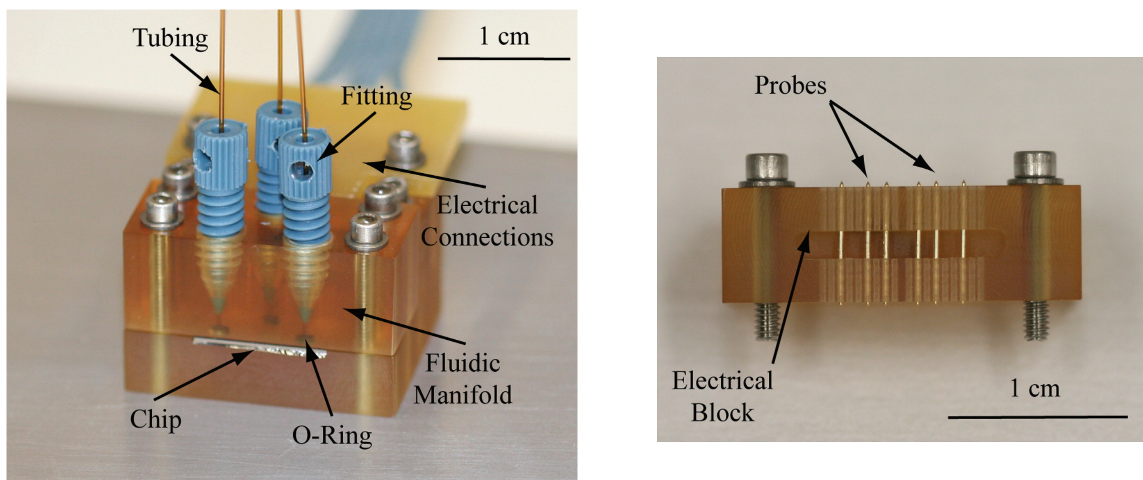

Figure 3-4: Packaged standalone device and close-up view of the electrode block

3.3. Results and Discussion

3.3.1. Mixer

The mixer relied completely on passive diffusion. The small cross section of the mixer brought the two incoming flows in close contact, reducing the distance the two liquids had to diffuse for complete mixing. The mixer dwell time (about 4 seconds for the integrated chip and 6 seconds for the standalone chip at 100 nL/min) was more than adequate to achieve complete mixing. In fact, total mixing was likely achieved after only 1 second based on the known diffusion constants of acetonitrile and water. Similar designs had been used to great effectiveness in the past[31, 54].

The mixer played no functional role in any of the experiments described in this chapter. Its role was more prominent when these devices were interfaced with pumps for feedback-controlled experiments. This is described in Chapters 5 and 6.

3.3.2. Composition Sensor

Binary mixtures of liquids were expected to have different electrical properties at varying compositions. This was especially the case in water/acetonitrile mixtures where one component is conductive (water), while the other is an excellent insulator (acetonitrile).

One important consideration that had to be taken into account was possible changes in the electrode surface, whether by metal degradation or absorbed molecules. These changes to the electrode surface caused a shift in the double layer capacitance and could produce changes in the sensor readings over time. This was particularly the case

for our microelectrodes, where the double layer capacitances and fluid impedance were both low. An equivalent circuit can be found in Figure 3-5. To negate these electrode surface effects, the measurement frequency had to be high enough to make the AC impedance of the double layer capacitances much smaller than the bulk fluid impedance. In the case of the sensor on the integrated device, a frequency of 500 kHz was needed to provide good stability. The downside of increasing the measurement frequency was that the large parasitic capacitances would dominate the overall sensor response. This was especially the case for the composition sensor on the integrated device, where the combined AC impedance of the double layer and bulk fluid was large compared to the AC impedance of the parasitic capacitance. To overcome this problem, a 10 mH inductor was placed in parallel with the sensor, which when combined with the parasitic capacitance, produced an LC circuit that resonated near the 500 kHz measurement frequency. The equivalent circuit is also shown in Figure 3-5.

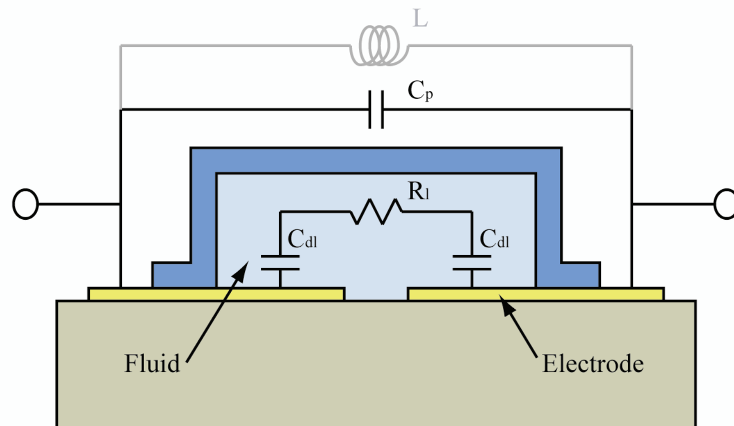

Figure 3-5: Equivalent circuits for the composition sensor. C_{dl} is the double layer capacitance, R_l is the fluid resistance, C_p is the parasitic capacitance, and L is an external inductor only used in the resonant-enhanced measurement circuit

This technique[55] resulted in a measurement largely dominated by the fluid conductivity. The overall impedance of the non-resonant circuit is given by:

$$|Z| = \sqrt{\frac{4 + C_{dl}^{2} R_{1}^{2} \omega^{2}}{\omega^{2}(4C_{dl}C_{s} + 4C_{s}^{2} + C_{dl}^{2}(1 + C_{s}^{2} R_{1}^{2} \omega^{2}))}} \text{. (equation 1)}$$

When an inductor that satisfies the resonant condition,

$$\omega_{o} = \frac{1}{\sqrt{LC_{p}}} \text{, (equation 2)}$$

is added in parallel to the sensor, the overall impedance becomes

$$|Z| = \sqrt{R_{l}^{2} + \frac{4}{\omega_{o}^{2} C_{dl}^{2}}} \text{, (equation 3)}$$

where as long as the resonant/measurement frequency is high, should be approximately equal to the fluid impedance.

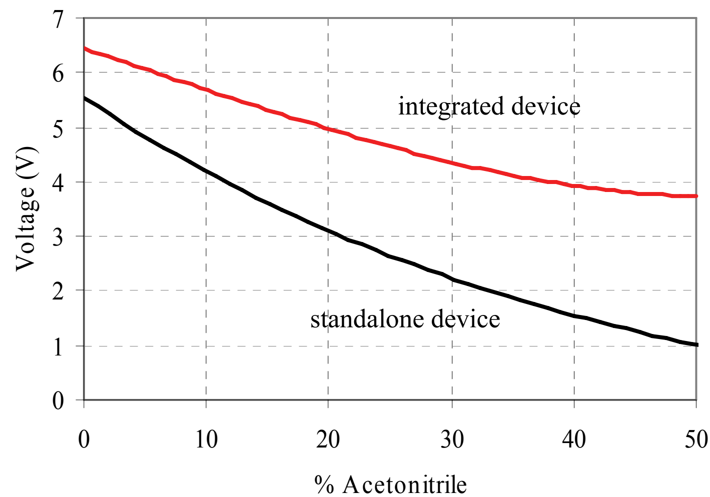

Figure 3-6: Example calibration plots for the composition sensors on the integrated device (500 kHz, 200 mV with resonant circuit) and standalone device (100 kHz, 200 mV with non-resonant circuit).

A calibration curve for the composition sensor on the integrated device is shown in Figure 3-6. The sensor precision was 0.3% acetonitrile and accuracy was estimated to be better than 1%. One drawback with this sensor was that there was a decrease in sensitivity at the higher organic compositions. This was likely due to changes in the circuit response as the resonant frequency shifted away from the measurement frequency (e.g., 500 kHz). This is possible because changes in fluid composition are accompanied by changes in fluid dielectric constant, which has a direct affect on the parasitic capacitance. A second cause is a natural saturation in the fluid impedance at higher organic ratios.

The composition sensor on the standalone device was designed to address the deficiencies in the first design. By greatly increasing the electrode area, the double layer capacitance was increased and the fluid impedance was decreased. This allowed the measurement frequency to be increased without using a resonant circuit to compensate for the parasitic capacitance. Not only did this simplify the measurement circuit, the measurements were no longer affected by non-ideal effects that occurred when the resonant frequency of the circuit shifted. Calibration data for the standalone device sensor is shown in Figure 3-6 and confirmed the expected improvement. The sensitivity was improved by roughly a factor of two and the sensor response at the higher acetonitrile percentages was also improved without sacrificing long-term stability.

It should be noted that this type of sensor was sensitive to many factors, including the amount of dissolved gas in the fluids, the exact formic acid percentage, as well as the temperature of the chip. To get accurate absolute measurements of the fluid composition, our solvents had to be carefully prepared. Our solvent preparation was based on standard

LC protocols and included the use of high-purity solvents and degassed liquids. While this gave us very repeatable results using a single chip with a single batch of solvents, solvent batch-to-batch as well as chip-to-chip variations eventually need to be accounted for. One potential way to account for possible variations is to have separate sensors to measure the bulk electrical properties of the two individual fluid components prior to mixing. This would provide a baseline upon which to base our composition measurements.

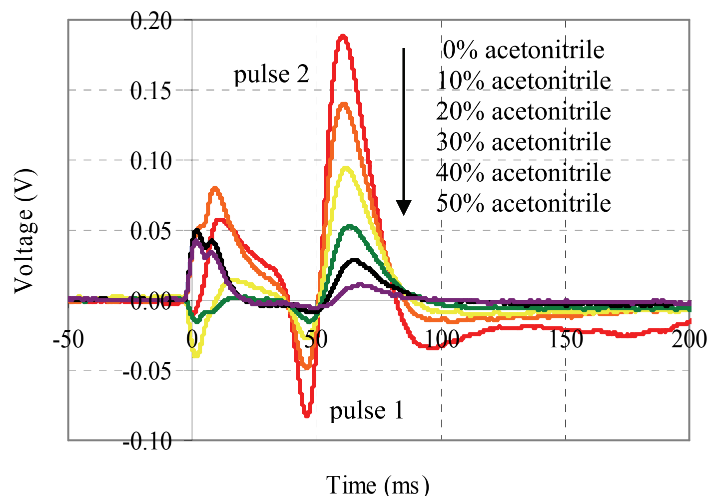

Figure 3-7: Sample waveforms collected using the integrated device. The different waveforms correspond to different fluid compositions ranging from 0–50% acetonitrile (10% intervals). A flow rate of ~ 140 nL/min was used to generate all the waveforms. The pulse was generated at t = 0 ms.

3.3.3. Flow Sensor

In aqueous solutions, the main electrochemical reaction at the pulse electrodes (1 and 2, see Figure 3-2 for electrode numbering) was the electrolysis of water:

$$\text{Anode (Electrode 1): } 2H_2O \rightarrow O_2 + 4H^+ + 4e^-$$

Cathode (Electrode 2): $2H_2O + 2e^- \rightarrow H_2 + 2OH^-$

Overall: $2H_2O \rightarrow 2H_2 + O_2$

This effectively produced two ion pulses. First, a pulse with an excess of ions (formed at electrode 1) resulting from the production of H^+. And second, a depletion of ions (formed at electrode 2) resulting from the neutralization of the H^+ ions naturally present in the solution (0.1% formic acid).

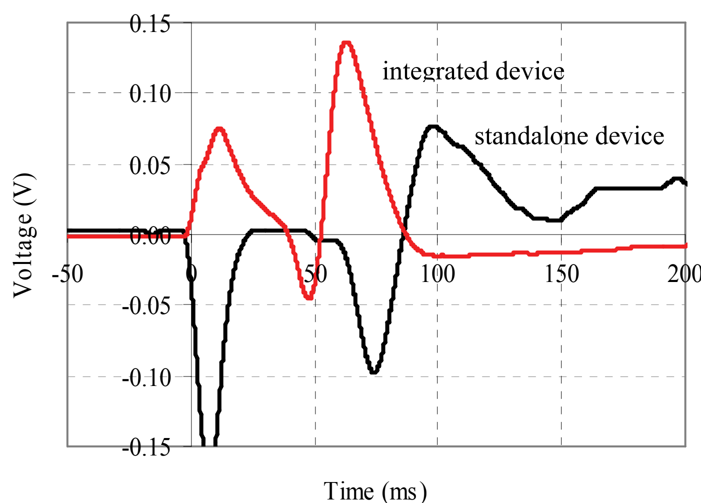

Figure 3-8: Sample waveforms comparing the response of the integrated device and standalone device. Both waveforms were collected at a flow rate of 140 nL/min and using a 10% acetonitrile solution. The pulse was generated at t = 0 ms.

Waveforms collected using the integrated device can be found in Figure 3-7. They showed the expected response and registered two separate ion pulses corresponding to the ion depletion and ion excess. There was a baseline shift in the waveforms at different compositions. This was expected and was caused by the same principles governing the composition sensor. This baseline shift is not seen in Figure 3-7 as the baseline level of the waveforms have all been zeroed for clarity. A comparison between

the waveforms seen in the integrated device versus the standalone device can be seen in Figure 3-8. As expected, both the peak and valley were shifted to a later time in the standalone device (e.g., peak position: 62.7 versus 98.8 ms, valley position: 46.7 versus 73.6 ms). Also, the time between the valley and peak (e.g., 16.0 versus 25.2 ms) increased, as was expected given the larger pulsing electrode spacing. These increases in TOF and valley/peak spacing matched up well with the corresponding 50% increase in the electrode spacing in the standalone design.

A calibration plot for the flow sensor on the integrated device is shown in Figure 3-9. Sensor precision was 0.9 nL/min and accuracy was estimated to be better than 3 nL/min. The calibration data for the flow sensor on the standalone device is also shown in Figure 3-9. For both designs, the sensor response closely followed the expected inverse relationship between TOF and flow rate as shown by fitted curves. This indicated relatively ideal behavior of the ion pulses. An increase in sensor precision was not seen with the standalone design. This was an indication that the main factor likely limiting the precision of the sensor was the width of the detector area. A smaller detector would have likely improved the time resolution. The measured TOFs were in close agreement with the expected TOFs, which are also plotted in Figure 3-9. The expected TOFs were calculated solely based on the physical dimensions of the channel and the volumetric flow rate. The discrepancy was well within the margin of error when taking into account uncertainty in the channel dimensions. When comparing sensors on different chips, the variation was low (< 5%). Chip to chip variation was limited only by how accurately we could control the sensor dimensions.

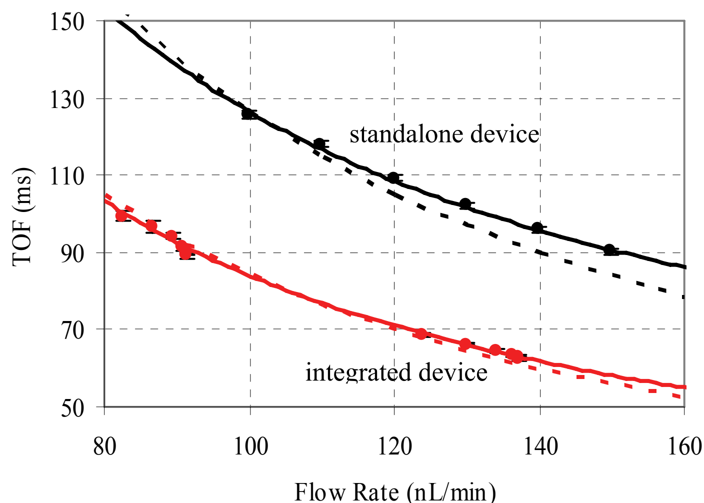

Figure 3-9: Flow sensor calibration plots for both the integrated and standalone devices. The TOFs correspond to the peak position. The points are fitted (solid line) assuming an ideal inverse relationship between TOF and flow rate. The dotted line represents the expected TOFs based only on the physical sensor dimensions and flow rate.

One problem with this type of sensor was that it ceased to function at higher acetonitrile percentages. This is evident in Figure 3-7, where decreased sensitivity to the ion pulses was observed at the higher organic compositions. This was most likely because the bulk fluid impedance began to saturate at the higher organic compositions, reducing the effect additional ions in the solution had on the fluid admittance. The increase in fluid impedance also would have caused fewer ions to be generated via electrolysis. One possible solution that was investigated was to try and improve detection by looking at the phase dependence of the pulse detection system. During normal sensor use, only the amplitude of the current was measured with no regard to phase. The use of a lock-in amplifier allowed for the phase dependence of the detector electrodes to be studied. Figure 3-10 shows waveforms collected using different phase offsets. The

detector waveforms exhibited a marked difference. For example, as the phase setting was increased from 0 to 90º, there was increased sensitivity to the peak and reduced sensitivity to the valley. Here, a phase setting of 0° corresponded to looking at the waveform component in-phase with the excitation signal, after accounting for the inverting I→V converter. It is likely that the phase could be tuned for optimum sensitivity to either the peak or valley, potentially allowing flow measurements over a larger composition range.

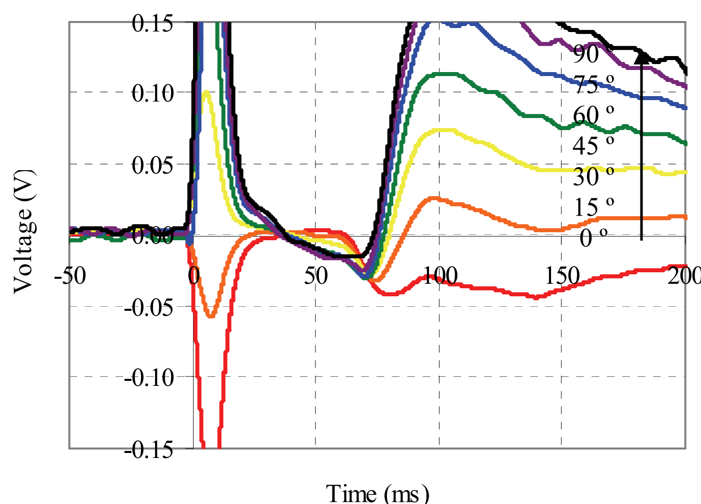

Figure 3-10: Sample waveforms collected using the flow sensor on the standalone device. The flow rate was 140 nL/min for all waveforms and a 10% acetonitrile solution was used. The pulse was generated at t = 0 ms.

Changes in the sensor design could also be implemented to extend the compositional range of the flow sensor. For example, it would be possible to add a tracer molecule in the liquid that is electrochemically active. This would generate a strong electrochemical pulse that would be detected regardless of the fluid composition. A second possibility is to use a thermal pulse instead of an electrochemical pulse.

Unfortunately, a thermal pulse, while likely to work for any fluid, is more susceptible to broadening. A final possibility is to place the flow sensor at the head of the mixer, prior to any significant mixing of the two flows. The sensor response would likely be dominated by the aqueous “section” of the flow, allowing flow measurements even when a majority of the flow was organic.

3.4. Conclusion

Sensors that meet the requirements of nanoscale HPLC have been developed and characterized. Both sensors were designed to work for flow rates < 200 nL/min, pressures > 40 bar, and fluid compositions ranging from 0–50% acetonitrile. While the sensors both demonstrated reduced sensitivity at higher acetonitrile percentages, this should not affect their application in HPLC as the majority of separations do not require acetonitrile percentages much higher than 50–60%.

Chapter 4: High-Pressure Electrolysis Pumping

4.1. Introduction

The ability to move fluids is one of the most basic tasks in microfluidics. As described in Chapter 1, pumping is generally achieved using non-mechanical methods, such as electro-osmotic flow, or mechanical methods, such as miniature diaphragm or peristaltic pumps. A summary of the major classes of pumps was discussed in Chapter 1. Because of their simplicity, electrically driven flows are generally used in microfluidic systems. Mechanical pumps are usually avoided when it comes to lab-on-a-chip systems as they are seen to be too complex and unreliable.

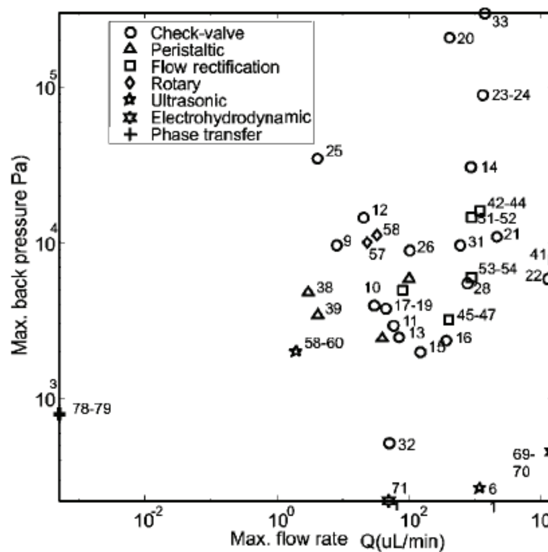

Figure 4-1: Different classes of microfluidic pumps and their corresponding maximum backpressures and flow rates

The biggest challenge in creating a microfluidic high-performance liquid chromatography (HPLC) system is the development of a miniature high-pressure pumping system. To illustrate, Figure 4-1[12] contains a plot showing the maximum backpressure and flow rates of several demonstrated microfluidic pumps. None of the surveyed pumps are capable of use in nanoscale HPLC where pressures are > 40 bar ($4x10^6$ Pa) and flow rates are < 0.2 μL/min. Also, many of the pumps surveyed would not even work with the acetonitrile/water solutions used in reverse-phase HPLC. There has been some effort to build microfluidic high-pressure pumps, largely with HPLC in mind. The majority of these efforts have been based on electrokinetic forces. The most promising examples are those which use a packed capillary[56-58] or micromachined channels to increase the liquid/solid contact area and at the same time prevent pressure-driven backflow. These pumps, while demonstrated to pressures as high as 500 bar, require voltages ranging anywhere from 1000–7000 V. These pumps also generally require the use of specially designed solvents for optimal performance. Another potential problem is related to the use of extremely high voltages. The high voltages involved can have electrophoretic effects on the separation. While in some hybrid separation techniques this is actually desired, HPLC systems require a pressure-driven pumping system.

One alternative to high-pressure pumping, which has not been as well researched, are pumps based on the electrochemical generation of gas. In one form, these pumps operate by generating gas via electrolysis. The produced gas displaces the fluid out of the electrolysis chamber and into the desired target. This mechanism may not be considered "pumping" in the classical sense in that there is only a pump outlet while traditional

pumps have both an inlet where they draw liquid and an outlet where they expel it. The electrolysis pump is analogous to a syringe, where only a fixed amount of fluid can be delivered before a refill is needed. One advantage of these pumps is their ability to generate very high pressures. For example, the electrolysis of water is theoretically capable of pressures up to nearly 2000 bar[59]. While electrolysis of water as a pumping mechanism has been studied in the past[30, 60-63], it is still poorly understood and has only been characterized at pressures < 10 bar, which is not suitable for most HPLC separations.

This chapter will discuss the fabrication and characterization of a high-pressure pump based on the electrolysis of water. Because nanoscale reverse-phase HPLC is the targeted application, direct electrolysis of mobile phases (e.g., acetonitrile/water (0.1% formic acid) solutions) will be performed. The pumps are designed to operate in the nanoscale HPLC flow regime with flow rates < 200 nL/min and backpressures > 40 bar.

4.1.1. Electrolysis of Water

The electrolysis of water generates H_2 and O_2 via the following half reactions:

$$\text{Anode: } 2H_2O \rightarrow O_2 + 4H^+ + 4e^-$$

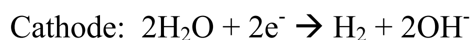

$$\text{Cathode: } 2H_2O + 2e^- \rightarrow H_2 + 2OH^-$$

$$\text{Overall: } 2H_2O \rightarrow 2H_2 + O_2$$

In the ideal situation, two H_2 molecules and one O_2 molecule are generated for every four electrons. In reality, there are possible side reactions, which can reduce the conversion efficiency. The minimum theoretical voltage for electrolysis is 1.23 V based on the Gibbs free energy of formation. In the case of Pt electrodes, an over-potential of at least 0.5 V is generally needed, bringing the minimum actual voltage to approximately 1.7 V.

The over-potential required is a function of the electrode material, electrode configuration, and ionic strength of the electrolyte. In general, the over-potential also gives a measure of how much of the total power input is dissipated as heat at the electrode/electrolyte interface.

4.2. Experimental

4.2.1. Device Design

The device consisted of a set of microfabricated planar electrodes on a soda-lime glass substrate. A picture and diagram of the electrode array can be seen in Figure 4-2. The central, circular electrode array had a diameter of 8.5 mm and the total chip dimensions were 17.5 x 15 (W x H) mm^2. The interdigitated electrodes had a width/spacing of 250 µm. A CNC-machined electrolysis chamber was constructed and placed over the electrodes. While a microfabricated electrolysis chamber could have been used, any micromachined chamber would have had a greatly reduced volume, likely on the order of a few µL. While this volume may have been suitable for a single separation, multiple separations would have been impossible without refilling. For example, a typical separation might last 1–2 hours at a flow rate of 150 nL/min, or a total volume of 0.9–1.8 µL. The CNC-machined electrolysis chamber had a volume of 300 µL, allowing for more than 30 hours of continuous operation. The larger electrolysis chamber also allowed for the integration of fluidic ports, which could be used for filling the pump and connecting the pump to other devices (e.g., the devices presented in Chapter 3). Finally, the CNC-machined chamber allowed for the integration of a commercial pressure sensor to better monitor the electrolysis process.

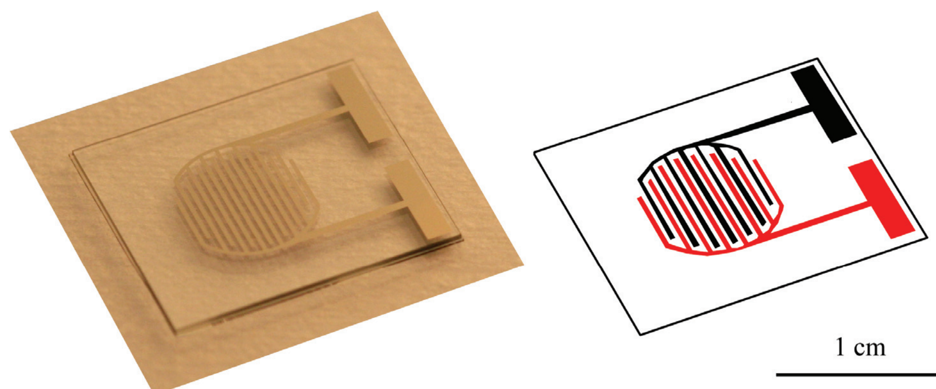

Figure 4-2: A picture of the electrode array

4.2.2. Chip Fabrication

The fabrication of the planar electrode array was straightforward and only required the deposition and patterning of a single Ti/Pt (200/2000 Å) metal layer. Lift-off patterning was used. The lift-off photoresist consisted of a 3 μm composite layering made up of LOR3B and AZ1518. The use of LOR3B as the base layer created a re-entrant profile ideal for lift-off. After the deposition of Ti/Pt using an e-beam evaporator, liftoff was accomplished by dissolving the photoresists using ST-22 photoresist stripper.

4.2.3. Pump Packaging

The electrolysis chamber was CNC machined using Ultem (polyetherimide) (McMaster Carr) and clamped over the electrolysis electrodes with an o-ring (McMaster Carr) providing the sealing. A picture of the packaged device can be found in Figure 4-3. Besides the opening that matched up with the circular electrode array, there were three other ports. One port, located on top of the device, was designed to accept a 0–70 bar flush mount stainless steel pressure sensor (PX600-1KGV, Omega Engineering, Inc.). Sealing at the pressure sensor junction was once again achieved using an o-ring

(McMaster Carr). A second port was used for pump filling purposes. During filling, this port was left open as a vent, and after filling, the port was plugged using a commercially available HPLC column plug (Upchurch Scientific). The final port was connected to a coil of Teflon FEP or stainless steel tubing (Upchurch Scientific) that served as the solvent reservoir. This connection was made using a commercial high-pressure fitting (Upchurch Scientific).

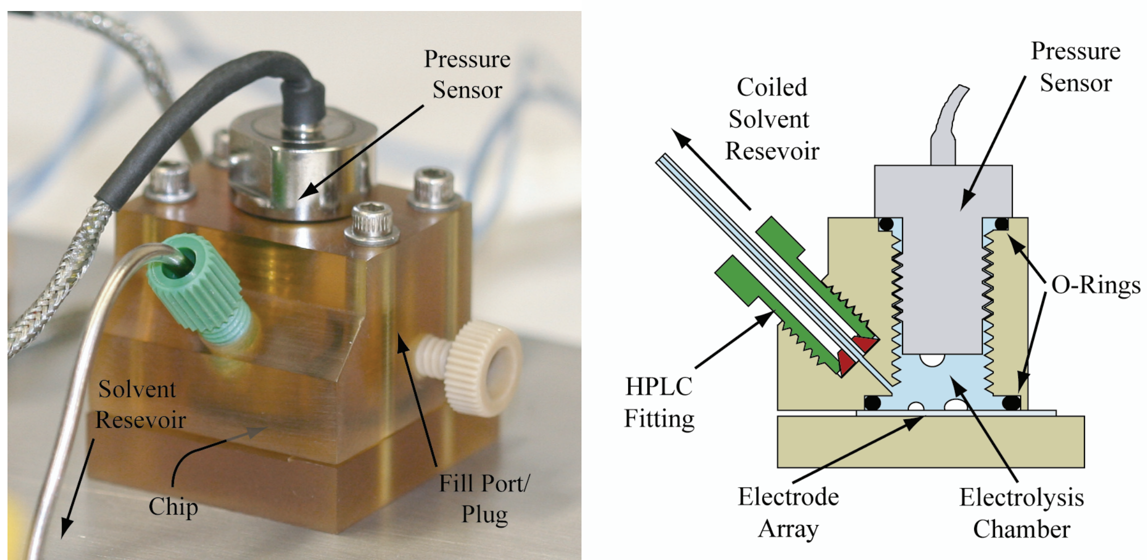

Figure 4-3: A picture of the packaged electrolysis pump along with a cross-sectional view. The electrolysis chamber is faintly visible in the center of the Ultem piece.

While the electrolysis chamber could have been simultaneously used as the solvent reservoir, we chose to use an external reservoir to prevent gas from contaminating the liquid. This is important for applications that are sensitive to dissolved gas, such as HPLC. The other end of the coiled tubing served as the pump outlet. For electrical connections, miniature screw terminals were positioned next to the on-chip electrical pads and used to clamp bare wires down onto the pads. The entire setup was capable of sustaining pressures > 70 bar.

4.2.4. Pump Calibration

The pump was filled by pumping degassed acetonitrile/water (0.1% formic acid) solutions into the pump outlet, through the coiled solvent reservoir, and into the electrolysis chamber. In this way, both the solvent reservoir and electrolysis chambers were filled simultaneously. The fill port was left unplugged during filling and closed again after the system had been completely filled. The pump was operated by passing a constant current through the electrolysis electrodes. The current was either supplied using a custom-built V→I converter (OP741, National Semiconductor) or a HP6186C DC current source (Agilent Technologies). The applied current, required voltage, and chamber pressure were recorded using a DAQPad-6020E data acquisition unit (National Instruments) in conjunction with LabVIEW (National Instruments). Data acquisition and electrolysis current control were both at 1 Hz.

Two different calibration methods were used to characterize the pump. In the first method, a valve was positioned at the end of the coiled solvent reservoir and placed in the closed position. A constant current was applied to the electrolysis electrodes and the rise in pressure inside the closed system was monitored. In the second setup, the outlet of the pump was connected to a 0–140 bar pressurized nitrogen gas cylinder. A constant backpressure was applied and a constant current fed through the electrolysis electrodes. The resulting flow rate was determined by measuring the linear velocity of the liquid/gas interface in a tube with known ID. In this setup, clear Teflon FEP rather than stainless steel tubing was used to observe the interface movement.

4.3. Results and Discussion

A majority of the experiments were conducted using the closed system setup. With the pump outlet closed off, currents ranging from 1–3 mA were applied to the electrolysis electrodes and the increase in internal pressure was monitored over time. Figure 4-4 shows the collected data when using a 100% water solution (0.1% formic acid). The maximum pressure generated during these experiments was approximately 50–60 bar, though higher currents readily resulted in faster pressure increases and higher maximum pressures.

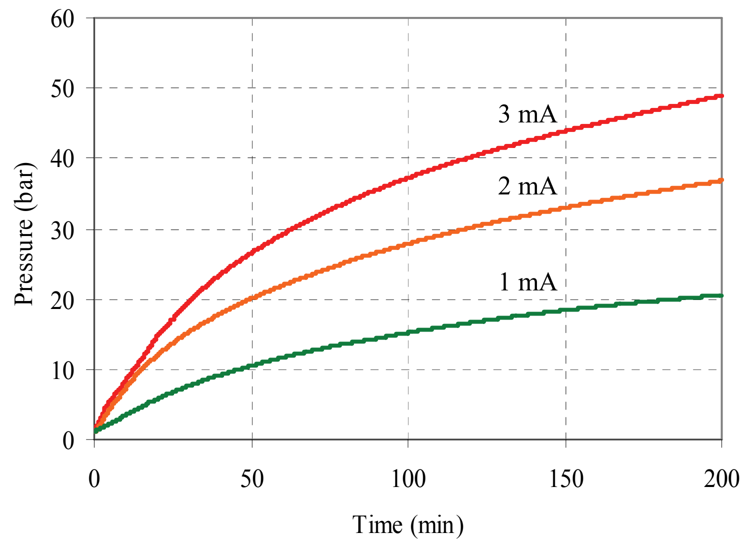

Figure 4-4: A plot showing the increase in pressure inside the closed electrolysis system at applied currents of 1, 2, and 3 mA. These three curves were collected using a 100% water solution (0.1% formic acid).

Developing a mathematical model to explain the pressure evolution in Figure 4-4 was important in understanding the underlying principles. The fundamental basis for our calculation was simply the ideal gas law:

$$P(t)V(t) = n(t)RT \text{ , (equation 1)}$$

where P(t) is the pressure, V(t) is the volume, n(t) is the total number of moles of gas, R is the universal gas constant, and T is the temperature. Given the volume and total molar amount of gas inside the chamber, the expected pressure could be readily calculated.

First, the evolution of the gas volume was characterized. If the electrolysis chamber was completely rigid and did not exhibit any pressure-related expansion, the gas volume would have remained constant and have been equal to the initial volume of gas inside the system (introduced during initial filling). This was not the case though, as the o-rings as well as the tubing exhibited pressure-related expansion. This was easily measured and was explained by the following equation:

$$V(t) = V_o + k_e(P(t) - P_o), \text{ (equation 2)}$$

where V(t) is the volume, V_o is the initial gas volume, k_e is the volume expansion coefficient, P(t) is the internal pump pressure, and P_o is the initial/ambient pressure. k_e was experimentally determined to be 0.50 μL/bar. This value was attained by applying a pressure to the pump chamber via the pump outlet. The displacement of the air-water interface in the solvent reservoir gave a measurement of the volume expansion. The linear response of the volume expansion was confirmed to be accurate to > 70 bar. V_o varied from one filling to another and needed to be experimentally determined.

Next, the sources of gas generation and gas loss were examined. The only source of gas generation was electrolysis and, due to basic electrochemical principles, the gas generation rate was known to be directly proportional to the applied electrolysis current. Ideally, for every four electrons passing through the electrodes, three gas molecules were generated (two H_2 and one O_2), but in reality not all the current was converted to gas. This was due to molecules in the solution that oxidized or reduced more readily than

water. The efficiency that electrons are converted into the desired byproducts (in this case H_2 and O_2) is known as the faradaic efficiency. In our situation, there were several reactions that could reduce the efficiency. For example, the formate ion is known to be oxidized, particularly in the presence of a catalytic electrode like Pt. Also, with Pt electrodes, it is known that H_2 can be oxidized and O_2 be reduced[64, 65] via the following half reactions:

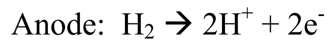

$$\text{Anode: } H_2 \rightarrow 2H^+ + 2e^-$$

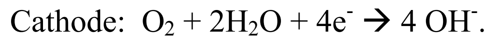

$$\text{Cathode: } O_2 + 2H_2O + 4e^- \rightarrow 4\,OH^-.$$

The oxidation of H_2 and reduction of O_2 are known to significantly decrease the faradaic efficiency, especially when the anode and cathode are in close proximity to each other[64], as was the case here. While technically not recombination, the replacement of either of the standard water electrolysis half reactions with the corresponding half reaction above has the same net effect as recombination (e.g., $2H_2 + O_2 \rightarrow 2H_2O$). Overall, the gas generation rate could be expressed as follows:

$$\frac{dn(t)^+}{dt} = \frac{3\varepsilon I}{4q_e N_a}, \text{ (equation 3)}$$

where $dn(t)^+/dt$ is the molar gas generation rate, ε is the faradaic efficiency, I is the current, q_e is the charge of an electron and N_a is Avogadro's number. Gas loss on the other hand was possible via permeation of gas out of the electrolysis chamber and also through the recombination of H_2 and O_2 at the catalytic Pt electrode surface. Gas loss through permeation is well known to be directly proportional to the differential pressure. Likewise, the recombination of dissolved H_2 and O_2 was also expected to be proportional to pressure, as the higher the pressure, the higher the concentration of dissolved gas in the liquid. These two factors could be lumped together and be expressed as follows:

$$\frac{dn(t)^{-}}{dt} = k_l(P(t) - P_o)\text{, (equation 4)}$$

where $dn(t)^{-}/dt$ is the molar gas loss rate, k_l is the gas loss coefficient, P(t) is the internal pump pressure, and P_o is the ambient pressure. The net molar gas change inside the chamber was simply a sum of the gas generation and gas loss terms (equation 3 and 4), with the total molar gas amount expressed as an integral as follows:

$$n(t) = \int_o^t \left(\frac{dn(T)^{+}}{dT} - \frac{dn(T)^{-}}{dT} \right) dT\text{, (equation 5)}$$

where n(t) is the total molar gas amount. n_o, the initial molar amount of gas in the chamber, was experimentally determined along with V_o. The determination of these initial values will be addressed later.

One final factor that needed to be accounted for was the solubility of the gas in liquid. Using a weighted average, the average combined H_2/O_2 solubility is 9.4×10^{-4} mol/(L-bar). The ideal gas law needed to be modified since only H_2/O_2 in the gas phase contributed to the pressure. The total molar gas amount could be split up as into a gaseous component and also a dissolved component as follows:

$$n(t) = n(t)_{gas} + n(t)_{dissolved} = n(t)_{gas} + k_s P(t) V_t\text{, (equation 6)}$$

where n(t) is the total molar gas amount, $n(t)_{gas}$ is the molar gas amount in the gaseous phase, $n(t)_{dissolved}$ is the molar gas amount in the dissolved phase, k_s is the average solubility constant, P(t) is the pressure inside the electrolysis chamber, and V_t is the total volume of the electrolysis chamber. This assumed that the liquid was always saturated with dissolved gas, which was reasonable given that there were already gas bubbles present in the solution. Combining equations 1–6 gave the following governing equation:

$$P(t)\left[V_o + k_e(P(t) - P_o)\right] = \left[\int_o^t \left(\frac{3\varepsilon I}{4q_e N_a} - \left(k_l(P(T) - P_o)\right)\right)dT - k_s P(t) V_t\right] RT \text{, (equation 7)}$$

where P(t) is the only unknown. This quasi steady-state model was solved using an initial condition of $P(0)=P_o$. V_o and n_o were determined experimentally. The faradaic efficiency (ε) and gas loss coefficient (k_l) were used as fitting parameters. Figure 4-5 shows the results of the model when compared with the experimental results. A faradaic efficiency of 54.4% and a molar gas loss coefficient of 1.1×10^{-8} moles/(min-bar) were used.

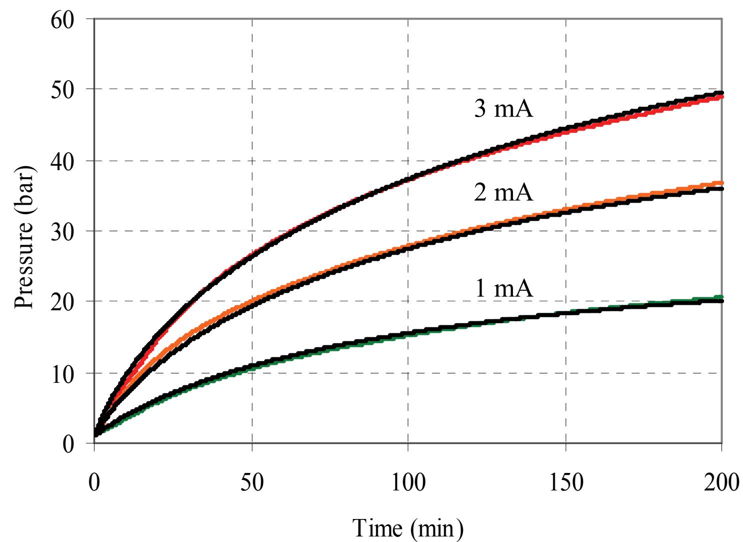

Figure 4-5: Comparison between mathematical model and actual data (Figure 4-4). The model results are shown in the solid black lines.

One challenging aspect of fitting this mathematical model was in the experimental determination of the initial gas volume (V_o). The mathematical model was very sensitive to the initial gas volume, particularly in the early stages of pressure increase. It was difficult to control the initial gas volume inside the chamber during filling and visually, it was very difficult to estimate. The initial volume was determined after the experiment

was completed. Post-experiment, the outlet valve was opened and the pressure released for a short period of time. The liquid that came out was collected and the volume measured. The amount of ejected liquid along with the associated pressure loss could be used to back calculate the initial gas volume as follows:

$$V_o = \frac{P_f \Delta V}{P_i - P_f} + k_e (P_o - P_i - P_f), \text{ (equation 8)}$$

where V_o is the initial gas volume, P_i is the pressure prior to pressure release, P_f is the pressure after pressure release, ΔV is the ejected fluid volume, k_e is the chamber volume expansion coefficient, and P_o is the initial/ambient gas pressure. In general, our filling method resulted in an initial gas volume of around 5–20 μL. V_o was also used to calculate n_o, the initial molar gas volume inside the chamber, using the ideal gas law.

The greatest advantage of devising this mathematical model was that it could be used to calculate the pressure versus flow versus current relationship of the pump when operated as a non-closed system. The complete knowledge of this three-way relationship was directly applicable to real pumping situations. Because we only wanted to know the steady-state, constant pressure flow rate, factors such as dissolved gas and volume expansion of the electrolysis chamber were not needed. In the steady-state, only the gas generation and gas loss needed to be considered. The flow rate achieved at a given pressure and current could be calculated as follows:

$$F = \left(\frac{dn(t)^+}{dt} - \frac{dn(t)^-}{dt} \right) \frac{RT}{P}, \text{ (equation 9)}$$

where F is the steady-state flow rate, R is the universal gas constant, T is the temperature, and P is the steady-state internal pump pressure. The expressions for $dn(t)^+/dt$ and $dn(t)^-$ /dt were previously described in equations 3 and 4. The fitting parameters found before

(ε = 54.4% and k_l=1.1x10^{-8} moles/(min-bar)) were used to calculate the flow/pressure/current relationship. The results can be found in Figure 4-6. This data could be used to estimate what currents were needed to drive the pump. For example, for a given fluidic load and desired flow rate, the corresponding backpressure could be calculated. The current corresponding to the desired flow rate and backpressure could then be read directly from Figure 4-6.

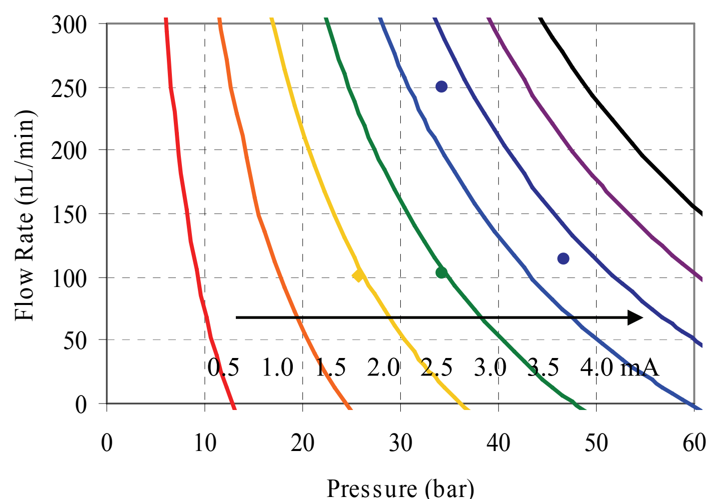

Figure 4-6: A plot showing the flow rate, pressure, and current relationship for the electrolysis pump. Also on the plot are single point calibrations to check the accuracy of the mathematical model. The discrete points are colored corresponding to the applied current.

To check the accuracy of the model, several discrete data points were collected. This was accomplished using the non-closed setup described in the experimental section. A backpressure was applied to the pump using a nitrogen gas cylinder and a constant current applied through the electrodes. The linear velocity of the water/air interface in the solvent reservoir was measured to determine the resulting flow rate. Four discrete

points were collected and are also plotted in Figure 4-6. Agreement with the mathematical model was good. Any discrepancy was likely caused by the system not being in equilibrium, as it was difficult to judge when the pump had finally stabilized. This was likely the reason why all the discrete points demonstrated a flow rate slightly below the one calculated using the mathematical model. This was also the reason why a non-closed system was not chosen for pump calibration. The need to test a large number of points and the long period of time needed to wait for the pump to stabilize would have made calibration inaccurate and time consuming. Testing the electrolysis in a closed system effectively allowed the calibration of the pump across a variety of flow rates, pressures, and currents with a few simple experiments.

Another key point that could be taken away from Figure 4-6 was the x-intercept of the various curves. These intercepts represented the point where the pressure was high enough that the gas generation rate was equal to gas loss rate. Therefore, they represented the maximum pressure that could be achieved with this pump at a given current. This is important because for most pumping applications there is not only a need to increase, but also to decrease the pressure as necessary (e.g., if you want to lower the flow rate). The intercepts could be used to determine how far the current needed to be lowered to induce a pressure loss.

One important figure of merit for these pumps was the efficiency. Efficiency could be defined in multiple ways. One way to define efficiency was to compare the actual flow rate with the expected flow rate for a particular current assuming 100% faradaic efficiency. This was termed the molecular efficiency and was calculated as follows:

$$\varepsilon_{molecular} = \frac{F}{F_{ideal}} = \frac{F}{\left(\frac{3IRT}{4q_e N_a P}\right)}, \text{ (equation 10)}$$

where F is the steady-state flow rate, I is the current, R is the ideal gas constant, T is the temperature, q_e is the charge of en electron, N_a is Avogadro's number, and P is the steady-state internal pump pressure. Figure 4-7 shows a plot of the molecular efficiency as a function of pressure and current. As expected, at a pressure of 1 bar, the molecular efficiency was a maximum and had a value equal to the actual faradaic efficiency (ε = 54.4%). As the pressure increased, the efficiency dropped as the gas loss rate increased.

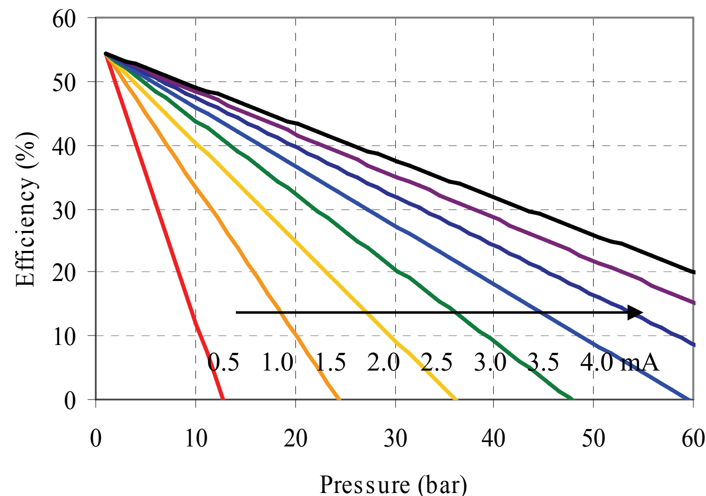

Figure 4-7: Plot of molecular efficiency as a function of pressure and current. Each of the curves corresponds to a different applied electrolysis current.

Another measure of efficiency that was worth examining was the power efficiency. This compared the amount of power dissipated by the pump versus the total work done by the gas in the electrolysis chamber. To determine this, first the I-V relationship for our electrochemical cell had to be measured. This is shown in Figure 4-8. At low currents, the voltage was near 1.7 V, the expected minimum voltage.

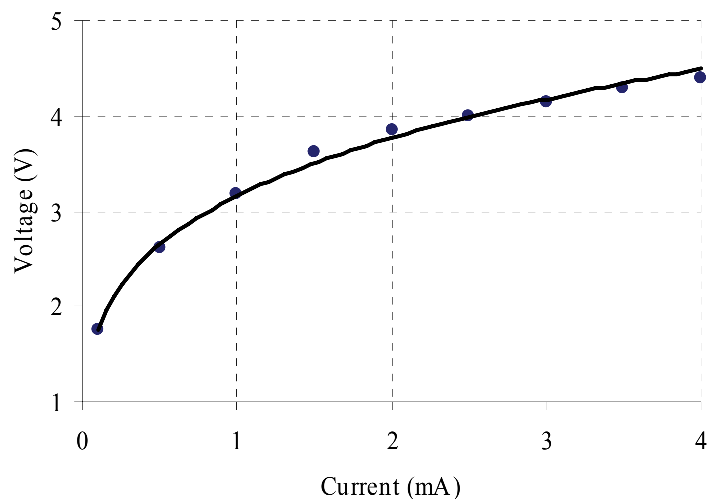

Figure 4-8: I-V curve for the electrolysis device

The power efficiency of the pump could then be calculated using the following equation:

$$\varepsilon_{power} = \frac{PF}{IV}, \text{ (equation 11)}$$

where P is the steady-state pressure in the pump, F is the steady-state flow rate, I is the applied current, and V is the voltage drop across the electrochemical cell. Combining the data in Figure 4-6 and Figure 4-8 , this power efficiency could be calculated. The results are shown in Figure 4-9. At low pressures, low currents had the best efficiency, reaching nearly 0.4%. As the pressure increased, the higher currents eventually become the most power efficient. This was expected since at high pressures the gas loss rate became higher and higher, reducing a greater portion of the flow rate at low currents. In HPLC, where the pressure is nearly always > 40 bar, higher currents were the most efficient.

The theoretical maximum power efficiency could be calculated by assuming a 100% faradaic efficiency and lowest possible driving voltage (e.g., 1.7 V for Pt electrodes). This calculation yielded a maximum power efficiency of 1.1%. Low power

efficiency was expected since a vast majority of the power went into the stored energy potential in H_2 and O_2.

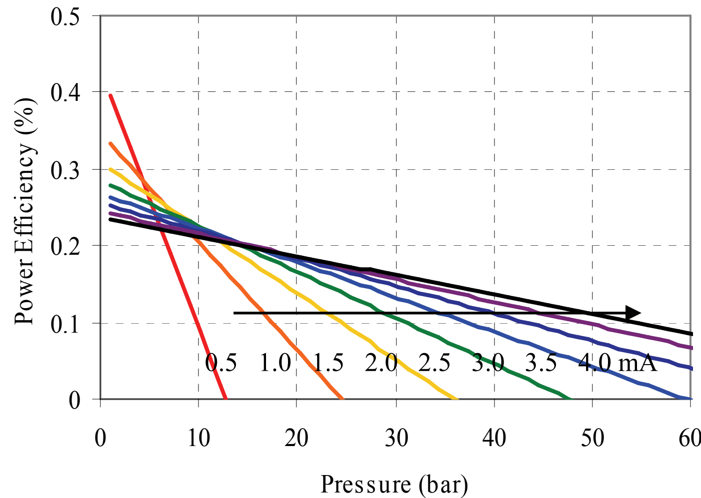

Figure 4-9: Plot showing the power efficiency of the electrolysis pump at various pressures and currents

One final important issue concerning the pump was the time response. Because this pump relied on the build up and release of pressure to deliver varying flow rates, the response time was slow, particularly at high operating pressures. This was evident from Figure 4-4. In fact, the data in Figure 4-4 represented the maximum pressure ramp rates because there was no pressure loss due to any liquid flow from the pump. Pressure release was also slow as no method to actively vent the gas was implemented. The response time of the pump had a strong dependence on the gas volume inside the electrolysis chamber. Changing the pump pressure when there was a large evolved gas volume in the electrolysis chamber took much longer than when the gas volume was small. These difficulties in controlling the pump necessitated the use of sensors for feedback-based control. This was especially the case when the transient performance of

the pump needed to be carefully regulated, as it does in HPLC. The integration of these high-pressure pumps into a closed-loop feedback control system is discussed in Chapter 6.

4.4. Conclusion

A high-pressure electrolysis-based pump was designed and characterized. Even at flow rates consistent with nanoscale HPLC (e.g., 150 nL/min at a pressure of 40 bar) power consumption was still < 15 mW. While all the data presented was for 100% water (0.1% formic acid) solutions, reverse-phase HPLC also requires the pump to deliver fluids with higher organic compositions, up to a maximum of roughly 50%. Characterization of the pump was also conducted at these higher organic compositions. There was not a significant difference in the pump performance other than the need for a higher driving voltage. This was expected because neither the faradaic efficiency nor the gas loss coefficient were expected to change significantly with the change in electrolyte. In general, for identical electrolysis currents, a 60% acetonitrile electrolyte needed twice the voltage of a 100% water electrolyte. This equated to a doubling in the power consumption.

There are still several possible improvements that can be made to the pump. For example, the use of HPLC mobile phases for the electrolyte is non-ideal. A specialized, strong electrolyte consisting of H_2SO_4 or Na_2SO_4 would be able to reduce the power consumption drastically, perhaps by as much as a factor of two. The use of a special electrolyte would require the implementation of a flexible barrier to separate the electrolyte and the mobile phase though. Another possible improvement is in developing methods to separate the produced O_2 and H_2. This would most likely enable faradaic

efficiencies of close to 100%, a 2x improvement over what it is now. This would once again reduce the overall power consumption.

There are several possible ways of improving the pump time response. A mechanism that allows the pump to selectively recombine O_2 and H_2 would probably allow better control of the pump. An improvement in the transient response of the pump can also be made by using a smaller and/or less flexible electrolysis chamber. Both these changes would mean that less gas would need to be generated to increase the pressure, with the opposite being true for decreasing the pressure. This comes at the cost of pressure stability, though. Smaller chambers are much more prone to pressure fluctuations than larger ones. In an application such as HPLC, where stability is important and fast transient response is rarely needed, a large electrolysis chamber is probably preferred.

Chapter 5: Multi-Function Microfluidic Platform for Liquid Chromatography Tandem Mass Spectrometry (LC-MS/MS)

5.1. Introduction

High-performance liquid chromatography tandem mass spectrometry (HPLC/MS-MS) is recognized as one of the most powerful analytical techniques available and is widely used in the biological sciences. One of the most important applications of HPLC-MS/MS is in the field of proteomics. The ability to separate and identify the components in a highly complicated mixture makes HPLC-MS/MS the preferred tool for a large number of proteomic studies[66]. Instead of analyzing the proteins directly, it is common to homogenize the mixture by performing an enzymatic digestion of the protein mixture. Trypsin, which cleaves peptides at the carboxyl side of the amino acids Lys and Arg, is often used as the digestion enzyme. The protein mixture is thus converted into a peptide mixture, which is more suitable for HPLC/MS-MS analysis.

The coupling of HPLC and MS can be accomplished in one of two ways: electrospray ionization (ESI) and matrix-assisted laser desorption/ionization (MALDI)[66]. In this work ESI is used. It is an on-line approach meaning that the detection is done concurrently with the separation. In ESI, a microscopic nozzle is used to create a fine spray. The formation of this spray is in part facilitated by the establishment of a high potential difference between the nozzle and the mass spectrometer opening. As the

droplets travel towards the mass spectrometer inlet, via coloumbic attraction, the solvent evaporates, creating smaller and smaller drops. This forces the analyte ions closer and closer together until the electrostatic repulsion of the ions overcomes the surface tension of the liquid drop and causes the drop to break down into even finer ones. This process of coloumbic fission continues until there are only lone analyte ions entering the mass spectrometer, where their m/z ratio is measured. Tandem MS, where selected ions are collected and further disassociated inside the mass spectrometer, is often used. The information gathered about the primary and secondary (fragment) ions can be used to determine the original peptide sequences. The peptide sequences detected in the mixture can then be compared to databases to see which proteins originally were in the sample[67, 68].

The high-resolution and high-sensitivity separation of peptides is generally done through nanoscale reverse-phase HPLC, where a hydrophobic stationary phase, such as C_8 or C_{18}, is used. Peptides exhibit a wide range of hydrophobicities, making isocratic elutions unsuitable. An isocratic separation conducted at an acetonitrile percentage high enough to elute the most hydrophobic peptide would result in extremely poor separation of the less hydrophobic ones. Gradient elutions, where the eluent composition is varied throughout the separation, are typically used instead. For example, a typical gradient might ramp linearly from 0 to 50% acetonitrile at a rate of 1%/min while maintaining a constant flow rate of 150 nL/min. This gradient causes the peptides to elute off the column in order of increasing hydrophobicity. The flow control systems used to generate gradient elutions are inherently more complicated than those for isocratic elutions. This is further complicated by the low flow rates and high pressure requirements. As a result,

HPLC systems are generally extremely expensive and complicated to operate. The work presented in this chapter aims to simplify the overall separation system by integrating the majority of HPLC components on a single microfluidic chip. This not only could lead to lower cost analyses, but also a miniaturized separation platform.

To date, most of the work done on miniaturized separation devices has been focused on electrically driven separations[69-71]. The development of miniaturized HPLC systems began with the development of on-chip columns interfaced with conventional HPLC hardware[72]. It is only relatively recently that more advanced microfluidic HPLC systems have been developed[31, 72-76], with the trend being towards more highly integrated devices. One important distinction of the chip presented in this chapter is the integration of sensors. These sensors were used to not only passively monitor the fluid flow, but also used as feedback for controlling the pumping.

5.2. Experimental

5.2.1. Chip Design

The presented chip included the following components: a passive mixer for producing the binary solvent mixtures; an electrochemical time-of-flight (TOF) flow sensor for flow rate measurements; an impedance-based composition sensor to measure the organic solvent percentage in the eluent; analytical and trap columns for separation and enrichment; weir-type filters for retaining the beads in the columns; and a polymer electrospray nozzle for MS detection. The mixer and sensors were previously discussed in detail in Chapter 3. A picture of the device can be found in Figure 5-1.

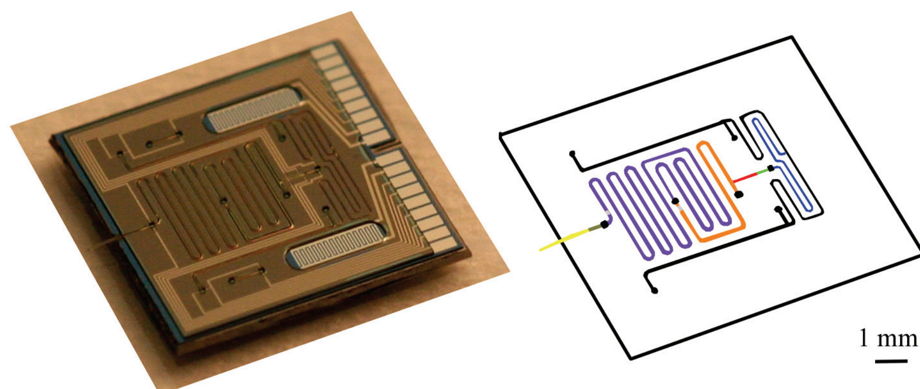

Figure 5-1: A picture and diagram of the presented chip. The various components are highlighted in blue (mixer), green (composition sensor), red (flow sensor), orange (trap column), purple (analytical column), brown (electrodes for applying electrospray potential), yellow (electrospray nozzle), and gray (bead filters). The black dots represent the location of fluidic ports. Overall chip size was 9.8 x 9.8 mm^2.

Images of all the individual devices on the chip can be found in Figure 5-2. The passive mixer consisted of a 30 x 25 (W x H) μm^2 in cross section and 8.8-mm-long channel. The small cross section was designed to bring the two incoming flows in close contact and reduce the distance molecules had to diffuse for complete mixing. The composition sensor consisted of a set of interdigitated electrodes with a width/spacing of 7.5 µm. The electrodes covered a total area of 70 x 300 (W x L) μm^2 and were located in a channel with a cross section of 80 x 25 (W x H) μm^2. A measurement of the impedance of the fluid was used to deduce the water/acetonitrile ratio. For the flow sensor, the electrodes used to generate the electrochemical pulse had a spacing of 100 µm and the detector electrodes were located 450 µm downstream. The flow sensor channel dimensions were 80 x 3.5 (W x H) μm^2. The time it took for the electrochemical pulse to travel from the pulsing electrodes to the detector electrodes was used to measure the

linear fluid velocity, which could then be converted to a volumetric flow rate. The analytical column had a cross section of 80 x 25 (W x H) μm^2 with a total length of 4.2 cm. The trap column on the other hand had a slightly larger cross section of 120 x 25 (W x H) μm^2, but was much shorter, with a total length of only 0.9 cm. The bead filters were constructed by using a step in the channel height. The filter height was around 3.5 µm, which prevented any particles larger than that from passing through. The electrodes used to establish the electrospray potential were identical in design to those used to measure the fluid composition. The electrospray nozzle consisted of a freestanding Parylene channel, which extended 0.9 cm past the edge of the chip. The end of the nozzle terminated in a triangular nib with a terminal radius of roughly 1–2 µm. Finally, the fluidic inlet/outlet ports were defined in SU-8 and were 200 x 200 (W x L) μm^2.

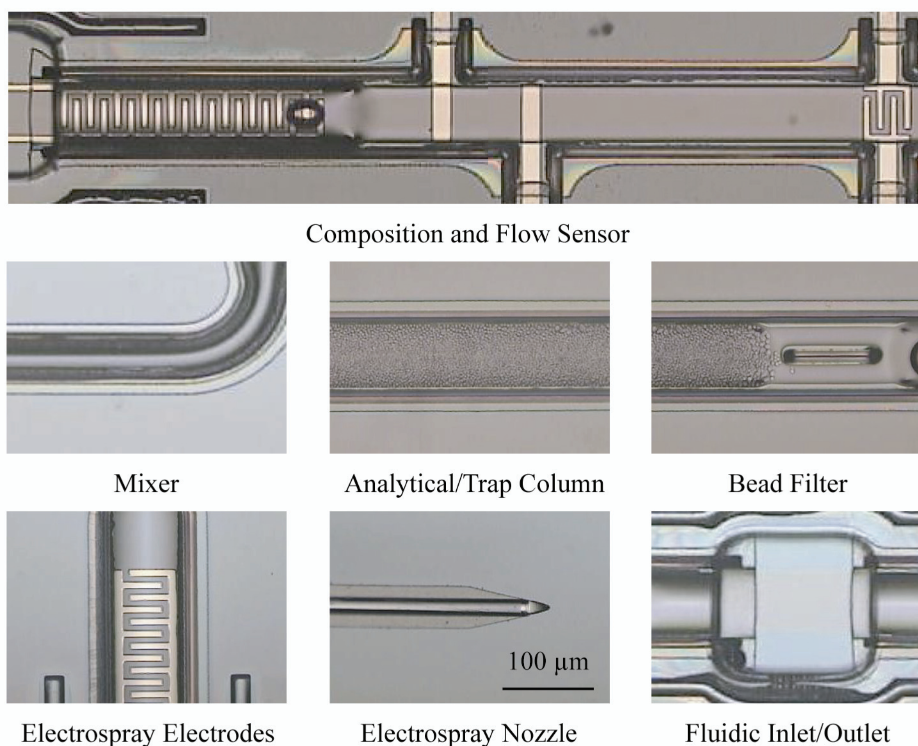

Figure 5-2: Close-up pictures of all the individual components on the presented chip. All devices are shown at the same scale.

The chip was designed such that the different components could be bypassed and/or turned off as needed. This, combined with the ability to selectively access and close off the many different fluidic ports on the chip, allowed this single chip to be operated in many different separation configurations. A summary of the configurations and the components they used is as follows:

1. **Standard Column with Active Sensors**: The chip was used as a nanobore format column with the benefit of integrated sensors for eluent monitoring. In this setup, the sensors, analytical column, and electrospray nozzle were used with conventional HPLC hardware to perform separations.
2. **Vented Column with Non-Active Sensors**: The chip was used as a nanobore format column with an integrated vented trap column for sample loading and enrichment. In this setup, the trap column, analytical column, and electrospray nozzle were once again used with conventional HPLC hardware to perform separations.
3. **Standard Column with On-Chip Feedback Flow Control**: The chip was used as a nanobore format column with the addition of an on-chip mixer and sensors for feedback-controlled on-chip gradient generation. In this setup, the mixer, sensors, analytical column, and electrospray nozzle were all used. Instead of using a conventional HPLC pump, a custom-built two-channel pneumatic pump was used to drive the flow.

The setups and experimental procedures for each of these configurations will be described in detail later in the chapter.

5.2.2. Chip Fabrication

The technology used to fabricate this chip was described in detail in Chapter 2. These chips utilized the high-pressure anchoring technology and SU-8-based fluidic ports outlined in Chapter 2. The process is diagrammed in Figure 5-3 and can be broken down into eleven steps.

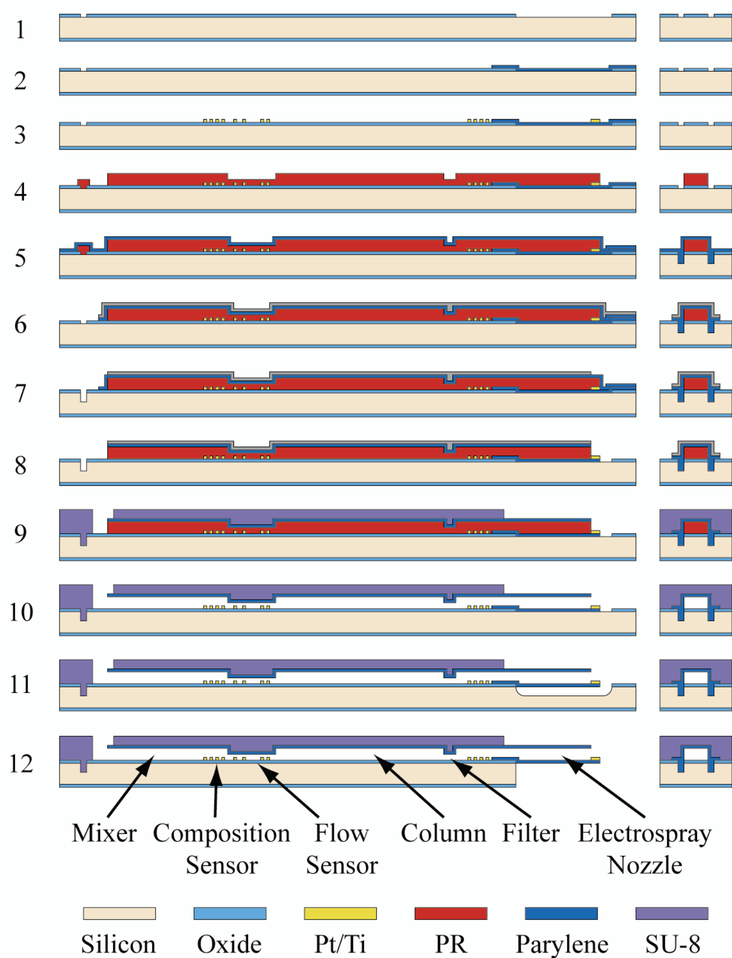

Figure 5-3: Process flow for the presented chip. The left-hand column shows a cross-sectional view where the liquid flow is from left to right. The right-hand column shows a cross-sectional view where the liquid flow is into the page.

1. Silicon Oxide Deposition and Patterning: A 4000 Å silicon oxide (SiO_x) layer was grown on a silicon wafer. Next, a 5 µm AZ1518 photoresist layer was spun on the wafer and patterned using photolithography. The exposed silicon oxide was then etched using a buffered HF solution. Afterwards, the photoresist was stripped using acetone and isopropyl alcohol. The oxide layer served three functions: first, as an insulation layer between the electrodes and the silicon wafer; second, as a mask for DRIE etching (see step 5); and third, as a mask for XeF_2 silicon during the undercutting of the electrospray nozzle (step 11).

2. Parylene Deposition and Patterning: After treating the wafer surface with A-174 adhesion promoter, a 5 µm Parylene layer was deposited. Patterning of this layer was accomplished using oxygen plasma with a photo-patterned 10 µm AZ 4620 photoresist layer as a mask. This layer would eventually form the base of the electrospray nozzle. After etching, the remaining photoresist was stripped using acetone and isopropyl alcohol.

3. Metal Deposition and Patterning: A 3 µm composite lift-off photoresist layer made up of LOR3B and AZ1518 was deposited and photo-patterned. The use of LOR3B as the base layer created a re-entrant profile ideal for lift-off. A 200/2000 Å Ti/Pt layer was then deposited via e-beam deposition. The Ti was used to improve adhesion between the Pt and the oxide surface. After metal deposition, liftoff was accomplished by dissolving the photoresists using ST-22 photoresist stripper. The resulting metal layer was used to define all the electrodes, as well as the metal lines and pads needed for electrical connections.

4. Sacrificial Photoresist: A 25 µm AZ4620 photoresist layer was spun on the wafer. By using two exposures, one full, and one partial, a bi-level (25 µm/3.5 µm), monolithic

photoresist structure was produced. A bi-level sacrificial layer was necessary to reduce the channel height where the flow sensor and filters were located. This sacrificial photoresist layer was temporarily used to define the channel and would eventually be dissolved away (step 10).

5. Parylene Anchors and Deposition: A deep reactive ion etcher (DRIE) was used to etch 40-µm-deep trenches on the sides of the channels. The oxide, patterned in step 1, was used as a mask for DRIE etching. Afterwards, a 10 µm Parylene-C layer was deposited. The DRIE trenches took advantage of the conformal nature of the Parylene deposition and served to anchor the Parylene layer to the substrate. By mechanically anchoring the encapsulating layer, much higher pressures could be sustained by the channels.

6. Parylene Patterning: A 200/2000-Å-thick Cr/Au layer was e-beam deposited and patterned by using a 40 µm AZ4620 photoresist mask. The metal was etched using Au etchant type TFA (KI-based) and CR-7 Cr etchant (perchloric-acid-based). After metal etching, the photoresist was stripped using acetone and isopropyl alcohol. The Cr/Au metal layer was then used as an etch mask for Parylene patterning, which was accomplished using an oxygen plasma. This patterning was used to remove Parylene over the areas where the SU-8 anchors would be etched (step 7).

7. SU-8 Anchors: Before the formation of the SU-8 anchors, the Cr/Au layer was patterned again using the same process outlined in step 6. Then, a 40-µm-thick AZ4620 photoresist layer was spun and patterned. This formed a mask to DRIE etch shallow 30 µm trenches near the SU-8 edges. The photoresist was stripped using acetone and isopropyl alcohol.

8. Parylene Patterning: The Parylene was etched in oxygen plasma using the Cr/Au mask patterned in step 7. This etch step opened all the ends of the microchannels and the electrospray nozzle opening. After Parylene etching, the metal mask was stripped using Au etchant and Cr-7 Cr etchant.

9. SU-8 Encapsulation: A 50-μm-thick SU-8 layer was spun on the wafer and patterned. This SU-8 layer filled the trenches (step 7), which helped improve SU-8 adhesion to the substrate. This was especially critical, as the entire chip would be soaked in harsh organic solvents later in the process (step 10). The SU-8 also helped to strengthen the channels further so they could withstand the high operating pressures. Finally, the SU-8 also sealed the regions where the electrodes crossed into the channel, preventing these areas from leaking during high-pressure operation.

10. Photoresist Dissolution: The sacrificial photoresist was dissolved using acetone over a period of 1 week, after which the channels were individually flushed with fresh acetone. The wafer was then rinsed in isopropyl alcohol and water before drying.

11. XeF_2 Etching: To make the electrospray nozzle freestanding, XeF_2, a gas-phase isotropic silicon etchant was used to remove the silicon underneath the nozzle. Simultaneously, this etch step was used to etch trenches along all the lines where the individual chips were to be separated. XeF_2 has nearly an infinite etch ratio between SiO_x and Si, and the oxide patterned in step 1 was used to constrain the silicon etching to underneath the nozzle and along chip edges. Using the trenches as a guide, the wafer was manually scribed and separated into individual dies.

5.2.3. Chip Packaging / Preparation

The packaging of this chip was identical to the chips described in Chapter 3. Multiple manifolds with various numbers of openings were used in the testing of this device. Single, dual, and triple inlet manifolds were used in our separation experiments depending on the particular configuration. When the chip was fitted with these manifolds, any of the on-chip fluidic ports that did not match up with a corresponding port in the manifold was effectively sealed off.

Before the chip could be tested, the analytical column, and in some cases the trap column, were packed with beads. This was accomplished by using a single inlet manifold. By positioning the manifold over the correct port while simultaneously blocking all other ports (except for the column outlet) the columns could be individually packed with the desired support, generally 3 or 5 μm C_{18} support (Varian, Inc. or Grace Vydac). Columns were packed by forcing a bead/isopropyl alcohol slurry mixture into the column at pressures up to 100 bar. A pressure bomb with magnetic stirrer was used to hold the slurry and keep the beads in suspension during packing.

5.2.4. Sensor Operation

The operation of the sensors was previously described in Chapter 3. The sensors on this device were identical to the sensors on the integrated device discussed there.

5.2.5. Pneumatic Pump

For feedback-controlled separations a custom-built two-channel pump was used. A conventional HPLC pump could not be used because they do not allow for the control

of the individual pump channels. The pump was a pressure-driven setup with two separate, but identically built channels, both powered by a common 45 bar nitrogen gas cylinder. Each channel consisted of a Model 3110, 0–40 bar electrically controlled pressure regulator (March-Bellofram) that directly controlled the pressure inside of a 1 mL solvent loop. Solvent loops were constructed using Teflon FEP tubing (Upchurch Scientific). A 40 mL gas sample chamber (Swagelok) was placed in between the regulator and liquid reservoir to reduce pressure fluctuations. The solvent loops were connected to 360 μm OD fused silica tubing (10–15 μm ID) (Polymicro Technologies) that could then be connected to the actual chip. For all our experiments, the pumps were loaded with degassed 100/0/0.1 and 40/60/0.1 (water/acetonitrile/formic acid) solutions. A photograph of the pump can be found in Figure 5-4.

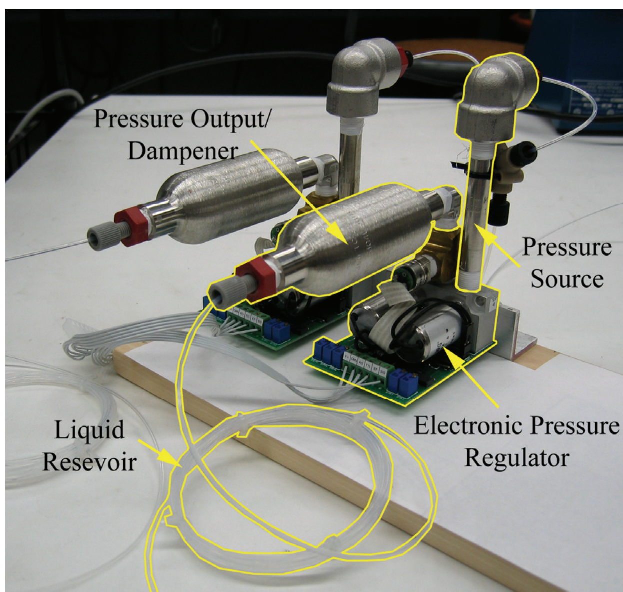

Figure 5-4: A picture of the custom-built two-channel pneumatic pump

5.2.6. Mass Spectrometry

All MS analyses were performed using an Agilent 1100 series LC-MSD SL ion trap mass spectrometer. The packaged chip was positioned in front of the mass

spectrometer on an axis orthogonal to the mass spectrometer inlet. The chip was attached to a 3-axis stage and the chip was manually positioned for optimal electrospray. Electrodes on the chip located between the end of the analytical column and the electrospray nozzle were grounded. The voltage setting was -1900 V for the mass spectrometer inlet and -1400 V for the counter electrode. Both full range mass spectra and MS/MS spectra were collected. A picture of the chip interfaced to the mass spectrometer can be found in Figure 5-5 .

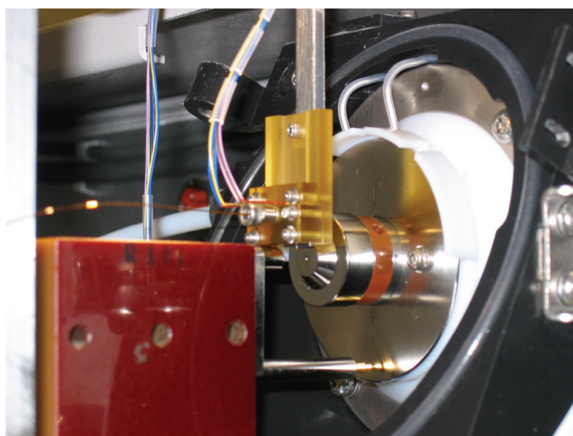

Figure 5-5: A picture of the chip/mass spectrometer interfacing

5.2.7. Data Acquisition

In the configurations where the sensors were active, the sensors were controlled and monitored using a DAQPad-6020E data acquisition unit (National Instruments) in conjunction with LabVIEW (National Instruments). Flow rate measurements were conducted at a frequency of 0.1 Hz and composition measurements at 1 Hz. Control of the custom-built pneumatic pump and the feedback algorithms used to control it were also implemented in LabVIEW. Feedback was implemented by using a proportional feedback algorithm. The pump control voltages were updated at 1 Hz. The conventional HPLC hardware, which included the Agilent 1100 series nanoflow pump, isocratic pump,

micro well-plate autosampler, and mass spectrometer, was controlled using the manufacturer's software.

5.2.8. Chip Separation Configurations

5.2.8.1. Standard Column with Active Sensors

The first separation configuration used the single inlet manifold. An Agilent 1100 series nanoflow pump was connected to our chip via a single open port. An Agilent 1100 series micro-well-plate autosampler was placed in-line between the pump and chip for automated sample metering. A diagram of the setup can be found in Figure 5-6.

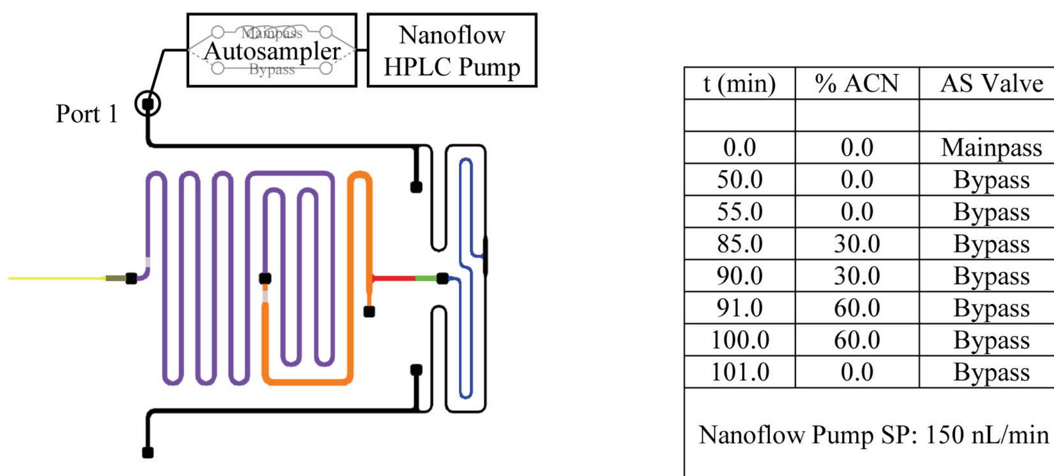

t (min)	% ACN	AS Valve
0.0	0.0	Mainpass
50.0	0.0	Bypass
55.0	0.0	Bypass
85.0	30.0	Bypass
90.0	30.0	Bypass
91.0	60.0	Bypass
100.0	60.0	Bypass
101.0	0.0	Bypass
Nanoflow Pump SP: 150 nL/min		

Figure 5-6: Fluidic configuration and separation method for the "Standard Column with Active Sensors" configuration

The analytical column was packed with 5 µm C_{18} support (Grace Vydac) to a length of approximately 3 cm. To begin, a sample was injected directly onto the analytical column using a 100/0/0.1 (water/acetonitrile/formic acid) solution at setpoint

flow rate of 150 nL/min. After the sample was loaded, the autosampler's internal sample loop was bypassed and a pre-programmed gradient elution was delivered by the nanoflow LC pump. The autosampler's sample loop was bypassed during the delivery of the gradient to reduce delay. The gradient ramped linearly from 0 to 30% acetonitrile at a rate of 1%/min and at a constant setpoint flow rate of 150 nL/min. The sensors monitored the flow rate and fluid composition flowing into the column in real time. Only a single flow path existed throughout the separation. The liquid entered the chip at port 1, and was directed through the mixer, sensors, trap column, analytical column, and electrospray nozzle, in that order. The mixer and trap column served no purpose except to direct the flow. This setup was designed to mimic the application of a nanobore format column with the added benefit of having sensors to monitor the eluent.

5.2.8.2. Vented Column with Non-Active Sensors

In the second configuration, both the chip's trap column and analytical column were packed using 3 µm C_{18} support (Varian, Inc.). The trap column had a total length of 0.8 cm and the analytical column was 3 cm long. The trap column was interfaced to an Agilent 1100 series micro-well-plate autosampler/isocratic pump combination for sample loading. The chip was also interfaced to an Agilent 1100 series nanoflow pump for gradient delivery. A diagram of the setup can be found in Figure 5-7.

To begin, the autosampler /isocratic pump was used to pump the sample through the trap column at a flow rate of 1 µL/min using a 100/0/0.1 (water/acetonitrile/formic acid) solution. During this stage of the separation, flow from the autosampler entered through port 3, was directed through the trap column, and out through port 2. Simultaneously, the flow entering the chip at port 1 also exited out through port 2. After

sample loading and desalting was complete, the internal autosampler valve was switched, automatically blocking off both the trap column inlet and outlet ports (ports 2 and 3). The Agilent 1100 series nanoflow pump was then used to deliver a linear 0 to 50% acetonitrile gradient at a ramp rate of 1%/min and a constant setpoint flow rate of 150 nL/min. The gradient entered through port 1 and traversed the mixer, sensors, trap column, analytical column, and electrospray nozzle, in that order. The mixer and sensors served no purpose other than providing a flow path. During this step, the sample was eluted off the trap column and onto the analytical column and separated. Sensors were not active in this configuration, though they could have been used to monitor the eluent flow in much the same way they were used in the "Standard Column with Active Sensors" configuration. The overall separation setup is similar to the vented column approach described in literature[77].

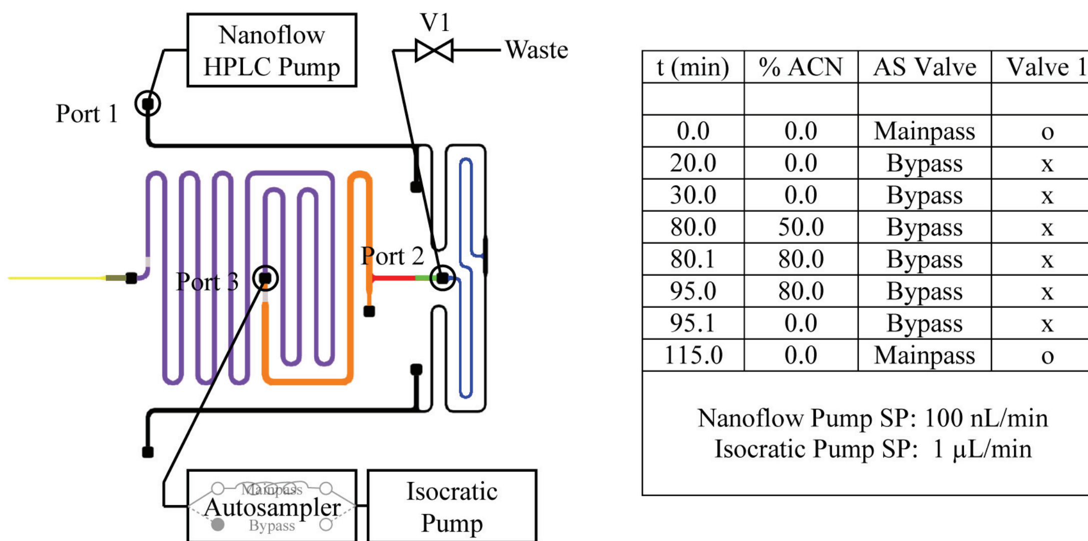

t (min)	% ACN	AS Valve	Valve 1
0.0	0.0	Mainpass	o
20.0	0.0	Bypass	x
30.0	0.0	Bypass	x
80.0	50.0	Bypass	x
80.1	80.0	Bypass	x
95.0	80.0	Bypass	x
95.1	0.0	Bypass	x
115.0	0.0	Mainpass	o

Nanoflow Pump SP: 100 nL/min
Isocratic Pump SP: 1 µL/min

Figure 5-7: Fluidic configuration and separation method for the "Vented Column with Non-Active Sensors" configuration. V1 is internal to the autosampler but is shown separately for clarity.

5.2.8.3. Standard Column with On-Chip Feedback-Controlled Flow Control

The third configuration utilized the integrated sensors for feedback-controlled operation. The custom-built two-channel pneumatically driven pump was used along with our dual-input fluidic manifold. The two solvent loops were loaded with 100/0/0.1 (water/acetonitrile/formic acid), designated channel A, and 40/60/0.1, designated channel B. In this configuration, an Agilent 1100 series micro-well-plate autosampler was placed in line between pump channel A and the chip. Valves (Upchurch Scientific) were also positioned on each of the pump channels for situations where we wanted only channel A or channel B to be active. The analytical column was packed with 5 µm C_{18} support (Grace Vydac) to a length of 3 cm. A diagram can be found in Figure 5-8.

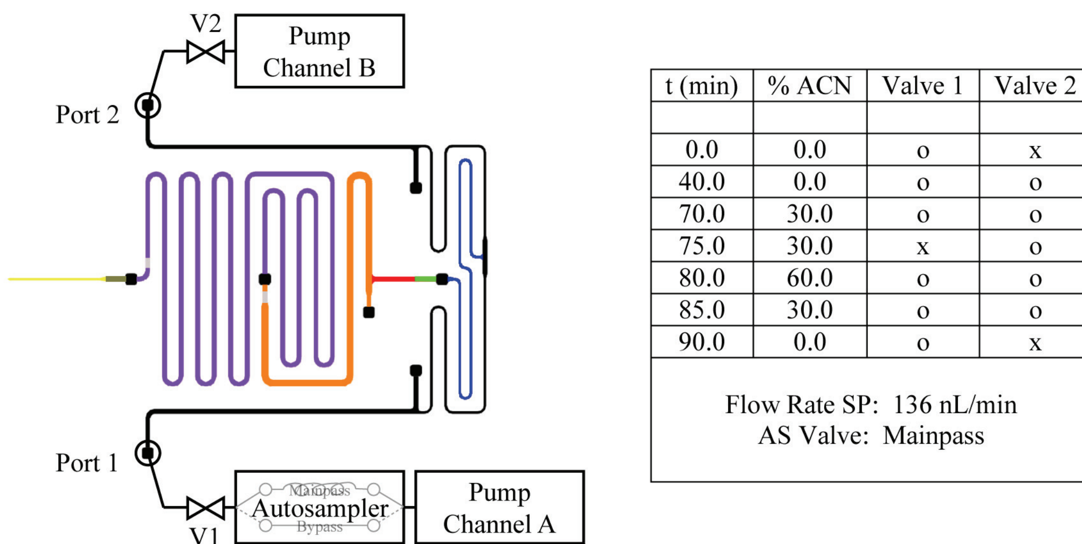

t (min)	% ACN	Valve 1	Valve 2
0.0	0.0	o	x
40.0	0.0	o	o
70.0	30.0	o	o
75.0	30.0	x	o
80.0	60.0	o	o
85.0	30.0	o	o
90.0	0.0	o	x

Flow Rate SP: 136 nL/min
AS Valve: Mainpass

Figure 5-8: Fluidic configuration and separation method for the "Standard Column with On-Chip Feedback-Controlled Flow Control" configuration

To begin, pump channel A was used to pump the sample directly onto the analytical column at a flow rate of 136 nL/min. During sample loading, valve 2 was

closed and flow entering through port 1 was directed through the mixer, sensors, trap column, analytical column, and electrospray nozzle, in that order. Once sample loading was complete, valve 2 was opened and pump channel B activated to produce a linear gradient from 0 to 30% acetonitrile at a rate of 1%/min and at a constant flow rate of 136 nL/min. During the gradient elution, liquids entered through ports 1 and 2 simultaneously and were directed through the mixer, sensors, trap column, analytical column, and electrospray nozzle, in that order. A flow rate of 136 nL/min was chosen to match the flow rates measured using the on-chip sensors in “Standard Column with Active Sensors” configuration in order to enable a better comparison.

5.3. Results and Discussion

5.3.1. Microfluidic Chip/Components

The microfluidic chip was designed to be compatible with HPLC analyses. Important properties include high-pressure operation, solvent resistance, biocompatibility, and durability. These goals were largely achieved. During column packing the chip experienced pressures as high as 100 bar with no noticeable effects. Also, an analysis of the MS data while flowing a high percentage of acetonitrile through the chip did not indicate any significant source of background noise, confirming the solvent resistance of our chip. The use of known biocompatible, low-retention materials such as Parylene also assured compatibility with biological molecules. To demonstrate durability, individual chips were operated for more than 72 hours with only slight degradation to the electrospray nozzle.

The design and performance of the mixer, composition sensor, and flow sensor were all previously discussed in detail in Chapter 3. The characterization and performance of the rest of the individual components will be briefly described here.

5.3.1.1. Analytical/Trap Column

The dimensions of the analytical column were chosen to be comparable to a 50 μm ID column. One important characterization of the column that had to be performed was the determination of the flow resistance of the packed column. This was accomplished by pumping fluid through the column at a fixed pressure and measuring the resulting flow. For a column packed with 5 μm support, a flow resistance of 0.029 bar/(nL/min)/cP/cm was determined. This implies that the pressure needed to drive 100 nL/min of water (e.g., 1 cP viscosity) through a 3 cm column would be 8.7 bar. The same measurement was conducted with columns packed with 3 μm support and a flow resistance of 0.077 bar/(nL/min)/cP/cm was determined. The flow resistance ratio between the 3 and 5 μm bead-packed columns should be proportional to the square of the bead diameter, or 2.78. The measured ratio of 2.67 was a close match and the discrepancy could have easily been caused by irregularities in the support size and shape. The trap column, with a cross-sectional area 150% greater than the analytical column, showed a corresponding reduction in the flow resistance.

5.3.1.2. Bead Filter

The weir-type filters used in this device all had a height of approximately 3.5 μm. They effectively stopped 3 and 5 μm beads in the columns. The ability to retain 3 μm

beads was largely due to the fact that the beads were not perfectly spherical or uniform in size. The presence of just a few irregularly large beads was enough to prevent any further beads from passing through. The thickness variation of the filters across each wafer was estimated to be < 1 μm. Unfortunately this still meant that some devices were more effective in holding the beads than others, particularly when attempting to use 3 μm beads. This was remedied in some cases by using a small number (10–50) of 5 μm beads to plug the filter prior to actually packing the column with 3 μm support.

5.3.1.3. Electrospray

The electrospray nozzle was thoroughly tested before any separations were conducted. The nozzle was tested over a wide range of solvent compositions and flow rates. Stable electrospray was even obtained at flow rates < 50 nL/min, which is usually a good indication of a well-designed nozzle. The nozzle was tested in both orthogonal and head-on configurations and worked similarly in both cases. While the Agilent 1100 series LC-MSD SL ion trap mass spectrometer used in our separation experiments required the nozzle potential to be held at ground, many other mass spectrometers require the nozzle voltage to be floated at high voltage (~ 1–3 kV). The nozzle was tested under these conditions as well. The durability of the nozzle proved to be the one weak spot on the chip and it was generally the first component to wear out. The electrospray process appeared to slowly wear away the Parylene, causing a blunting of the nozzle tip and degrading performance over time. A metal-coated electrospray tip could potentially be used to improve durability.

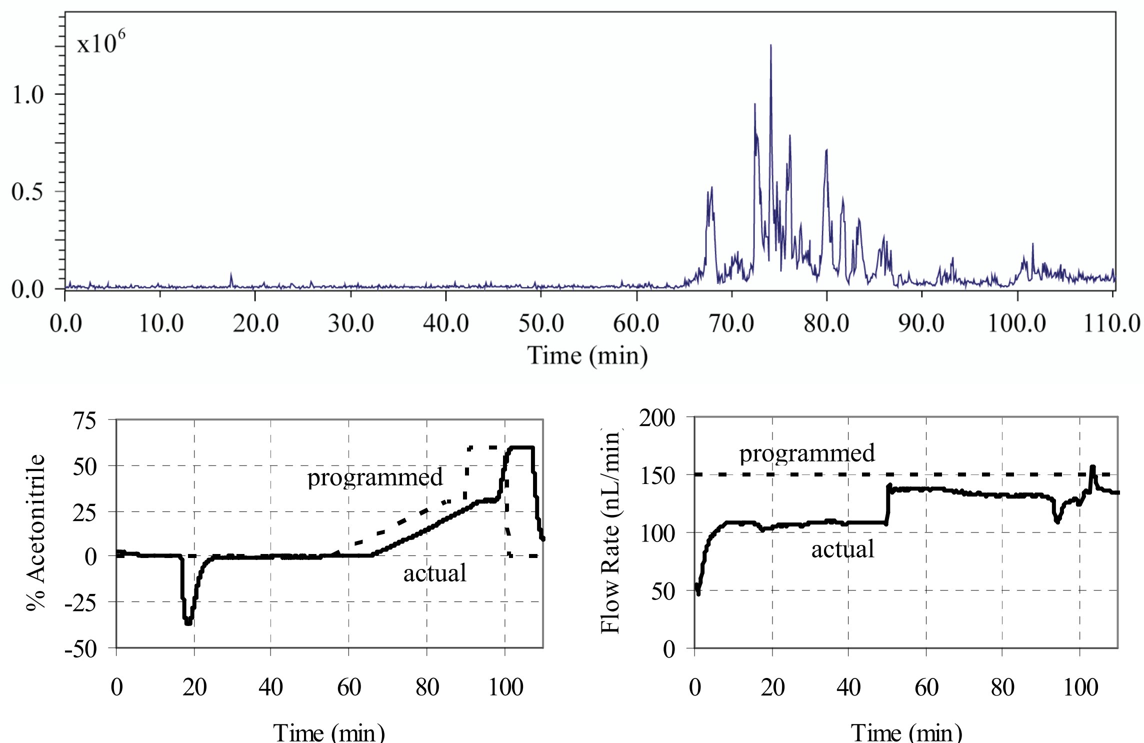

Figure 5-9: Separation results using the "Standard Column with Active Sensors" configuration. The MS data (top), flow sensor (bottom right), and composition sensor (bottom left) data are plotted.

5.3.2. Standard Column with Active Sensors

Separations of 250 fmol Bovine Serum Albumin (BSA) digest were conducted and yielded results that were reasonable given the column dimensions and separation method. An example can be found in Figure 5-9 along with the recorded sensor data. A subsequent analysis of the MS data yielded protein coverage of about 50%, similar to what is normally achieved using a commercially available nanobore column. This meant that 50% of the amino acids in the BSA protein were identified during the analysis. The sensor data provided interesting insight into the actual separation itself. Based on the programmed composition profile and the composition detector data, there was an 11 min delay for compositional changes to propagate from the pump to the on-chip sensors. The

negative acetonitrile percentage registered at ~ 15–25 min indicated the sample plug being loaded onto the column. The sensors also clearly registered the passing of the gradient through the column from 65–95 min. This corresponded very well with the actual elution of the peptides from the column. Some delay was expected between the gradient reaching the sensors and the peaks eluting because the sensors were located at the head of the column. Breakthrough time for our column and flow rate was approximately 1 min.

Another interesting consequence of having the sensors was that we were able to detect flow rate inconsistencies. For example, from 0–50 min, when the autosampler valve was in mainpass mode, the flow rate was much lower than when the autosampler valve was in bypass mode (> 50 min). This was most likely due to the large internal autosampler volume when in mainpass mode. Our sensor data also indicated that there were fluctuations in flow rate during the actual gradient and particularly when there were sudden changes in the fluid composition (e.g., at the 90 min mark). These flow errors were confirmed by measuring accumulation of liquid in a clear capillary to determine the actual flow rate. We believe that these fluctuations had minimal effect on the actual separation itself. In fact, when performing the same experiment many times, the results were nearly identical, indicating excellent repeatability for our HPLC pump and on-chip column.

The integration of sensors into the column has many possible uses. By monitoring the flow in the column and comparing it to the flow that the pump is indicating, it can be very easy to troubleshoot leaks or blockages in the fluid lines. These problems could be nearly impossible to find otherwise, given the low working flow rates.

The sensors could also possibly improve the efficiency of HPLC systems. Since the column conditions are always known, the guesswork can be taken out of the steps such as column equilibration. Finally the addition of sensors could also potentially open the door for comparing separations done on the different HPLC systems. HPLC systems naturally tend to behave slightly differently from one another, particularly when gradient elutions are used. This is caused by different systems having different delay volumes. This variation in delay essentially causes different degrees of gradient "blurring". By monitoring the flow at the column and correlating that with the separation, comparisons could be made based on the measured column conditions rather than the programmed elution profile. This ability would enable better cross-laboratory comparisons of gradient-based separations.

5.3.3. Vented Column with Non-Active Sensors

One drawback of directly injecting the sample onto the analytical column was that it could only be done at a relatively low flow rate because of pressure considerations. If the sample volume was high, the sample loading process took a long time. This configuration, with the addition of a shorter trap column, was designed to address these problems. The shorter and wider trap column could be used to load the sample at high flow rates while still maintaining a reasonable backpressure. Separations of different amounts of a BSA digest are shown in Figure 5-10. The intensity of the peaks scaled nearly directly with the amount of sample, indicating ideal and repeatable capture/elution of the sample by/from the trap column. Coverage of the BSA protein was similar to the previous setup.

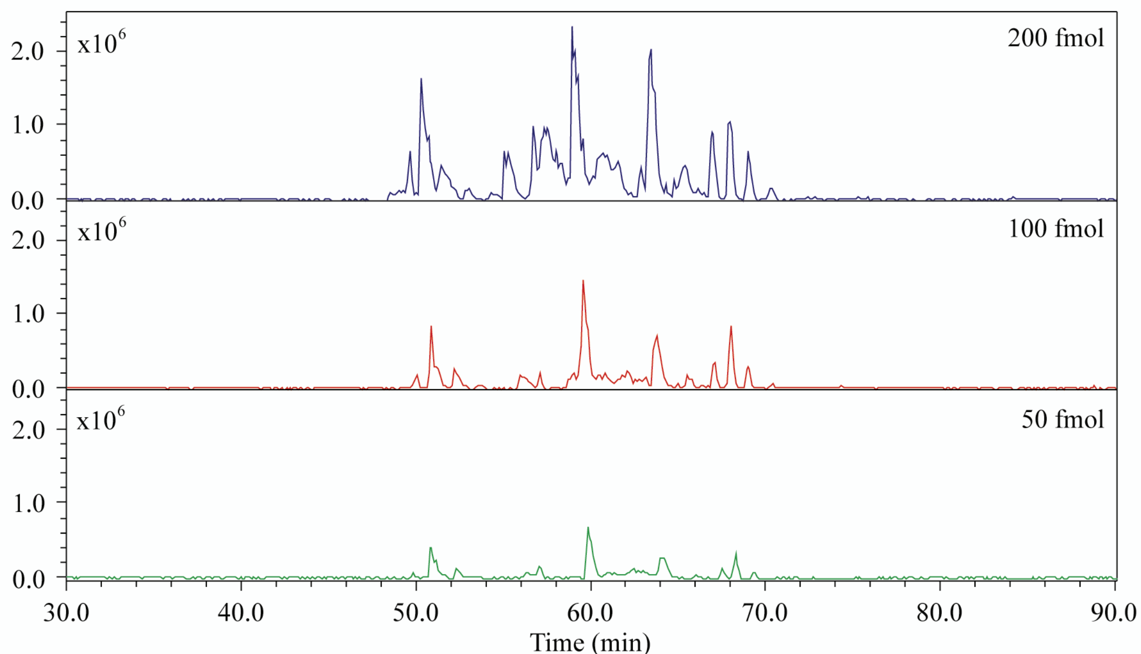

Figure 5-10: Separation results using the "Vented Column with Non-Active Sensors" configuration. The MS data for three different sample concentrations are plotted.

The sensors, while not activated in these separation experiments, could have been used to monitor the sample loading and gradient elution in much the same way done in the "Standard Column with Active Sensors" configuration. Another advantage of a trap column, besides improved sample loading times, is that it can be used to enrich "dirty" samples without exposing the mass spectrometer to unwanted contaminants.

5.3.4. Feedback-Controlled Operation

Before using the sensors for feedback-controlled separations, the feedback system was characterized. When using the on-chip sensors with our two-channel pump, the standard deviation from the set points flow rates and compositions was very low, approximately 0.3% acetonitrile and 1.2 nL/min. These deviations were either the same

or slightly higher than the sensor precision values determined in our calibrations in Chapter 3, indicating that control was largely limited by the characteristics of the sensors. When running programmed linear gradients like those seen in nanoscale HPLC, run-to-run repeatability was excellent. Standard deviations from the mean gradient were only 0.3% acetonitrile and 1.6 nL/min

One way to check whether the flow control system was working properly was by comparing the pressures inside the two pump channels during feedback-controlled gradient generation with the pressures expected based on theoretical calculations. In our fluidic system there are three important fluidic resistances: the resistance of the tubing connecting channel A of the pump to the chip, the resistance of the tubing connecting channel B of the pump to the chip, and finally the column resistance. The relevant resistances, pressures, and flow rates are all shown in Figure 5-11 using an electrical circuit analogy.

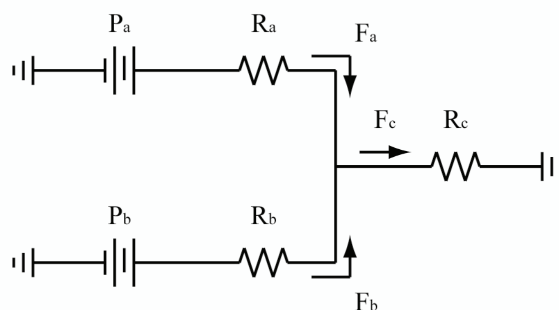

Figure 5-11: Equivalent electrical circuit for the fluidic system

While the viscosity of the liquid flowing through R_a and R_b is constant, the viscosity of the fluid flowing through the column is actually dependant on the ratio between F_a and F_b, since the viscosity of acetonitrile/water mixtures is dependant on the

acetonitrile/water ratio. Taking this into account, the governing series of equations comes directly from the application of the fluidic equivalents of Kirchoff's loop rules:

$$P_a(t) - R_a F_a(t)\eta(0) - R_c F_c(t)\eta\left(\frac{0.6F_b(t)}{F_a(t)+F_b(t)}\right) = 0$$

$$P_b(t) - R_b F_b(t)\eta(0.6) - R_c F_c(t)\eta\left(\frac{0.6F_b(t)}{F_a(t)+F_b(t)}\right) = 0 \text{, (equation 1)}$$

$$F_c(t) = F_a(t) + F_b(t)$$

where η(x) is a known function representing the absolute viscosity of the liquid as a function of the acetonitrile amount (e.g., η(0) being the absolute viscosity of a 100% water solution and η(1) being the absolute viscosity of a 100% acetonitrile solution), and channels A/B contain a 100/0/0.1 and 40/60/0.1 (water/acetonitrile/formic acid) solutions, respectively. R_a, R_b, and R_c can all be independently measured, meaning that P_a and P_b can be readily calculated for any given desired flow profile ($F_a(t)$, $F_b(t)$).

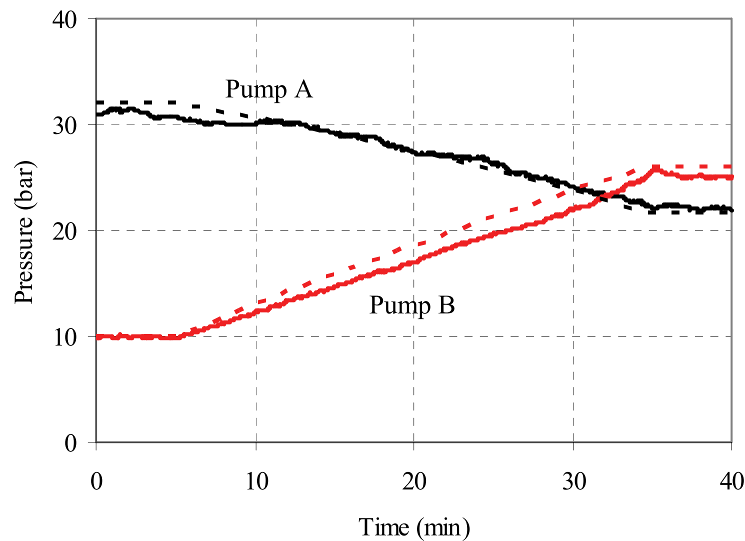

Figure 5-12: Comparison between the pressures obtained during feedback drive operation of a 0 to 30% acetonitrile gradient (solid lines) versus the pressure calculated using a mathematical model (dotted lines).

Figure 5-12 shows a comparison between the calculated pressure curves and the ones obtained during feedback-driven operation for a 0 to 30% acetonitrile gradient (1%/min) at a flow rate of 150 nL/min. For this simulation, the following resistance values were measured and used: $R_a\eta(0)$ = 0.148 bar/(nL/min), $R_b\eta(0.60)$ = 0.206 bar/(nL/min), and R_c = 0.110 bar/(nL/min)/cP. The good correlation was confirmation that the closed-loop flow control system was working properly.

5.3.5. Standard Column with On-Chip Feedback-Controlled Flow Control

This last separation configuration was designed to show the advantages of using the integrated sensors for feedback-driven gradient generation. Consecutive separations of 250 fmol BSA digest are shown in Figure 5-13.

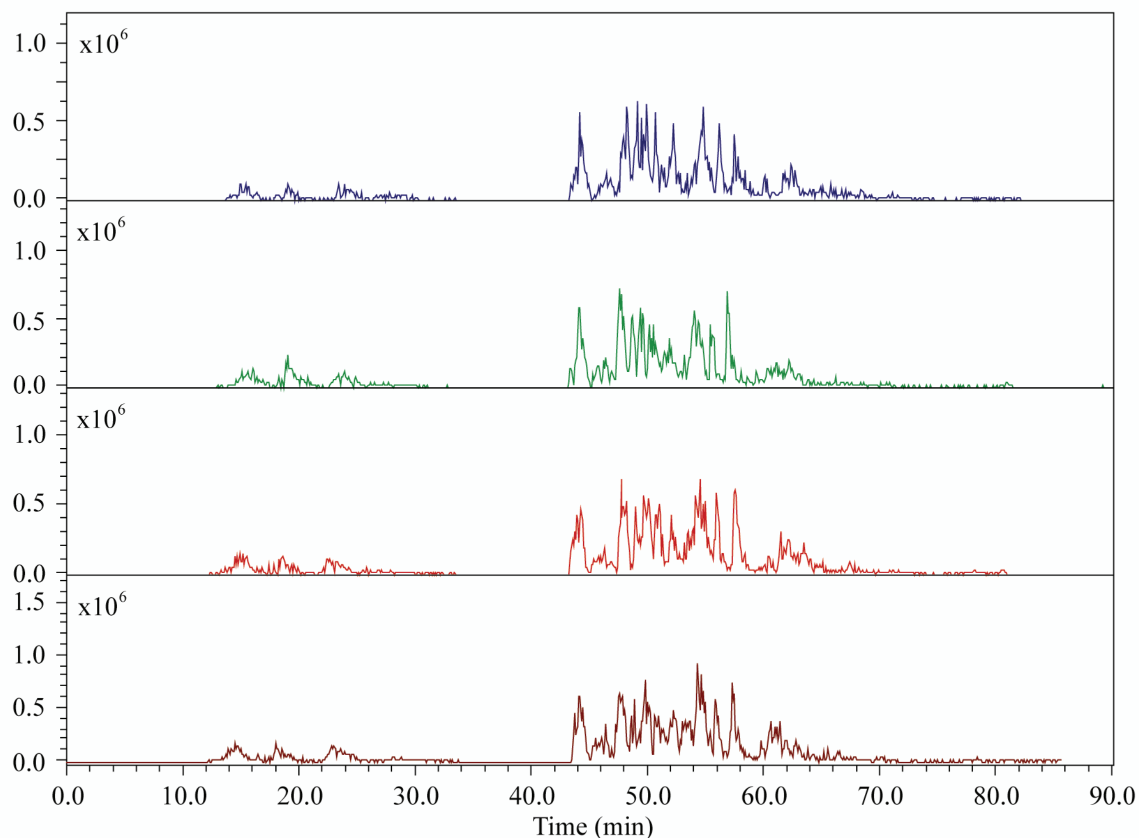

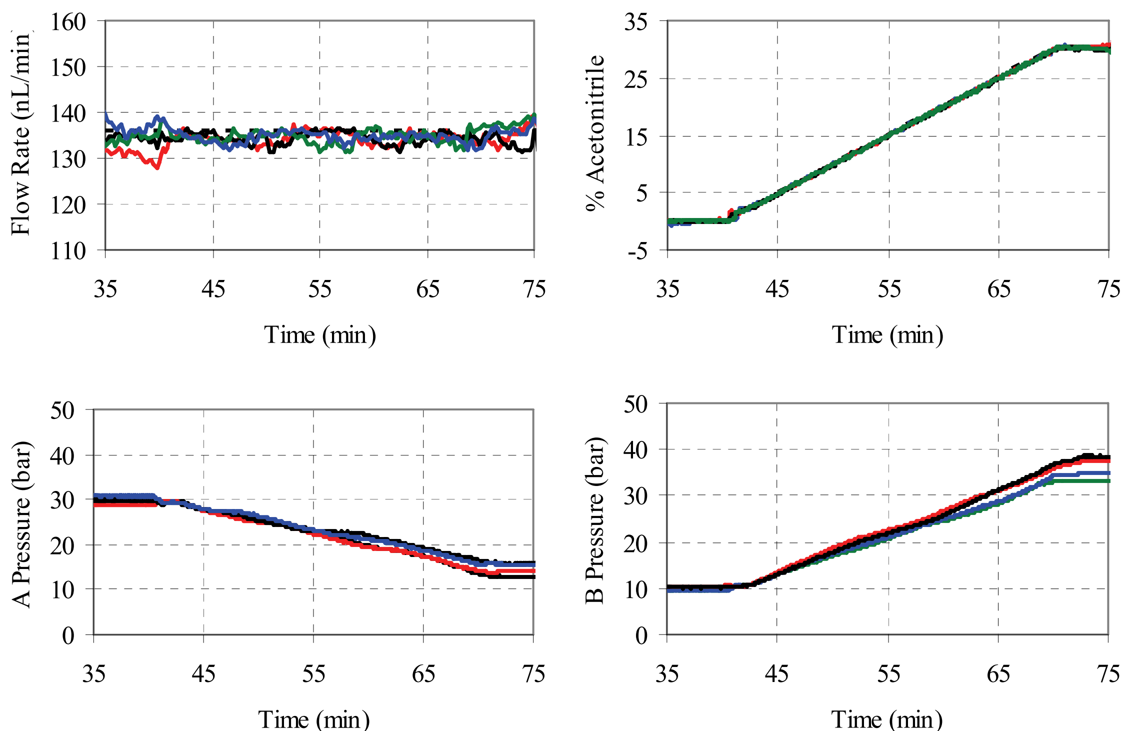

Figure 5-13: Separation results using the "Standard Column with On-Chip Feedback-Controlled Flow Control" configuration. The MS data (top), flow sensor (middle left), composition sensor (middle right), and pump pressure (bottom) data are plotted.

Protein coverage was generally around 50–60%, again in line with our previous experiments. The separations, while very similar to separations conducted using the commercial HPLC pump, in terms of peak resolution and protein coverage, did not exhibit the same kind of repeatability. Relative standard deviation (RSD) of the elution times for the mid-eluting peaks was 3.3%. This is slightly higher than the values generally specified for commercial nanoflow HPLC systems. One factor that might have contributed to this higher RSD value is that the gradient was generated so close to the column. Any minor fluctuations in the composition or flow rate will be seen by the column almost immediately, having an adverse effect on the separation. On the other hand, in a commercial HPLC system the swept volume between the pump and the actual

column is often times many orders of magnitude larger than in our chip. This is evident by the long gradient delay observed in the "Standard Column with Active Sensors" configuration. This long dwell time actually had the advantages of smoothing out any fluctuations in the flow. Possible corrections to this are more sensitive and accurate sensors or the inclusion of a larger volume buffer zone between the sensor and column.

On the other hand, having the gradient generated on chip does have many advantages. For example, complex gradient shapes can be generated with little distortion. Our system is well suited for this task because any gradient that is generated will maintain the desired flow profile with minimum "blurring". On the other hand, a conventional system would most likely produce distortions to complex flow profiles due to diffusion and non-perfect fluidic connections.

Another advantage of having the gradient generated so closely to the column is that rapid and accurate changes in the fluid composition can be made. This could allow for faster overall analysis times since time is not wasted waiting for changes in fluid compositions to reach the column. Another interesting possibility that this configuration opens up is the ability to do rapid analysis of unknown samples. Unknown samples are generally run using a long, shallow gradient over a wide organic range. With this chip, the gradient formation could conceivably be altered based on the mass spectrometer response allowing the gradient to be steeper when the peak density is low, and shallower when the peak density is high. The results of this initial separation could be used directly in generating a general method for that sample and ones of similar origin.

5.4. Conclusion

The fabricated chip proved to be very capable in conducting reverse-phase separations of peptide mixtures. This single chip had the ability to interface with commercial HPLC hardware, offering a plug-in solution for HPLC-MS/MS. Also, by connecting the chip to a custom-built two-channel pumping system, on-chip feedback-controlled gradient generation could be accomplished, producing a HPLC system that is unmatched when it comes to rapid and accurate changes in column flow.

There was some concern that the electrochemical TOF flow sensor might cause problems with the separation. For example, the high-voltage pulses will most likely oxidize/reduce the analytes. Fortunately, the duty cycle of the pulse generation is only 0.07% so only a tiny fraction of the analyte would have been affected. A second concern was directed at the gas generated during the high-voltage pulses. Because of the high pressure, the gas would have dissolved into the fluid immediately, but would have eventually resurfaced at the low-pressure end of the system (e.g., after the column). These gas bubbles could destabilize the electrospray process. Fortunately, no gas was observed post column and separations conducted with the flow sensor active were identical to ones conducted with the sensor disabled.

One element that was not used in this chapter was the high-pressure electrolysis pumps. Electrolysis electrodes were actually integrated on the chip, as seen in Figure 5-1, and consisted of an oval chamber defined in SU-8 with a set of interdigitated electrodes inside. These integrated pumps were ultimately not used because of the low volume. Even when using a CNC-machined reservoir, the overall volume of the liquid reservoir would have only been 2–3 μL, which is barely enough for a single separation. This

meant that the reservoirs would have had to be refilled after each separation, most likely using an automated refill system. The added complexity of this would have exceeded the pneumatic pump setup and was therefore not pursued.

Chapter 6: Portable High-Performance Liquid Chromatography Conductivity Detection (HPLC-CD) System

6.1. Introduction

High-performance liquid chromatography (HPLC), as discussed in Chapter 5, is a powerful separation technique which can be used to analyze complex mixtures of biological molecules. In the last chapter we demonstrated a miniature microfluidic platform for proteomic applications. While proteomic analyses are generally conducted in a laboratory, there are several potential applications of HPLC that would require a miniature separation platform for field use. One example is a miniature biodetection system that could be part of an early warning system. Similarly, a hand-held system can be used by first responders to quickly assess the extent of a biological disaster. While the HPLC-tandem mass spectrometry (MS/MS) chip described in Chapter 5 could be used for biodetection, there were several factors that limited its portability. Mass spectrometers are expensive, bulky, and consume significant power, making them unsuitable for a hand-held tool. While there are efforts to create miniature mass spectrometers[78], the inability to generate high vacuums has hindered performance. Another factor that limited the portability of our HPLC-MS/MS chip was the large size and high power consumption of the pumps. In the case of the pneumatic pumping system, a high-pressure gas source was also required.

The HPLC/MS-MS chip had most of the components integrated onto a single chip. Another possibility is to make several microfluidic devices and connect them together. This modular approach has many advantages. One obvious advantage is the ability to replace components if one were to break or wear out. The ability to switch out components can also be useful for other reasons. For example, the column chemistry can be changed by simply swapping out one column for another. The biggest disadvantage of using a modular system is that it adds volume between the different components in the fluidic system. If these volumes are not carefully controlled, the overall separation performance of the system can be affected. Another disadvantage is that a modular system places an added burden on the packaging because chip-to-chip connections become necessary.

This chapter will describe the design and fabrication of a completely portable separation platform. Many of the devices described in the earlier chapters, as well as newly presented devices, were connected together using a modular concept to create a fully functioning gradient-capable reverse-phase nanoscale HPLC system. To date, only one fully portable HPLC system has been demonstrated, by Sandia National Laboratories[73, 74]. Their portable system integrates an electrokinetic pump, valves, column, and an optical detector into a handheld device. The integration of sensors and use of closed-loop control is one big distinction of the presented portable system. These added features enable the use of more advanced separation techniques and improve reliability.

6.2. Experimental

6.2.1. Modular System / Individual Chip Design

There were three distinct microfluidic chips/devices used in this modular, miniature separation system.

1. **Electrolysis Pumps**: The pumps developed in Chapter 4 were used to provide high pressure and low power delivery of the mobile phases. Two pumps were used, one loaded with an aqueous solution and the other with a predominantly acetonitrile mixture.
2. **Flow Control**: The standalone flow control chip described in Chapter 3 was used to mix the two pump flows, measure the acetonitrile percentage, and determine the total flow rate. The sensor data was used as feedback to control the pumps.
3. **Separation/Detection**: The final chip included a separation column with integrated conductivity detector.

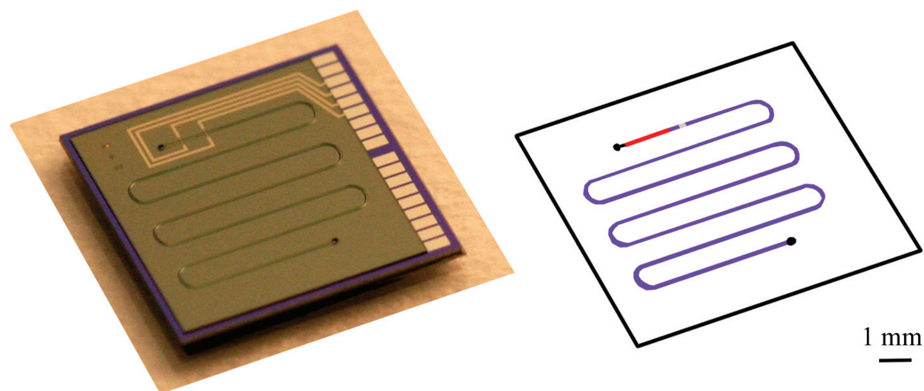

Figure 6-1: A picture and diagram of the presented separation/detection chip. The various components are highlighted in purple (analytical column), gray (bead filter), and red (conductivity detector). The black circles represent the location of the inlet and outlet ports.

Each of these devices were packaged individually and then connected to form a fully functioning HPLC system. The design of the electrolysis pumps and flow control chip were discussed earlier, in Chapters 4 and 3, respectively. The separation/detection chip will be discussed in more detail in this chapter and is shown in Figure 6-1.

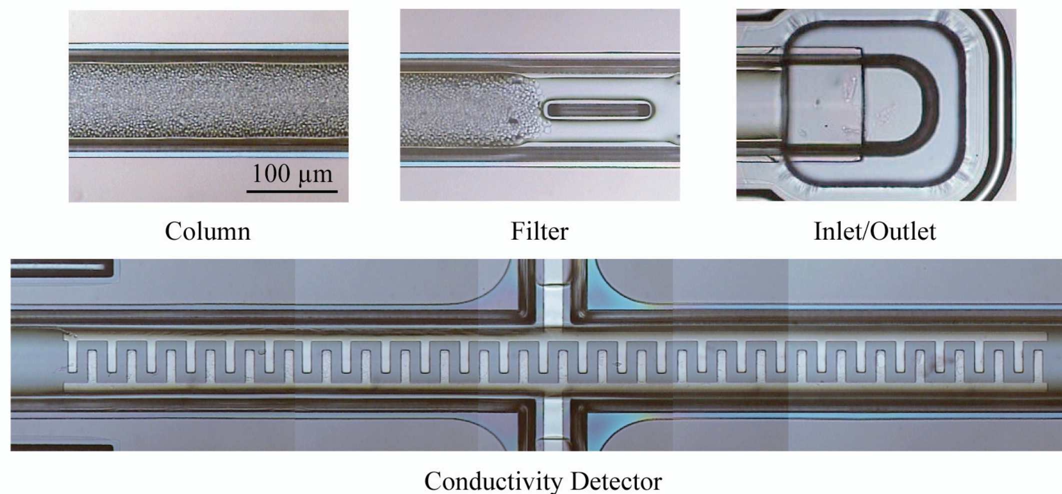

Figure 6-2: Close-up pictures of all the individual components on the column/detection chip. The larger (70 x 1000 (W x L) μm^2) detector is shown here. All devices are shown at the same scale.

The individual components on the separation/detection chip can be seen in Figure 6-2. The column had a cross section of 80 x 25 (W x H) μm^2 and a total length of 4.6 cm. The filter was a weir-type filter with a height of 3.5 μm. The fluidic inlet/outlet ports were defined in SU-8 and were 200 x 200 (W x L) μm^2. There were two sets of detector electrodes on the chip. The first consisted of a pair of interdigitated electrodes with a width/spacing of 10/10 μm. These electrodes covered a total area of 70 x 500 (W x L) μm^2 and were located in a channel with a cross section of 80 x 25 (W x H) μm^2. The resulting detector volume was 1 nL. The second set of electrodes were identical except

they covered a larger area of 70 x 1000 (W x L) μm^2. The detector volume was also larger as a result (e.g., 2 nL). The two detectors could also be connected in parallel to form a single 70 x 1500 (W x L) μm^2 sensor.

6.2.2. Chip Fabrication

The processes used to make the electrolysis pump and flow control chip were already discussed in Chapters 4 and 3, respectively. The process to make the separation/detection chip was identical to the one used to make the flow control chip. A diagram of the separation/detection chip at various points in the process is shown in Figure 6-3. A description of the individual steps can be found in Chapter 3.

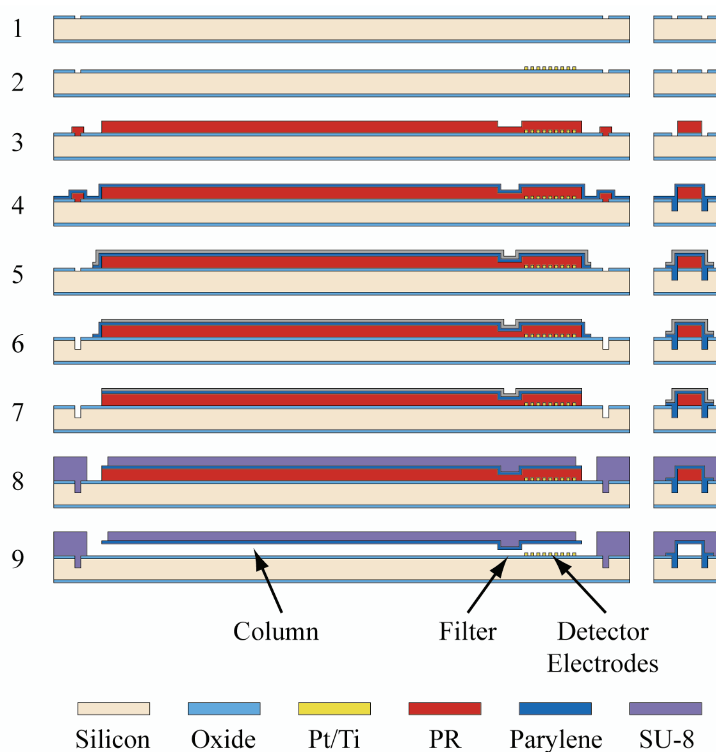

Figure 6-3: Process flow for the separation/detection chip. The left-hand column shows a cross-sectional view where the liquid flow is from left to right. The right-hand column shows a cross-sectional view where the liquid flow is into the page.

6.2.3. Chip Packaging / Preparation

The packaging of the electrolysis pumps and flow control chip were described previously in Chapters 4 and 3. The packaging of the separation/detection chip was identical to that of the flow control chip, except for the number of fluidic ports. The separation/detection chip used a manifold with only two fluidic ports, one as an inlet feeding into the column, and the other as an outlet at the other end.

The column on the separation/detection chip, like the column on the HPLC-MS/MS chip in Chapter 5, had to be packed with beads prior to testing. This was accomplished by using the same two-port manifold equipped during normal operation of the chip. The column was slurry packed using 3 μm C_{18} support (Varian, Inc.) at a pressure of 100 bar using the same setup described in Chapter 5.

6.2.4. Electrolysis Pump Operation

The electrolysis pumps were controlled by applying a current through the electrodes. The magnitude of the current was varied based on the sensor data and programmed flow profile. Current was delivered using a voltage-controlled current source (OP741, National Semiconductor) with a maximum output voltage of +/-12 V. Detailed information about the pump operation can be found in Chapter 4.

6.2.5. Flow Control Chip Operation

The flow control chip had a passive mixer along with two sensors. The first sensor was an impedance-based composition sensor, which determined the water/acetonitrile percentage based on electrical measurements. The second sensor was a

time-of-flight (TOF) flow sensor, which measured the velocity of an electrochemically generated ion pulse to deduce the flow rate. The flow control chip used here is identical to the standalone device discussed in Chapter 3, which should be referred to for more detail.

6.2.6. Detector Operation

The detector on the separation/detection chip was based on measuring the conductivity of the solution. Conductivity detection was achieved by applying a 100 kHz, 200 mV AC (HP8111A, Agilent Technologies) signal across the detector electrodes. The resulting current was measured using an I→V converter (OP37, Analog Devices). The AC voltage output was converted to a DC signal using an AC→RMS converter (AD636, Analog Devices). The total gain (V_{out}/I_{pp}) was 1.07×10^5 Ω. For all experiments in this chapter, both sets of detector electrodes were connected in parallel to form a single 70 x 1500 (W x L) μm^2 sensor.

6.2.7. Chip Separation Configurations

Two different separation configurations were used. In the first setup, the electrolysis pumps were not used and the flow control and separation/detection chips were interfaced with a commercial Agilent HPLC pump to conduct separations. This was done to provide a baseline separation for the purpose of comparison. In the second separation configuration, the high-pressure electrolysis pumps were used to drive the fluid flow.

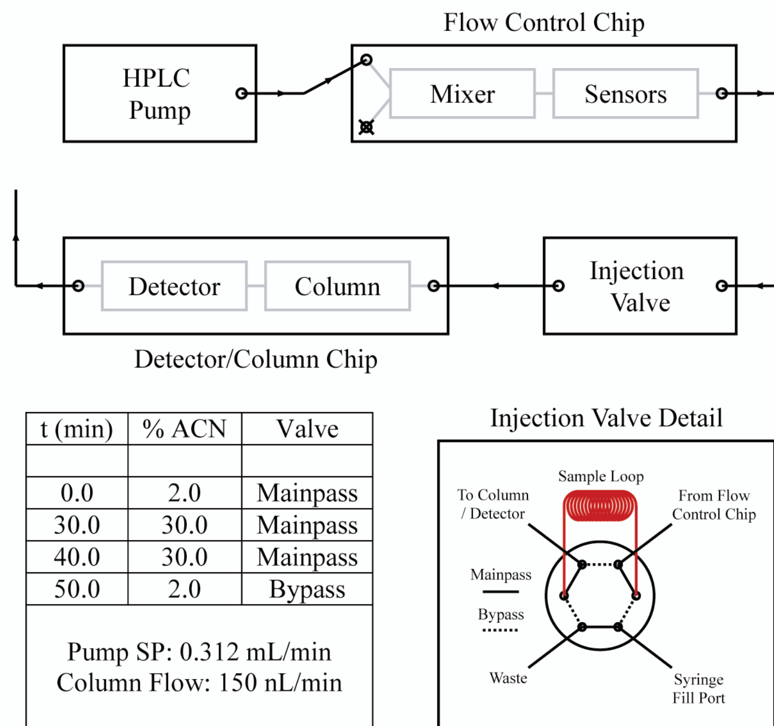

t (min)	% ACN	Valve
0.0	2.0	Mainpass
30.0	30.0	Mainpass
40.0	30.0	Mainpass
50.0	2.0	Bypass

Pump SP: 0.312 mL/min
Column Flow: 150 nL/min

Figure 6-4: Diagram of the commercial HPLC pump-driven setup along with the separation method. An inset showing the operation principle of the injection valve is also included.

6.2.7.1. Separation with Conventional HPLC Pump

In this separation configuration, an Agilent 1100 Series Quaternary Pump equipped with a homemade 2080:1 capillary flow splitter was used to run the separation. The pump was equipped with a water/acetonitrile (0.1% formic acid) solvent system and connected to one of the mixer inputs on the flow control chip, with the other mixer input blocked off and unused. The flow was directed through the mixer and sensors, out of the flow control chip, and into a manually actuated Nanovolume® two-position, six-port sample injection valve (Vici Valco Instruments). This two-position valve allowed a sample loop (100 nL) to be filled via a syringe and then switched online. The output of

the valve was connected to the separation/detection chip. Fluidic connections between the different components were made using 25/360 μm (ID/OD) fused silica tubing (Polymicro Technologies). This setup is diagrammed in Figure 6-4.

To run a separation, first, a 5 μL syringe (Hamilton Corp) was used to load the sample into the injection valve's 100 nL sample loop. The loop was then switched online and the sample pumped onto the column using a 98/2/0.1 (water/acetonitrile/formic acid) solution. Simultaneously, the HPLC pump began its programmed linear gradient from 2 to 30% acetonitrile over a period of 30 min. The pump held the composition at 30% acetonitrile for 10 min before ramping back to 2% over the course of 10 min. The pump flow rate was held at 0.312 mL/min throughout the separation, which, with the use of the flow splitter, resulted in the delivery of 150 nL/min to the column.

6.2.7.2. Separation with Electrolysis Pumps

The second separation configuration swapped out the Agilent HPLC pump for two high-pressure electrolysis pumps. One pump, designated channel A, was filled with a 100/0/0.1 (water/acetonitrile/formic acid) solution while the other pump, designated channel B, was filled with a 40/60/0.1 solution. Each pump had a 300 μL electrolysis chamber, which was connected to a 1 mL stainless steel solvent loop (Upchurch Scientific). Each of these pumps were connected to one of the mixer inputs on the flow control chip using 15/360 μm (ID/OD) fused silica tubing (Polymicro Technologies), with manually actuated valves (Upchurch Scientific) placed in between. The remainder of the setup was identical the Agilent HPLC pump-driven setup. A diagram of this setup

can be found in Figure 6-5. A photograph of the actual experiment can also be found in Figure 6-6.

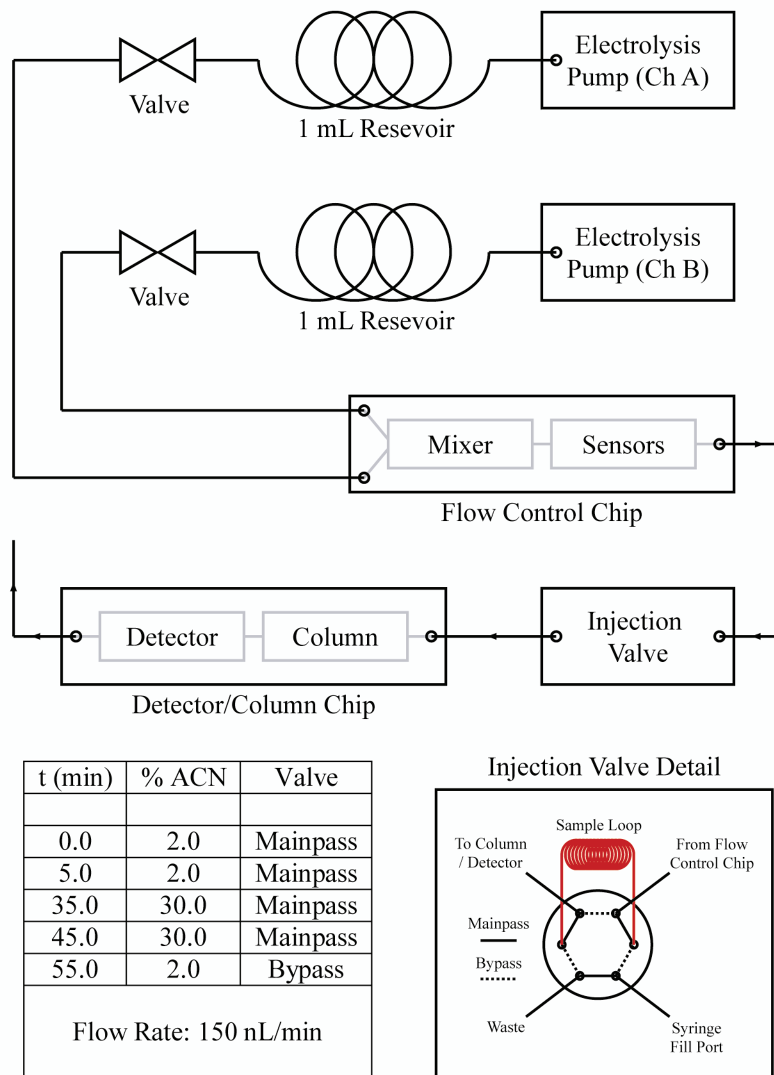

t (min)	% ACN	Valve
0.0	2.0	Mainpass
5.0	2.0	Mainpass
35.0	30.0	Mainpass
45.0	30.0	Mainpass
55.0	2.0	Bypass
Flow Rate: 150 nL/min		

Figure 6-5: Diagram of the electrolysis pump-driven setup along with the separation method. An inset showing the operation principle of the injection valve is also included.

The separation method was slightly different from the Agilent HPLC pump-driven separation. After filling the sample loop and switching the loop online as done before, the gradient was started after a 5 min delay instead of immediately after the valve

switch. This accounted for the gradient delay in the Agilent HPLC pump (e.g., the time it took for changes in composition to propagate from the pump to the flow control chip) and was done to try and enable a better comparison between the two separation configurations.

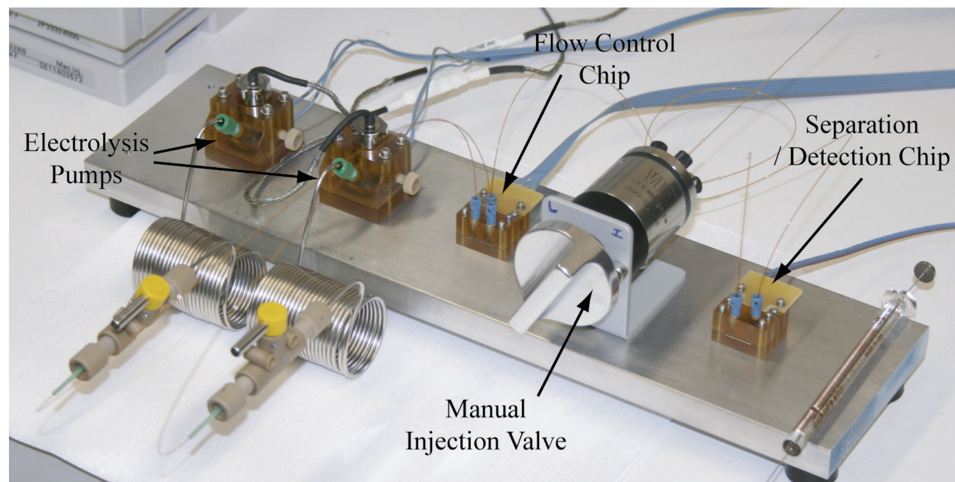

Figure 6-6: A photograph of the entire separation system

6.2.8. Data Acquisition and Computer Control

A DAQPad-6020E data acquisition unit (National Instruments) in conjunction with LabVIEW (National Instruments) was used to control and monitor the separation system. The control of the electrolysis pump currents; monitoring of the pump pressures; operation of the sensors; analysis and recording of the sensor data; feedback control algorithms; and collection of the detector data were all implemented in LabVIEW. Flow-rate measurements were conducted at a frequency of 0.1 Hz, and composition measurements at 1 Hz. The electrolysis control currents were updated at a frequency of 1 Hz also. The Agilent 1100 Series Quaternary Pump (Agilent Technologies), when used, was controlled using the manufacturer's software.

6.3. Results and Discussion

6.3.1. Microfluidic Chips/Components

The electrolysis pump and flow control chip were studied and presented in detail in Chapters 3 and 4. Two of the three components on the separation/detection chip (e.g., analytical column and filter) were identical to components already on the HPLC-MS/MS chip and were described in Chapter 5. Only the conductivity detector will require further discussion in this chapter.

6.3.1.1. Conductivity Detector

Originally, the detection electrodes were designed to be used for both electrochemical and conductivity detection. However, initial tries to implement electrochemical detection using DC amperometry were met with little success. It was believed that this was mainly caused by contamination of the electrode surface. Many of our electrode-based sensors, such as the composition sensor in Chapter 3, were also very easily contaminated. This problem was compounded by the fact that there was no direct access to the electrodes and the usual mechanical methods of cleaning the working electrodes were not possible. Pulsed amperometric techniques, which electrochemically clean the electrode surface periodically, would have been more effective, but were not pursued.

Electrochemical detection was abandoned in favor of conductivity-based detection. AC conductivity measurements using our microfabricated electrodes proved to be much less problematic. This was most likely because the use of an AC excitation signal with sufficient frequency eliminated the sensor's dependence on a clean electrode

surface. Figure 6-7 contains a plot showing the response of the conductivity sensors to varying concentrations of formic acid, which is the main electrolyte in the mobile phases. The sensitivity was estimated be better than 1 μM. One limitation of conductivity detection is that only ions can be detected, limiting what analytes can be analyzed. Post-column reactions/derivatizations could be potentially used and would enable the detection of normally neutral molecules, providing more general detection capability.

During the passing of a solvent gradient, this detector demonstrated significant drift. This was expected, due to changes in the bulk fluid conductivity at various water/acetonitrile ratios. This was the same principle that was used for composition measurements. This drift was accounted for by comparing actual separations with blank runs. Direct subtraction of the two signals gave a well-compensated detector signal with minimal drift.

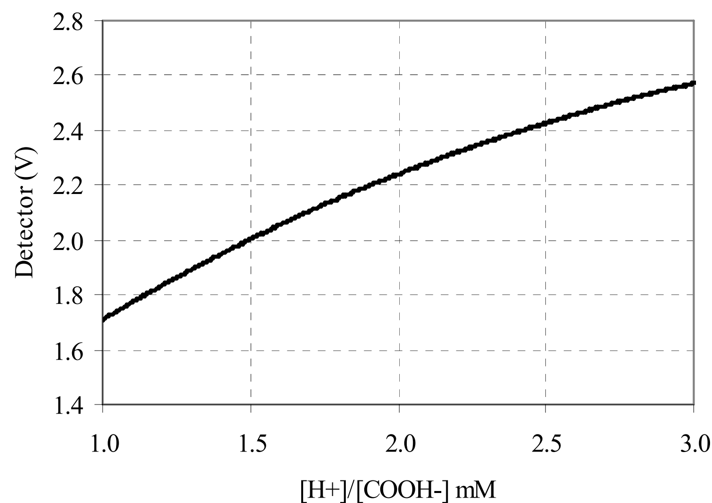

Figure 6-7: Detector response at different aqueous concentrations of $[H^+]/[COOH^-]$. 0.1% formic acid in water corresponds to 2.1 mM.

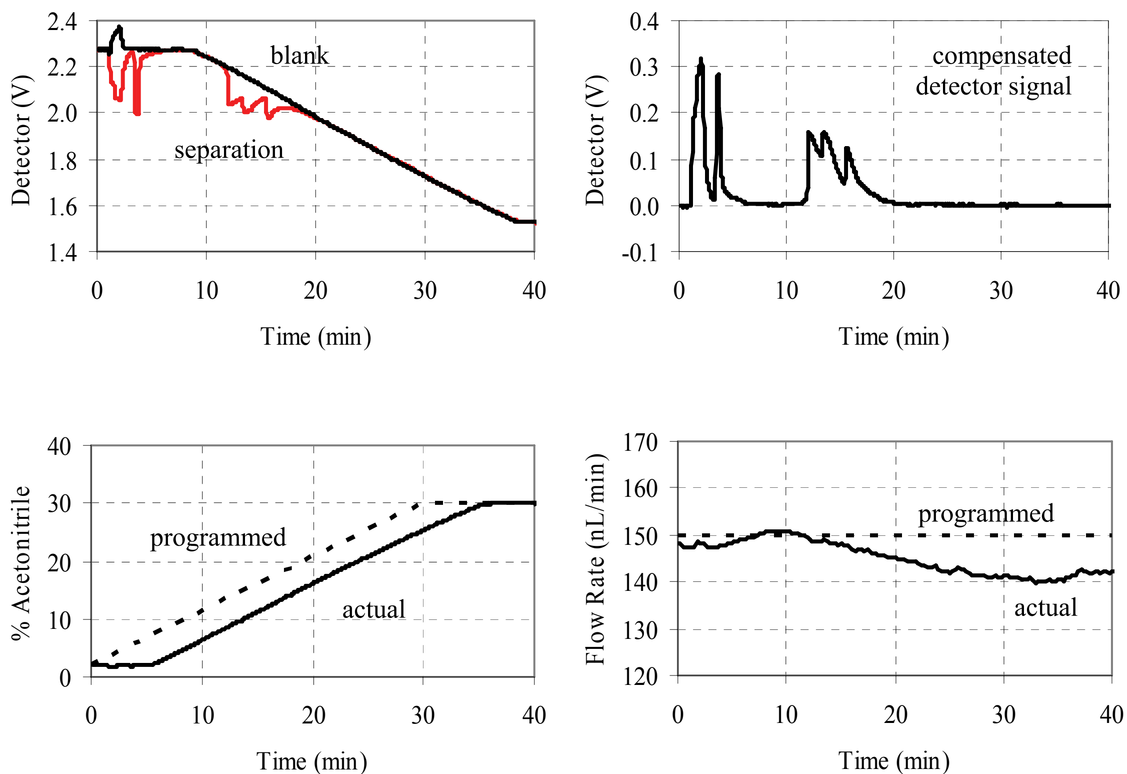

Figure 6-8: Separation of a five-peptide sample. The raw detector and baseline signals (top left) are shown along with the compensated detector signal (top right). Also shown are the composition (bottom left) and flow rate (bottom right) as indicated by the integrated sensors.

6.3.2. Separation with Agilent HPLC Pump

A peptide mixture was used to assess the separation performance. The mixture contained five peptides: Gly-Tyr (MW 238.2), Val-Tyr-Val (MW 379.5), Methionine Enkephalin Acetate (Tyr-Gly-Gly-Phe-Met) (MW 573.7), Leucine Enkephalin (Tyr-Gly-Gly-Phe-Leu) (MW 555.6), and Angiotensin II (Asp-Arg-Val-Tyr-Ile-His-Pro-Phe) (MW 1046.2). Separations of 100 nL of a 1 mg/mL (each component) stock sample solution were conducted and an example can be found in Figure 6-8. The separations showed the

expected five peaks. The di- and tri-peptides both eluted out before the start of the gradient. This was expected because of their small size.

Based on the composition sensor data, there was a delay of approximately 6 min for compositional changes to reach the flow control chip after being generated in the HPLC pump. After reaching the composition sensor, it took another 3 min for the liquid to reach the end of the column. The 3 min delay time included the sample loop volume because it was left online during the entire separation. The composition sensor indicated a highly linear gradient delivered by the HPLC pump. The flow sensor also indicated good flow stability. Some flow fluctuations were observed, particularly during the gradient. This is highly characteristic of split-flow nanoflow systems where compositional changes propagate at varying speeds along the two flow paths, slightly changing the desired 2080:1 split flow ratio.

One of the problems with this separation was that a very large quantity of sample had to be used. This was mainly due to a relatively low detector sensitivity, at least when compared to MS. Overall, 0.1 μg of each peptide (e.g., 0.5 μg total amount) had to be injected to get good peak detection. Unfortunately, this was near or exceeding the amount of sample that would normally be appropriate for a column of these dimensions. As a result, overloading effects were seen. Characteristic behavior that indicates sample overloading are peaks that show a steep rise, but slow falloff rather than the desired symmetrical peak shape. The last three peaks in our separation were classic examples of this. Besides poor peak shapes, sample overloading can also reduce the peak retention times. This is because of competition of analytes on the column, where more hydrophobic peptides displace the less hydrophobic ones. It is expected that with an

improvement in detector sensitivity, the amount of sample could be reduced, allowing a better overall separation.

One interesting point that should be noted was that the analyte peaks were detected as a decrease in conductivity. This was caused by the proton transfer between the solution and the peptides. H^+ was the main ion in the mobile phases (from the formic acid). It also had the highest contribution to the overall liquid conductivity because of its high mobility. At low pH, the amine group on the amino acids accepted an H^+. This essentially removed H^+ ions from solution and put a net positive charge on the peptide. While the total charge in the solution remained the same, the overall mobility of the charged peptide was significantly lower than the free H^+ ions, resulting in a lower overall conductivity. Originally, separations were conducted using 0.1% trifluoroacetic acid (TFA) rather than formic acid. TFA is usually used by default for most peptide/protein separations. When TFA was used in our separation experiments, the sensitivity of the conductivity detection dropped to a point where the peaks were only barely discernable. This was believed to be due to the ion-suppression properties of TFA. A similar problem is believed to happen when TFA is used with MS detection[79], which is why formic acid is preferred in HPLC-MS/MS.

6.3.3. Separation with Electrolysis Pumps

Because the electrolysis pumps were filled at atmospheric pressure, the pumps first had to be pressurized. This was most efficiently done by closing the valves separating the electrolysis pumps from the flow control chip. With a closed electrolysis system, similar to the one used for calibration in Chapter 4, a high current was applied

until the pressures reached the desired starting point, generally around 40–55 bar. The valves were then opened to push the fluids into the rest of the fluidic system and the closed-loop flow control system activated.

Because nearly all aspects of this separation system were susceptible to gas (e.g. composition sensor, flow sensor, column, and detector), the flow was allowed to flush the gas out of the fluidic system for 20–30 min before any separations were attempted. The existence of gas in the fluidic system was easily monitored by looking at the low pressure end of the separation system, or the detector. Any bubbles trapped in the fluidic system would become most prominent at the low-pressure end since the dissolved gas would "undissolve" there. The column detector was used to observe any passing bubbles, which expressed themselves as sharp valleys in the conductivity measurements. Flow equilibration was continued until the detector indicated a bubble-free flow. Another source of gas is from the electrolysis chamber itself. The use of a large buffer volume (> 1 mL) between the electrolysis chamber and the chip ensured that this would not cause any problems.

The overall design of the fluidic system had to take into account the capabilities of the electrolysis pumps. As was mentioned in Chapter 4, the electrolysis pumps were relatively slow to react, with a maximum ramp rate on the order of 0.1–0.2 bar/min. The fluidic system had to be designed to make sure that ramp rates beyond this were not needed for the programmed flow profiles. This was controlled by changing the diameter and length of the fused silica tubing connecting the pumps to the flow control chip. Large diameter and short lengths (e.g., low fluidic resistances) meant that only small changes in pressure were needed to achieve changes in composition. The opposite was

true of small diameter and longer tubing lengths. One drawback of making the fluidic resistance small was that it could cause instability in the system. Small pressure fluctuations in any of the pumps would have a large effect on the composition, potentially ruining the separation. In the end, these factors were balanced to achieve good pump stability while still maintaining the ability to change the composition at the requisite rate. The mathematical model developed in Chapter 4 to simulate the pneumatic pump-driven flow control system was also applied here to determine the optimal tubing lengths. In the end, 0.35 m long and 15 μm ID lengths of tubing were chosen for both pumps.

Another consequence of the slow response of the pump was that it complicated the design of the feedback algorithms. Ideally, with the slow response of these pumps, the control algorithms needed to not only consider the error history, but also look at the future desired flow profile. This, however, would have complicated the control algorithms. Another complication was that knowledge of the pump state was critical to pump control. The frequency response of the electrolysis pumps had a strong dependence on the volume of gas in the electrolysis chamber. Unfortunately, state estimation can be difficult, with errors likely building up over long periods of time. In the end, a digital control algorithm with three different current states was used for pumping. The pumps were run using only 0, 2, and 4 mA driving current. The values of these three levels were based on the pump calibration curves in Chapter 4. With an expected operating pressure of around 40 bar and a total flow rate of 150 nL/min, an average current in the vicinity of 2 mA was expected and was therefore chosen as the middle level. 4 mA, on the other hand, was capable of pressures and flow rates significantly higher than necessary and was chosen for the high-state level. The high

state was generally reserved for situations where the pump pressure needed to be increased. Finally 0 mA was used when there was a desire to decrease the pump pressure. The lookup table in Table 6-1 was used to control the pumps. This simple control algorithm proved to be very reliable and actually resulted in better performance than attempts to implement a PID control algorithm. During a typical gradient, compositional set point errors were < 0.1 % acetonitrile and flow rate errors were < 3 nL/min.

Flow Error (+) = too high (-) = too low	Composition Error (+) %ACN too low (-) %ACN too high	Pump A Current (mA)	Pump B Current (mA)
+	+	0.0	4.0
+	-	4.0	0.0
-	+	2.0	4 .0
-	-	4.0	2.0

Table 6-1: Digital control algorithm for electrolysis pumps

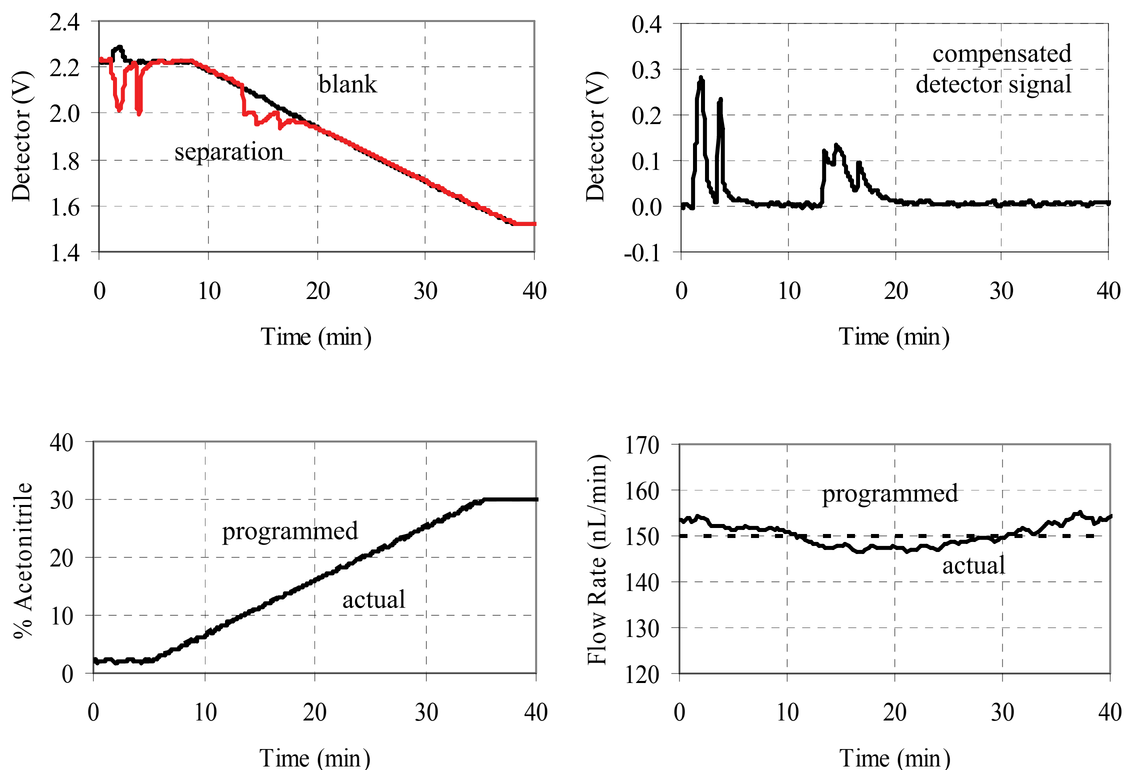

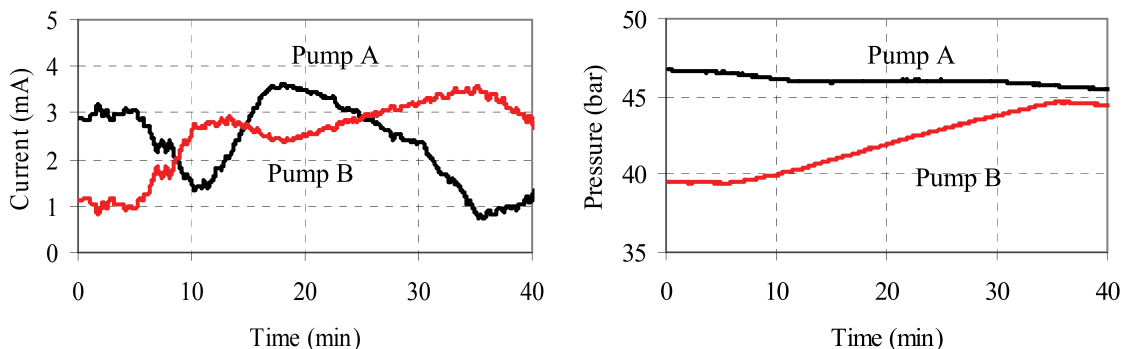

Figure 6-9: Separation of a five-peptide sample. The raw detector and baseline signals (top left) are shown along with the compensated detector signal (top right). Also shown are the composition (middle left), flow rate (middle right), pump-driving currents (bottom left), and pump pressures (bottom right). To better show the trend, pump currents were fitted with a 5 min moving average.

Figure 6-9 shows a separation of the same five peptide mixture used earlier. The sample amount was once again 100 nL of a 1 mg/mL stock solution. No real difference could be found between the separations conducted using this setup and the setup using the commercial HPLC pump. Small shifts in the peak positions could have been easily caused by differences in the flow rate.

Looking at the currents used to drive the electrolysis pumps revealed some interesting points. First of all, the average current was generally around 2–3 mA, which was completely expected based on our calibration of the electrolysis pump in Chapter 4. Also, the basic trend for the channel A current was downwards while the channel B current was upwards. This was expected, given the slope of the desired gradient. The pressure inside the electrolysis pumps also demonstrated upward and downward slopes as expected. The same mathematical model used in Chapter 5 to compare the actual

pneumatic pump pressures versus the expected ones could be applied to this system as well. The results of this calculation can be found in Figure 6-10. For this simulation, the following resistance values were measured and used: $R_a\eta(0) = 0.043$ bar/(nL/min), $R_b\eta(0.60) = 0.034$ bar/(nL/min), and $R_c = 0.281$ bar/(nL/min)/cP.

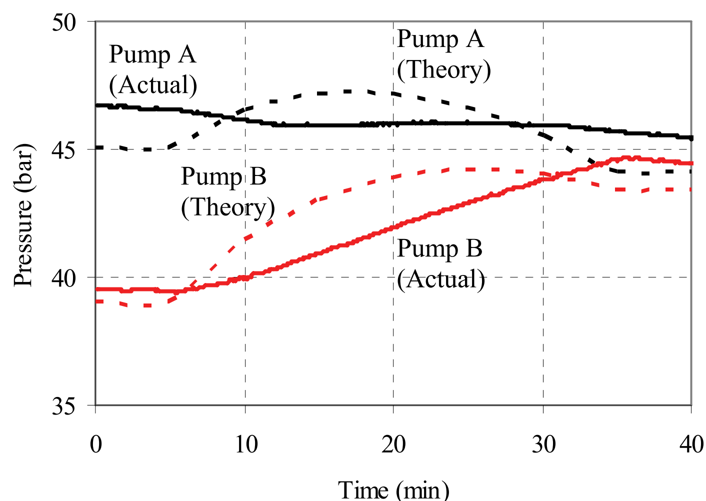

Figure 6-10: Comparison between the actual electrolysis pump pressures and the calculated ones

Interestingly enough, the ratio of the actual pump pressures matched up with the ratio of the calculated pressures very well. This was a good indication that the compositional changes were well controlled by the feedback system. This was backed up by the composition sensor data. The actual pump pressures differed slightly from those predicted by the model. The effect of this discrepancy was evident by looking at the flow rate data in Figure 6-9. From 0–10 and 30–40 min, the flow rate was higher than the 150 nL/min set point. Expectedly, the actual pump pressures were also higher than the theoretical pump pressures during those same intervals. The opposite was true of the 10–30 min interval where the flow rate was less than the 150 nL/min set point. Therefore,

even though the calculated and actual pressures look significantly different, the only consequence was a deviation of ±3 nL/min from the set point flow rate.

6.4. Conclusion

A portable HPLC separation platform was demonstrated and characterized. The platform used a modular approach where several different chip/devices were connected to form a working system. The overall size of the system (excluding electronics) was small enough to be handheld and had a total power consumption of only 30 mW. The separation performance was adequate but suffered due to column overloading, a result of a detector's less than ideal sensitivity. Improvements to the detector would likely have resulted in much higher-resolution separations.

Chapter 7: Conclusion

In the past few chapters, numerous individual microfluidic devices have been demonstrated. This includes: high-pressure electrolysis pumps, mixers, composition sensors, flow sensors, columns, frits, electrospray nozzles, and conductivity detectors. All the developed components were designed to withstand the rigorous high pressure, low flow rate, and solvent compatibility requirements of nanoscale HPLC. These individual components were then integrated together to form gradient-capable, reverse-phase, nanoscale HPLC systems.

Over the past few decades, almost every imaginable microfluidic component has been demonstrated, and each component has been realized using several microfabrication technologies. While standalone microfluidic components are sometimes useful, ultimately, integration of various microfluidic components is absolutely necessary to create more powerful microfluidic systems. The advancement of the microfluidics field hinges on this. Despite this fact, many microfluidic efforts are still aimed at producing individual components. It is hoped that the work presented in this thesis will encourage others to push for the high-level integration of microfluidic components as well.

Chapter 8: References

(1) Stone, H. A.; Stroock, A. D.; Ajdari, A. *Annual Review of Fluid Mechanics* **2004**, *36*, 381-411.

(2) Beebe, D. J.; Mensing, G. A.; Walker, G. M. *Annual Review of Biomedical Engineering* **2002**, *4*, 261-286.

(3) Ho, C. M.; Tai, Y. C. *Annual Review of Fluid Mechanics* **1998**, *30*, 579-612.

(4) Kovacs, G. T. A.; Maluf, N. I.; Petersen, K. E. *Proceedings of the IEEE* **1998**, *86*, 1536-1551.

(5) Bustillo, J. M.; Howe, R. T.; Muller, R. S. *Proceedings of the IEEE* **1998**, *86*, 1552-1574.

(6) Whitesides, G. M.; Ostuni, E.; Takayama, S.; Jiang, X. Y.; Ingber, D. E. *Annual Review of Biomedical Engineering* **2001**, *3*, 335-373.

(7) Terry, S. C.; Jerman, J. H.; Angell, J. B. *IEEE Transactions on Electron Devices* **1979**, *26*, 1880-1886.

(8) Maluf, N. *An introduction to Microelectromechanical Systems Engineering*; Artech House, Inc.: Norwood, MA, 2000.

(9) Unger, M. A.; Chou, H. P.; Thorsen, T.; Scherer, A.; Quake, S. R. *Science* **2000**, *288*, 113-116.

(10) Becker, H.; Gartner, C. *Electrophoresis* **2000**, *21*, 12-26.

(11) Oh, K. W.; Ahn, C. H. *Journal of Micromechanics and Microengineering* **2006**, *16*, R13-R39.

(12) Nguyen, N. T.; Huang, X. Y.; Chuan, T. K. *Journal of Fluids Engineering-Transactions of the ASME* **2002**, *124*, 384-392.

(13) Woias, P. *Sensors and Actuators B—Chemical* **2005**, *105*, 28-38.

(14) Kovacs, G. T. A. *Micromachined Transducers Sourcebook* McGraw-Hill Science/Engineering/Math, 1998.

(15) Reyes, D. R.; Iossifidis, D.; Auroux, P. A.; Manz, A. *Analytical Chemistry* **2002**, *74*, 2623-2636.

(16) Lion, N.; Rohner, T. C.; Dayon, L.; Arnaud, I. L.; Damoc, E.; Youhnovski, N.; Wu, Z. Y.; Roussel, C.; Josserand, J.; Jensen, H.; Rossier, J. S.; Przybylski, M.; Girault, H. H. *Electrophoresis* **2003**, *24*, 3533-3562.

(17) Nguyen, N. T.; Wu, Z. G. *Journal of Micromechanics and Microengineering* **2005**, *15*, R1-R16.

(18) Auroux, P. A.; Iossifidis, D.; Reyes, D. R.; Manz, A. *Analytical Chemistry* **2002**, *74*, 2637-2652.

(19) SCS In *SCS Technical Document*, 2007, pp 1-12.

(20) Meng, E.; Tai, Y. C. *18th IEEE International Conference on Micro Electro Mechanical Systems (MEMS 2005)* **2005**, 568-571.

(21) Xie, J.; Shih, J.; Tai, Y. C. *16th IEEE International Conference on Micro Electro Mechanical Systems (MEMS 2003)* **2003**, 20-23.

(22) Liger, M.; Rodger, D. C.; Tai, Y. C. *16th IEEE International Conference on Micro Electro Mechanical Systems (MEMS 2003)* **2003**, 602-605.

(23) Walsh, K.; Norville, J.; Tai, Y. C. *14th IEEE International Conference on Micro Electro Mechanical Systems (MEMS 2001)* **2001**, 114-117.

(24) Shih, J.; Tai, Y.-C.; Miao, Y.; Lee, T. D. *5th IEEE Conference on Sensors (SENSORS 2006)* **2006**, 1432-1435.

(25) Shih, J.; Xie, J.; Tai, Y. C. *12th International Conference On Solid-State Sensors, Actuators And Microsystems (Transducers 2003)* **2003**, 388-391.

(26) He, Q.; Pang, C.; Tai, Y. C.; Lee, T. D. *17th IEEE International Conference on Micro Electro Mechanical Systems (MEMS 2004)* **2004**, 212-215.

(27) Miserendino, S., California Institute of Technology, Pasadena, 2007.

(28) Xie, J.; Shih, J.; Lin, Q. A.; Yang, B. Z.; Tai, Y. C. *Lab on a Chip* **2004**, *4*, 495-501.

(29) Li, P.-Y.; Shih, J.; Lo, R.; Adams, B.; Agrawal, R.; Saati, S.; Humayun, M. S.; Tai, Y.-C.; Meng, E. *20th IEEE International Conference on Micro Electro Mechanical Systems (MEMS 2007)* **2007**, 15-18.

(30) Xie, J.; Miao, Y. N.; Shih, J.; He, Q.; Liu, J.; Tai, Y. C.; Lee, T. D. *Analytical Chemistry* **2004**, *76*, 3756-3763.

(31) Xie, J.; Miao, Y. N.; Shih, J.; Tai, Y. C.; Lee, T. D. *Analytical Chemistry* **2005**, *77*, 6947-6953.

(32) Selvaganapathy, P.; Yit-shun Leung, K.; Renaud, P.; Mastrangelo, C. H. *Microelectromechanical Systems, Journal of* **2002**, *11*, 448-453.

(33) Chen, C.-L.; Selvarasah, S.; Chao, S.-H.; Khanicheh, A.; Mavroidis, C.; Dokmeci, M. R. *2nd IEEE International Conference on Nano/Micro Engineered and Molecular Systems (NEMS 2007)* **2007**, 826-829.

(34) Chen, P. J.; Rodger, D. C.; Meng, E. M.; Humayun, M. S.; Tai, Y. C. *Journal of Microelectromechanical Systems* **2007**, *16*, 223-231.

(35) Chen, P.-J.; Tai, Y.-C. *20th IEEE International Conference on Micro Electro Mechanical Systems (MEMS 2007)* **2007**, 453-456.

(36) Wang, X. Q.; Lin, Q.; Tai, Y. C. *12th IEEE International Conference on Micro Electro Mechanical Systems (MEMS 1999)* **1999**, 177-182.

(37) Wang, X. Q.; Tai, Y. C. *13th IEEE International Conference on Micro Electro Mechanical Systems (MEMS 2000)* **2000**, 68-73.

(38) Xie, J.; Yang, X.; Wang, X. Q.; Tai, Y. C. *14th IEEE International Conference on Micro Electro Mechanical Systems (MEMS 2001)* **2001**, 539-542.

(39) Selvaganapathy, P.; Carlen, E. T.; Mastrangelo, C. H. *Sensors and Actuators A—Physical* **2003**, *104*, 275-282.

(40) Ryu, K. S.; Wang, X.; Shaikh, K.; Goluch, E.; Mathias, P.; Liu, C. *9th International Conference on Miniaturized Systems for Chemistry and Life Sciences (µTAS 2005)* **2005**, 1192-1194.

(41) Licklider, L.; Wang, X. Q.; Desai, A.; Tai, Y. C.; Lee, T. D. *Analytical Chemistry* **2000**, *72*, 367-375.

(42) Shih, J.; Miao, Y. N.; Lee, T. D.; Tai, Y. C. *10th International Conference on Miniaturized Systems for Chemistry and Life Sciences (µTAS2006)* **2006**, 1573-1575.

(43) Liu, M. C.; Ho, D.; Tai, Y.-C. *2nd IEEE International Conference on Nano/Micro Engineered and Molecular Systems (NEMS 2007)* **2007**, 993-996.

(44) Lammerink, T. S. J.; Tas, N. R.; Elwenspoek, M.; Fluitman, J. H. J. *Sensors and Actuators A—Physical* **1993**, *37-8*, 45-50.

(45) Wu, S. Y.; Lin, Q.; Yuen, Y.; Tai, Y. C. *Sensors and Actuators A—Physical* **2001**, *89*, 152-158.

(46) Collins, J.; Lee, A. P. *Lab on a Chip* **2004**, *4*, 7-10.

(47) Wu, J.; Ye, J. *Lab on a Chip* **2005**, *5*, 1344-1347.

(48) Czaplewski, D. A.; Ilic, B. R.; Zalalutdinov, M.; Olbricht, W. L.; Zehnder, A. T.; Craighead, H. G.; Michalske, T. A. *Journal of Microelectromechanical Systems* **2004**, *13*, 576-585.

(49) Oosterbroek, R. E.; Lammerink, T. S. J.; Berenschot, J. W.; Krijnen, G. J. M.; Elwenspoek, M. C.; van den Berg, A. *Sensors and Actuators A—Physical* **1999**, *77*, 167-177.

(50) Ashauer, M.; Glosch, H.; Hedrich, F.; Hey, N.; Sandmaier, H.; Lang, W. *Sensors and Actuators A—Physical* **1999**, *73*, 7-13.

(51) Meng, E.; Tai, Y. C. *12th International Conference on Solid-State Sensors, Actuators and Microsystems (Transducers 2003)* **2003**, 686-689.

(52) Harnett, C. K.; Mosier, B. P.; Caton, P. F.; Wiedenman, B.; Crocker, R. W. *7th International Conference on Micro Total Analysis Systems (µTAS 2003)* **2003**, 139-142.

(53) Wu, J. A.; Sansen, W. *Sensors and Actuators A—Physical* **2002**, *97-8*, 68-74.

(54) Veenstra, T. T.; Lammerink, T. S. J.; Elwenspoek, M. C.; van den Berg, A. *Journal of Micromechanics and Microengineering* **1999**, *9*, 199-202.

(55) Shih, C. Y.; Li, W.; Zheng, S.; Tai, Y. C. *5th IEEE Conference on Sensors (SENSORS 2006)* **2006**, 271-274.

(56) Shulin, Z.; Chuan-Hua, C.; Mikkelsen, J. C., Jr.; Santiago, J. G. *Sensors and Actuators B—Chemical* **2001**, *B79*, 107-114.

(57) Reichmuth, D. S.; Chirica, G. S.; Kirby, B. J. *Sensors and Actuators B—Chemical* **2003**, *92*, 37-43.

(58) Paul, P. H.; Arnold, D. W.; Rakestraw, D. J. *3rd International Conference on Miniaturized Systems for Chemistry and Life Sciences (uTAS 1998)* **1998**, 49-52.

(59) Cameron, C. G.; Freund, M. S. *Proceedings of the National Academy of Sciences of the United States of America* **2002**, *99*, 7827-7831.

(60) Suzuki, H.; Yoneyama, R. *Sensors and Actuators B—Chemical* **2003**, *96*, 38-45.

(61) Suzuki, H.; Yoneyama, R. *Sensors and Actuators B—Chemical* **2002**, *86*, 242-250.

(62) Bohm, S.; Timmer, B.; Olthuis, W.; Bergveld, P. *Journal of Micromechanics and Microengineering* **2000**, *10*, 498-504.

(63) Munyan, J. W.; Fuentes, H. V.; Draper, M.; Kelly, R. T.; Woolley, A. T. *Lab on a Chip* **2003**, *3*, 217-220.

(64) Jones, J. E.; Hansen, L. D.; Jones, S. E.; Shelton, D. S.; Thorne, J. M. *Journal of Physical Chemistry* **1995**, *99*, 6973-6979.

(65) Will, F. G. *Journal of Electroanalytical Chemistry* **1997**, *426*, 177-184.

(66) Aebersold, R.; Mann, M. *Nature* **2003**, *422*, 198-207.

(67) Hunt, D. F.; Yates, J. R.; Shabanowitz, J.; Winston, S.; Hauer, C. R. *Proceedings of the National Academy of Sciences of the United States of America* **1986**, *83*, 6233-6237.

(68) Eng, J. K.; McCormack, A. L.; Yates, J. R. *Journal of the American Society for Mass Spectrometry* **1994**, *5*, 976-989.

(69) Bruin, G. J. M. *Electrophoresis* **2000**, *21*, 3931-3951.

(70) Harrison, D. J.; Fluri, K.; Seiler, K.; Fan, Z. H.; Effenhauser, C. S.; Manz, A. *Science* **1993**, *261*, 895-897.

(71) Jacobson, S. C.; Hergenroder, R.; Koutny, L. B.; Ramsey, J. M. *Analytical Chemistry* **1994**, *66*, 1114-1118.

(72) Ocvirk, G.; Verpoorte, E.; Manz, A.; Grasserbauer, M.; Widmer, H. M. *Analytical Methods and Instrumentation* **1995**, *2*, 74-82.

(73) Lindner, D. *Lab on a Chip* **2001**, *1*, 15N-19N.

(74) de Mello, A. *Lab on a Chip* **2002**, *2*, 48N-54N.

(75) Reichmuth, D. S.; Shepodd, T. J.; Kirby, B. J. *Analytical Chemistry* **2005**, *77*, 2997-3000.

(76) Yin, N. F.; Killeen, K.; Brennen, R.; Sobek, D.; Werlich, M.; van de Goor, T. V. *Analytical Chemistry* **2005**, *77*, 527-533.

(77) Licklider, L. J.; Thoreen, C. C.; Peng, J. M.; Gygi, S. P. *Analytical Chemistry* **2002**, *74*, 3076-3083.

(78) Badman, E. R.; Cooks, R. G. *Journal of Mass Spectrometry* **2000**, *35*, 659-671.

(79) Annesley, T. M. *Clinical Chemistry* **2003**, *49*, 1041-1044.